Electronic Pre-Compensation of Intra-Channel Nonlinearity in a 10Gb/s Optical Transmission System

by

Ahmed M. Awadalla

A thesis
presented to the University of Waterloo
in fulfillment of the
thesis requirement for the degree of
Master of Science
in
Physics

Waterloo, Ontario, Canada, 2007

I hereby declare that I am the sole author of this thesis. This is a true copy of the thesis, including any required final revisions, as accepted by my examiners.

I understand that my thesis may be made electronically available to the public.

Abstract

We introduce several new algorithms for compensating intra channel nonlinearities in lightwave systems through electronic predistortion. These were optimized and modeled assuming realistic conditions at Nortel and were found to be insensitive to normal environmental and design fluctuations in commercial systems. We also present an upper bound on system performance that agrees well with measured results.

Acknowledgements

I would like to thank my supervisors Dr. Maurice O'Sullivan and Dr. David Yevick for their continuous support and encouragement. I also would like to thank Kuang-Tsan (KT) Wu and Michael Reimer for help and advice.

Contents

1 INTRODUCTION **1**

1.1 Optical Fiber Networks 1

1.1.1 Historical Perspective 1

1.1.2 Coherent Systems and IMDD systems 2

1.1.3 Long and Short Haul 3

1.1.4 WDM 3

1.1.5 Optical Network Architecture 3

1.2 Optical Networks Elements 4

1.2.1 Optical Fibers 5

1.2.2 Optical Transmitters 5

1.2.3 Optical Receivers 5

1.2.4 Optical Amplifiers 6

1.3 Optical Fiber Impairments 7

1.3.1 Power Loss and Bandwidth 7

1.3.2 Chromatic Dispersion 8

1.3.3 Nonlinearities 9

1.4 Thesis Outline 9

2 SELF-PHASE MODULATION **11**

2.1 Qualitative Description 11

2.2 Wave Equation 12

2.2.1 Electric Polarization 13

2.2.2 Slowly Varying Envelope Approximation 14

2.3 Numerical Solution 20
2.3.1 Split-Step Fourier Transform Procedure 20

3 ELECTRONIC PRE-DISTORTION 23
3.1 Introduction 23
3.2 Mathematical Formulation 24
3.2.1 Band-Pass Signals and Systems 24
3.2.2 Band-Pass System Response 26
3.2.3 Linear Impulse Response 27
3.3 Linear Dispersion Precompensation 27
3.3.1 Base-Band Filtering 28
3.3.2 Carrier Modulation 31

4 NEXT GENERATION MODEMS 33
4.1 Introduction 33
4.2 NGM Layout 33
4.3 NGM Operation 35
4.4 Nonlinear Table 35
4.5 Finite Impulse Response Filter 38

5 SELF-PHASE MODULATION COMPENSATION IN NGM 43
5.1 Introduction 43
5.2 Previous Work 43
5.3 Nonlinear EPD in NGM 44
5.3.1 Nonlinear EPD Basic Concept 44
5.3.2 Nonlinear Optical Channel Response-Back Propagation 45
5.3.3 Required Link Parameters 46
5.3.4 NGM Capabilities 46
5.3.5 NGM Limitations 47
5.4 SPM Precompensation Algorithm in NGM 47
5.4.1 EPD Filter Details 47
5.4.2 Nonlinear RAM Evaluation 49

5.4.3 Algorithm Modification 51
5.5 Application Space 57
5.6 Reduction of Parameters of OPC 57

6 SPM COMPENSATION SENSITIVITY ANALYSIS 69
6.1 Introduction 69
6.2 Link Model 70
6.2.1 Power Variation Model 70
6.2.2 Span Length 75
6.3 Sensitivity Analysis 76
6.3.1 Methodology 76
6.3.2 Sensitivity Analysis Results 79
6.3.3 Modified Compensation Algorithm 80
6.3.4 Modified Compensation Sensitivity Analysis 83
6.3.5 Optimized Modified Compensation 86
6.4 4 Span Systems 90
6.5 Conclusions 95

A Pseudo Random Bit Sequence 96

B Dual Drive Mach-Zehnder 97

C Back Propagation/Optical Phase Conjugation 99

D Parameter Reduction 101
D.1 Single Parameter Approximation 101
D.2 Error Quantification 102

List of Tables

6.1 The G.625 fiber parameters. 78
6.2 The values of the constants in the current application space. 78
6.3 8 Spans Compensation Statistics. 80
6.4 Nonuniformity Statistical Comparison. 83
6.5 Modified Algorithm and Standard Algorithm Comparison. 86
6.6 Complete Statistical Properties List. 8 Spans 90
6.7 Complete Statistical Properties List. 4 Spans 95

List of Figures

3.1 Frequency Content of the Signal $s(t)$ 24
3.2 2D Modulation Complex Filtering. 29
3.3 FIR filter with $2N + 1$ taps, $T/2$ spaced. 30
3.4 2D modulation of a monochromatic source. 32

4.1 NGM block diagram. 34
4.2 Typical scatter diagram of a normalized complex base-band signal. 36
4.3 Allowable Modulation Area. 37
4.4 Odd FIR structure. 39
4.5 Even FIR structure. 40
4.6 NGM FIR filter. 41

5.1 Nonlinear EPD filter. 48
5.2 Standard Nonlinear EPD Algorithm. 52
5.3 Signal before/after nonlinear table. No SPM compensation. 54
5.4 Signal before/after nonlinear table. Standard SPM compensation. 55
5.5 Signal before/after nonlinear table. Standard SPM compensation Prerotated. 56
5.6 8 spans standard SPM compensation. 58
5.7 6 spans standard SPM compensation. 59
5.8 4 spans standard SPM compensation. 60
5.9 8 spans standard SPM compensation. With and without prerotation. . . . 61
5.10 8 spans SPM compensation with parameter reduction. 64
5.11 6 spans SPM compensation with parameter reduction. 65
5.12 4 spans SPM compensation with parameter reduction. 66

5.13 SPM penalty versus Alpha. 67
5.14 Optimum dispersion versus Alpha. 68

6.1 Equalized and nonequalized power evolution. 72
6.2 Pdf of SPM Compensation. 79
6.3 Alpha Sensitivity of SPM Compensation. 81
6.4 SPM compensation nonuniformity distribution. 82
6.5 Modified SPM compensation nonuniformity distribution. 84
6.6 Pdf of Modified SPM compensation. 85
6.7 Alpha sensitivity of modified compensation. 87
6.8 Pdf of optimized compensation. 88
6.9 Pdf of optimized compensation. Logarithmic Scale. 89
6.10 Alpha Sensitivity of optimized compensation. 91
6.11 4 spans compensation pdf. 92
6.12 4 spans compensation pdf. Logarithmic scale. 93
6.13 Alpha sensitivity of 4 spans compensation. 94

D.1 Analytic performance upper bound versus actual performance. 104

List of Abbreviations

ASIC	Application specific integrated circuit
BCH	Baker-Hausdorff identity
BER	Bit error rate
CW	Continuous wave
DAC	Digital to analog converter
DSP	Digital signal processing
EDFA	Erbium doped fiber amplifier
EPD	Electronic pre-distortion
FEC	Forward error correction
FFT	Fast Fourier transform
FIR	Finite impulse response
GVD	Group velocity dispersion
IM/DD	Intensity modulation direct detection
LAN	Local area network
LPF	Low pass filter
MZ	Mach-Zehnder
NDSF	Nondispersion shifted fiber
NGM	Next Generation Modem
OPC	Optical phase conjugation
PDL	Polarization dependent loss
PRBS	Pseudo random bit sequence
ROSNR	Required optical signal to noise ratio

SBS	Stimulated Brillouin scattering
SNR	Signal to noise ratio
SPB	Samples per bit
SPM	Self-phase modulation
SRS	Stimulated Raman scattering
SSF	Split Step Fourier
TDM	Time division multiplexing
WDM	Wavelength division multiplexing
XPM	Cross phase modulation

Chapter 1

INTRODUCTION

In this chapter we will briefly overview the elements and impairments of optical fiber communication links relevant to this thesis. We then briefly outline the thesis.

1.1 Optical Fiber Networks

1.1.1 Historical Perspective

While coaxial and microwave systems can operate at high bit rates the repeater spacing ($\sim$ 1 km) is small due to the large losses at high frequencies. As a result, the cost of operation is high. Lightwave systems were consequently recognized already in the 1950s as a potential replacement as the magnitude of the bit rate-distance product, BL, is several orders larger in such systems.[3]. Indeed, lightwave systems have exhibited a rapidly increasing bit rate-distance product over the last decades due to continual improvements and refinements and now constitute the primary choice for medium and long haul communication systems, including global communication at very high bit rates.

The first multimode lightwave systems operated at 0.8μm, with a repeater spacing of about 10 km. The repeater spacing increased significantly when InGaAsP semiconductor lasers enabled communication in the 1.3μm wavelength range for which the fiber loss is far smaller. In this region, the material dispersion is small but the modal dispersion of multimode fibers was high. Accordingly, single mode fiber systems became necessary.

Further, the attenuation of the fiber was further reduced by operation at the minimum absorption point near 1.55μm in place of 1.3μ. While the dispersion of normal fibers is larger at this longer wavelength, dispersion shifted fibers were developed, which enabled a repeater spacing of 70 km. Coherent lightwave systems permit even longer spacing. Further, complicated and expensive electronic repeaters were replaced by optical fiber amplifiers, which combined with dispersion compensation techniques enable all optical networks and electronic signal regeneration was completely removed. This revolutionary change was accompanied by multichannel operation based on wavelength division multiplexing (WDM) technology. [3].

In summary, the main milestones of lightwave systems were:

1. Communication grade optical fibers and coherent optical sources (0.8μm lasers).
2. InGaAsP laser sources operating at 1.3μm and implementation of single mode fibers.
3. 1.55μm operation and dispersion shifted fibers.
4. Optical fiber amplifiers and WDM systems.

1.1.2 Coherent Systems and IMDD systems

Most lightwave systems currently employ IM/DD (intensity modulation direct detection), which means that the amplitude of the laser source is modulated directly by the bit stream. Such direct amplitude modulation is referred to as intensity modulation and the corresponding receiver is a square law detector that outputs a signal that is proportional to the light signal intensity, thus eliminating phase information. This is also termed direct detection and yields a simple modulation and detection procedure that leads to low system cost and complexity.

Alternatively, coherent systems have been developed that employ a wide range of modulation-demodulation methods as in radio communication systems. Here the detection process mixes a carrier with the detected signal in order to preserve both amplitude and phase information. Coherent systems possess greater receiver sensitivity, that is less received power is required for low-error transmission but can be more affected by noise and

of course are far more complex and expensive.[3]. We will accordingly not consider such systems in this thesis.

1.1.3 Long and Short Haul

Optical fiber communication links are best suited for long haul transmission because of the long repeater spacing and low repeater (amplifier) station cost. The large fiber bandwidth, however, is increasingly attractive for short haul (< 10 km) communication systems that are becoming markedly closer to commercial acceptance.

1.1.4 WDM

While the theoretical bandwidth of optical fibers is close to ~ 10 THz, communication system electronics and photonics cannot be designed to utilize this bandwidth operating with a single source, which is effectively restricted at present to a bit rate of 40 Gb/s requiring a ~ 40 GHz bandwidth. However, the large bandwidth can be utilized by transmitting many data channels simultaneously using multiplexing techniques. Such multiplexing is generally performed both in the time domain (TDM) to combine low-frequency signals onto one 10 or 40Gb/s channel and in the frequency domain through frequency division multiplexing which combines light from many individual lasers operating at these wavelengths. Such frequency division multiplexing is termed wavelength division multiplexing, WDM, in optical communications.

1.1.5 Optical Network Architecture

In this section we describe optical network architectures, which fall into three principle categories:

1. Point to point links.
2. Broadcast links.
3. Local area networks.

Point to point links implement a simple architecture with the communication link connecting two stations in either long or short haul applications. A short haul system might connect two workstations in a building but transmit a very high-speed signal. In a long haul system, the signal must be amplified every ~ 100 km, which can be done even over many WDM channels because of the large fiber amplifier bandwidth. The network is then simply a transmitter followed by consecutive fiber spans joined by optical amplifiers.

A broadcast network broadcasts information from a single source to multiple recipients in the manner of cable TV. Such networks are employed, for example, in intra city communications. While fibers are not particularly cost-effective for such applications, the large optical bandwidth can be employed to transmit a very large number of channels such as high definition TV channels compared to coaxial cables. Such networks implement either a hub topology resembling short haul point to point systems or a bus topology. In the bus topology a single fiber link is employed that is accessed through taps that transmit only a portion of the optical power to the subscriber. The number of subscribers is then limited by the power available in the fiber, but amplifiers can increase the power periodically to augment the number of potential subscribers.

Local Area Networks, LANs connect large numbers of users in small (< 10 km) areas such as a company or an university in such a manner that each user has random access to the network. That is, in contrast with the broadcast systems, in which the data flows from one source to a number of recipients, each user can randomly access the network to transmit or receiver data. The main topologies are the bus, ring, and star topology.

This thesis is restricted to long haul WDM point-to-point optical fiber communication networks with IM/DD modulation.

1.2 Optical Networks Elements

We now introduce each element or component of the optical network of importance in this thesis.

1.2.1 Optical Fibers

Optical fibers achieve an extremely high bandwidth with low attenuation through total internal reflection. This means that for a certain range of large incidence angles the light propagating in a medium with higher refractive index does not propagate an appreciable distance into the lower refractive index media [11]. Thus dielectric waveguides can be fabricated from doped silica. These can be either multimode, which means that several modes with different spatial and angular patterns and therefore propagation velocities can be guided by the fiber. The differing velocities of these modes, however, leads to multimode dispersion and therefore relatively low data rates. A single mode fiber that only propagates one mode (neglecting polarization effects) can however be fabricated that largely eliminates this limitation.

The three main fiber impairments are loss, chromatic dispersion, and nonlinearity. These are described in detail in the next section.

1.2.2 Optical Transmitters

An optical transmitter converts the raw data it receives into a modulated optical signal and launches it into the fiber. Every transmitter contains both an electronic and an optical component. In the electronic subsystem, the raw data is processed and encoded. The processed data is converted to an analog form and applied to the laser or modulator. A modulator can be employed to modulate the optical signal it receives form the optical source in both amplitude and in some cases phase. The optical sources in most high-performance systems is a semiconductor laser while modulators are typically Mach-Zehnder interferometers.

1.2.3 Optical Receivers

An optical receiver converts an optical signal into to the electrical domain and often further processes it to generate output data. A photodetector converts the signal into electrical current that is generally proportional to the signal intensity. Such photodetectors are typically *pn* junctions that generate electrons from absorbed photons. Sophisticated junction geometries generate less noise and possess a higher quantum efficiency, defined as the

number of electrons emitted for each photon. The receiver can process the received signal through appropriate filters that remove noise and minimize intersymbol interference. A decision circuit samples the filtered electrical signal and compares the output with a given threshold to determine if the symbol was a 1 or a 0.

An important measure of the receiver quality is its sensitivity, which is the minimum SNR (signal power to noise power ratio) at the input of the receiver required for satisfactory operation. A measure of the performance of a system is its bit error rate, BER, which is generally defined as the average probability of incorrect bit identification [3]. For each system, a maximum BER is defined above which the system is said to be failed or outed. The receiver sensitivity is the minimum SNR required to ensure a BER below the threshold value. A typical value of BER threshold in optical systems is 10^{-9}, or 10^{-3} if error correction codes are used.

1.2.4 Optical Amplifiers

When the power of the optical signal propagating in the fiber decreases below a certain limit due to loss, it must be increased to a higher level and possibly filtered through repeaters formed from optical amplifiers and regenerators. Regenerators transfer the signal back to the electrical domain, reconstruct the original signal waveform and retransmit it through a separate transmitter module. Such components are generally high cost and system specific since an upgrade with higher bit rate generally requires a new regenerator. Further, each wavelength channel normally demands a separate regenerator. Large bandwidth optical fiber amplifiers, on the other hand, are not system specific, can be employed in multichannel systems, and are simple and relatively inexpensive. However, contrary to regenerators, they introduce additional noise that accumulates with an increased number of amplifiers. Further, the gain of the amplifiers is not wavelength-independent, impacting the link design process.

We consider only erbium doped fiber amplifiers, EDFA, below. The EDFA is currently the most widely employed optical amplifier since it is an all-fiber device and therefore simple to implement, does not introduce crosstalk in WDM systems and because the main EDFA component, namely the pump laser, is compact, reliable and can emit high power.[19] In the following we therefore briefly summarize EDFA properties.

EDFA

An EDFA is a length of typical fiber doped with erbium ions. The signal to be amplified is input into the EDFA together with the optical pump light through a wavelength selective coupler. A second wavelength selective coupler at the output separates the signal from the pump. Thus the main components are an erbium doped fiber, two couplers, two isolators, and the pump laser. The pump creates a population inversion in the fiber that enables amplification through stimulated emission. Erbium ions possess three relevant energy levels; $E1$, $E2$, and $E3$, in ascending order such that the pump laser at wavelength 980 nm is absorbed by the $E1$ to $E3$ transition followed by decay to $E2$ through spontaneous emission. However since the life time of the ions in $E3$ is $\sim 1\mu$s and in $E2$ is ~ 10 ms, population inversion occurs between $E2$ and $E1$. Since $hc/(E2-E1)$ falls in the wavelength region of interest to high-speed communication systems, a communication signal in an EDFA will be amplified. Further, Stark splitting splits each energy level into several closely-spaced levels that are nearly equally occupied due to thermalization. As a consequence, such an amplifier amplifies a wavelength band, although the gain is unequal over the different wavelengths since the electrons are not evenly distributed in energy.[22].

1.3 Optical Fiber Impairments

1.3.1 Power Loss and Bandwidth

Fiber loss is generally expressed according to the formula

$$P_{out} = \exp\{-\alpha L\} P_{in} \tag{1.1}$$

in which α is termed the fiber attenuation parameter and L is the fiber length.[19] The physical origin of fiber loss are material absorption and Rayleigh scattering, which is caused by light scattering from microscopic inhomogeneities in the glass. Material absorption is insignificant over the range of $800-1600$ nm but increases rapidly at higher wavelengths while Rayleigh scattering is inversely proportional to fourth power of the wavelength. The joint attenuation of the two mechanisms thus has a minima of .2 dB/km at 1550 nm.

However, other wavelength windows are generally employed, for which the attenuation is 2.5 dB/km at 800 nm, .5 dB/km at 1300 nm, and is dominated by Rayleigh scattering.

The window of operation at 1550 nm is further divided into three bands motivated by the possible choices of amplifiers within this bandwidth. The lowest band is called the S-band, in the range $1460 - 1530$ nm, and is amplified by Raman amplifiers. The C-band, $1530 - 1565$ nm, is amplified by standard EDFAs while the L-band, $1565 - 1625$ nm, is employed for high capacity WDM systems as it requires gain shifted EDFAs.[19]. Note that each band possesses a bandwidth in the order of ~ 1 THz.

1.3.2 Chromatic Dispersion

Chromatic dispersion arises since different spectral components in a fiber propagate at different group velocities. In single mode fibers chromatic dispersion has two sources, namely material and waveguide dispersion. Material dispersion refers to the frequency dependence of the refractive index of bulk glass while the waveguide dispersion is caused by group velocity dependence on wavelength in modes of a waveguiding medium of a frequency-independent refractive index medium. The group velocity dispersion, GVD, is

$$\beta_2 = \frac{d^2\beta}{d\omega^2} = \beta_2^{material} + \beta_2^{waveguide} \tag{1.2}$$

Systems in which $\beta_2 < 0$ are called anomalous while those with $\beta_2 > 0$ are termed normal.

In silica, a transition from normal to anomalous occurs in the 1300 nm window, which implies that dispersion in this window is low. For the same reason, the 1550 nm window normally exhibits large dispersion. However, properly designed refractive index profiles can yield a waveguide dispersion that cancels the material dispersion in this window of operation. Such fibers are termed dispersion shifted. Alternatively, dispersion compensation modules can be employed, which are fibers that have the opposite value of the total dispersion of each fiber span. Thus propagation through the fiber span followed by the compensation module removes the pulse spreading effect.

1.3.3 Nonlinearities

As the bit rate and the launch power of communication systems increases, nonlinear effects become significant. One class of nonlinearities arises due to scattering inside the fiber. These are principally stimulated Brillouin scattering, SBS, and stimulated Raman scattering, SRS. Here energy is transferred from one wave, called pump wave, to a second Stokes wave, due to scattering. A second category of nonlinear effects is created by the nonlinear dependence of the fiber refractive index on the signal power. These are principally self-phase modulation, SPM, cross phase modulation, XPM, and four wave mixing. The latter two effects exists in multichannel systems only as they arise from nonlinear generation of harmonics of the channel frequencies that introduce signal distortion. In XPM, the distortion yields nonlinear cross talk between two channels, while four wave mixing generates a cross talk in a third channel from the interaction between two channels. The effect of XPM and four wave mixing is significantly reduced by increasing the wavelength separation between channels or by proper wavelength positioning of the channels. SPM is an intra channel effect that causes intensity proportional phase modulation, this phase modulation interacts with dispersion inducing amplitude modulation that is a source of penalty in present communication systems. This thesis considers exclusively SPM, which will therefore be examined in detail in the subsequent. Other nonlinear effects are not of relevance to the thesis since the system of interest here is designed to minimize these nonlinearities. However, it should be noted that dispersion and SPM can interact in long haul systems with inline amplifiers and the resulting effects can accumulate with overall length to generate the principal source of pulse distortion.

1.4 Thesis Outline

In the second chapter, 2, self-phase modulation (SPM) is described and the propagation equation for the electric field in the presence of SPM is derived. We then discuss the simplifications required to implement our numerical solutions to the propagation equation and present our computational procedure.

The third chapter, 3, presents a discussion of electronic precompensation which we employ to compensate for distortion caused by self-phase modulation. We describe the

mathematical basis and the hardware required by the precompensator and finally examine its application to chromatic dispersion.

In chapter 4 the Nortel next generation modem (NGM) transmission system that is employed for precompensation is examined. We present the system block diagram and discuss the relevant blocks.

The next chapter, 5, examines an algorithm for implementing SPM compensation. Simplifications of this algorithm are discussed and the different methods are compared.

Chapter 6 presents a statistical sensitivity analysis based on a model of physical fluctuations in the optical link. Designs that minimize the effect of these variations are further introduced.

Chapter 2

SELF-PHASE MODULATION

Self-phase modulation (SPM) is a nonlinear optical effect arising from the interaction of light with matter. The Kerr effect changes the refractive index of bulk media with optical intensity. Accordingly, for a train of pulses of light traveling in a certain medium, the refractive index of the medium changes with the pulse amplitude, causing both pure amplitude modulation and a phase modulation that can as well be partially converted to amplitude modulation in the presence of chromatic dispersion.

In this chapter self-phase modulation will be overviewed and the nonlinear propagation equation derived. This equation cannot in general be analytically solved, so numerical techniques will be discussed instead, including those employed in this thesis.

2.1 Qualitative Description

Self-phase modulation introduce an intensity dependent added phase to the transmitted pulses. Given the fact that the presence of chirp sometimes amplifies the distortion introduced by chromatic dispersion[19], we find that the SPM induced, intensity dependent chirp will also react with the chromatic dispersion and introduce further distortion to the transmitted pulses.

To understand the physical effect of the Kerr nonlinearity, consider the case that anomalous chromatic dispersion is present; that is, the second differential of the propagation constant with respect to frequency is negative. Then for a pulse traveling in the medium,

the red shifted components of the pulse will, in general, travel slower than the blue shifted components. However, since the SPM-induced phase is linearly proportional to pulse intensity, and the time derivative of the leading part of the pulse is negative, the SPM-induced phase red-shifts the leading part of the pulse and blue-shifts the trailing part. Thus self-phase modulation here causes the leading and trailing parts of the pulse to approach each other.

The magnitude of SPM-induced chirp principally depends on the power level of the signal and its second derivative with respect to time. Thus SPM distortion is important for either high power or rapid pulse rates.

2.2 Wave Equation

Light propagation is governed by Maxwell's equations from which we will here derive the equation for light inside a fibre including nonlinear effects. Maxwell's equations are[11]

$$\nabla \cdot \mathbf{D} = \rho \tag{2.1}$$

$$\nabla \cdot \mathbf{B} = 0 \tag{2.2}$$

$$\nabla \times \mathbf{H} = \frac{\partial \mathbf{D}}{\partial t} + \mathbf{j} \tag{2.3}$$

$$\nabla \times \mathbf{E} = -\frac{\partial \mathbf{B}}{\partial t} \tag{2.4}$$

where $\mathbf{E}$ and $\mathbf{H}$ are the electric and magnetic fields, respectively, and $\mathbf{D}$ and $\mathbf{B}$ are the electric and magnetic flux densities, respectively, $\mathbf{j}$ is the current density vector and finally ρ is the charge density. In the case of propagation in dielectrics such as optical fibres, $\mathbf{j} = \mathbf{0}$ and $\rho = 0$.

We can combine the equations together using the constitutive relations [9]

$$\mathbf{D} = \epsilon_o \mathbf{E} + \mathbf{P} \tag{2.5}$$

$$\mathbf{B} = \mu_o \mathbf{H} + \mathbf{M} \tag{2.6}$$

Here ϵ_o is the free space permittivity, μ_o is the free space permeability, $\mathbf{P}$ is the induced electric polarization, and $\mathbf{M}$ is the induced magnetic polarization. Since silica is a nonmagnetic material, $\mathbf{M} = 0$.

Employing the constitutive equations in Maxwell's equation yields [1]

$$\nabla \times \nabla \times \mathbf{E} = -\frac{1}{c^2}\frac{\partial^2 \mathbf{E}}{\partial t^2} - \mu_o \frac{\partial^2 \mathbf{P}}{\partial t^2} \tag{2.7}$$

after noting that $\mu_o \epsilon_o = 1/c^2$ with c the speed of light in free space. The induced electric polarization, $\mathbf{P}$, is in general a complex function of $\mathbf{E}$ that we accordingly approximate below.

2.2.1 Electric Polarization

Optical fibers operate in the wavelength range .5–2 μm that is far from the resonant absorption peaks of electronic transitions, so that a simple phenomenological relation between $\mathbf{P}$ and $\mathbf{E}$ can be employed (see Eq. 2.9). In the absence of magnetic dipoles and assuming negligible higher order multipole effects, the system response to electric field is dominated by the electric dipole, and is therefore local[21, 1]; that is, $\mathbf{P}(\mathbf{r})$ at $\mathbf{r} = \mathbf{r}_1$ depends only on $\mathbf{E}(\mathbf{r}_1)$. In the linear case we then obtain[21]

$$\mathbf{P}(\mathbf{r}, t) = \epsilon_o \int_{-\infty}^{\infty} \chi^{(1)}(t - t') \cdot \mathbf{E}(\mathbf{r}, t') dt' \tag{2.8}$$

in which $\chi^{(1)}$ is the linear susceptibility. At sufficiently low powers, this equation reproduces linear wave propagation, further, for larger powers, $\mathbf{P}$ can be expanded into a power series in $\mathbf{E}$ [21]

$$\begin{aligned} \mathbf{P}(\mathbf{r}, t) = \quad & \epsilon_o \int_{-\infty}^{\infty} \chi^{(1)}(t - t') \cdot \mathbf{E}(\mathbf{r}, t') dt' \\ + \quad & \epsilon_o \int_{-\infty}^{\infty} \chi^{(2)}(t - t_1, t - t_2) : \mathbf{E}(\mathbf{r}, t_1)\mathbf{E}(\mathbf{r}, t_2) dt_1 dt_2 \\ + \quad & \epsilon_o \int_{-\infty}^{\infty} \chi^{(3)}(t - t_1, t - t_2, t - t_3) \vdots \mathbf{E}(\mathbf{r}, t_1)\mathbf{E}(\mathbf{r}, t_2)\mathbf{E}(\mathbf{r}, t_3) dt_1 dt_2 dt_3 \\ + \quad & \ldots \end{aligned} \tag{2.9}$$

such that the first term represents the linear contribution and the other terms are the nonlinear terms, i.e.

$$\mathbf{P} = \mathbf{P}_L + \mathbf{P}_{NL} \tag{2.10}$$

where terms constituting $\mathbf{P}_{NL}$ are, in the frequency domain[21],

$$\mathbf{P}^{(n)}(\omega) = \epsilon_o \chi^{(n)}(\omega_1, \omega_2, ..., \omega_n) \vdots \mathbf{E}(\omega_1)\mathbf{E}(\omega_2).....\mathbf{E}(\omega_n) \tag{2.11}$$

and n represents the nonlinear order. For materials with inversion symmetry such as silica glass, all even order nonlinearities vanish [4]. For the remaining discussion, only the lowest (third) order non-zero term will be retained

$$\mathbf{P}_{NL} \approx \epsilon_o \int_{-\infty}^{\infty} \chi^{(3)}(t - t_1, t - t_2, t - t_3) \vdots \mathbf{E}(\mathbf{r}, t_1)\mathbf{E}(\mathbf{r}, t_2)\mathbf{E}(\mathbf{r}, t_3) dt_1 dt_2 dt_3 \tag{2.12}$$

Another valid approximation here is to consider the temporal variation of $\chi^{(3)}$ to be of zero width, i.e delta-dirac distributed, the atom response to input pulse occurs on a scale of less than $100fs$, much larger than optical fluctuations and hence it does not respond to those variations. Average power variations in the signal occurring at modern communication bit rates are, however, much larger than $100fs$. Thus the response of the material to the incoming field can be regarded as instantaneous [1, 19, 8] with nonlinear and linear electronic polarizations

$$\mathbf{P}_{NL}(\mathbf{r}, t) \approx \epsilon_o \chi^{(3)} \vdots \mathbf{E}(\mathbf{r}, t)\mathbf{E}(\mathbf{r}, t)\mathbf{E}(\mathbf{r}, t) \tag{2.13}$$

and

$$\mathbf{P}_L(\mathbf{r}, t) \approx \epsilon_o \chi^{(1)} \mathbf{E}(\mathbf{r}, t) \tag{2.14}$$

respectively.

2.2.2 Slowly Varying Envelope Approximation

We now solve Eq. 2.7 for field propagation in a piecewise homogenous single-mode fiber. We assume that the field is quasi-monochromatic field with

$$\frac{\Delta\omega}{\omega_o} \ll 1 \tag{2.15}$$

where ω_o is the center frequency of the propagating field and $\Delta\omega$ is the bandwidth, and weakly guiding, $\Delta n/n << 1$. The vector wave equation can be replaced by the scalar wave equation, 2.7, which can then be solved perturbatively by considering $\mathbf{P}_{NL}$ as a small perturbation to $\mathbf{P}_L$. We then employ the slowly-varying-envelope approximation. Given the piecewise homogeneity of the fiber and 2.10, Eq. 2.7 becomes

$$\nabla^2\mathbf{E} - \frac{1}{c^2}\frac{\partial^2\mathbf{E}}{\partial t^2} = \mu_o\frac{\partial^2\mathbf{P}_L}{\partial t^2} + \mu_o\frac{\partial^2\mathbf{P}_{NL}}{\partial t^2} \tag{2.16}$$

From the weakly guiding nature of the fiber and the quasi-monochromatic property of the optical field, we can write the electric field and the linear and nonlinear polarization as

$$\mathbf{E}(\mathbf{r},t) = \frac{1}{2}\hat{x}[\bar{E}(\mathbf{r},t)exp(-i\omega_o t) + c.c] \tag{2.17}$$

$$\mathbf{P}_L(\mathbf{r},t) = \frac{1}{2}\hat{x}[\bar{P}_L(\mathbf{r},t)exp(-i\omega_o t) + c.c] \tag{2.18}$$

$$\mathbf{P}_{NL}(\mathbf{r},t) = \frac{1}{2}\hat{x}[\bar{P}_{NL}(\mathbf{r},t)exp(-i\omega_o t) + c.c] \tag{2.19}$$

in which *c.c.* stands for complex conjugate, $\hat{x}$ is the polarization unit vector. $\bar{E}(\mathbf{r},t)$, $\bar{P}_L(\mathbf{r},t)$ and $\bar{P}_{NL}(\mathbf{r},t)$ are the slowly varying parts of the electric field, linear and nonlinear electronic polarization respectively[1].

Substituting Eq. 2.17 in Eq. 2.13 we find

$$\begin{aligned}\mathbf{P}_{NL}(\mathbf{r},t) &= \frac{1}{2}\hat{x}[\frac{\epsilon_o}{4}\chi^{(3)}\bar{E}^3(\mathbf{r},t)exp(-3i\omega_o t) + c.c] \\ &+ \frac{1}{2}\hat{x}[\epsilon_o\frac{3}{4}\chi^{(3)}|\bar{E}(\mathbf{r},t)|^2\bar{E}(\mathbf{r},t)exp(-i\omega_o t) + c.c]\end{aligned} \tag{2.20}$$

Since the $3\omega_0$ term is not phase matched to the propagating field, we obtain after comparing with Eq. 2.19

$$\bar{P}_{NL}(\mathbf{r},t) = \epsilon_o\epsilon_{NL}\bar{E}(\mathbf{r},t) \tag{2.21}$$

with

$$\epsilon_{NL} = \frac{3}{4}\chi^{(3)}|\bar{E}(\mathbf{r},t)|^2 \tag{2.22}$$

Rearranging 2.16 then yields

$$\nabla^2\mathbf{E} = \frac{1}{c^2}\frac{\partial^2}{\partial t^2}(\mathbf{E} + \frac{1}{\epsilon_o}\mathbf{P}_L + \frac{1}{\epsilon_o}\mathbf{P}_{NL}) \tag{2.23}$$

After substituting 2.17 2.18 2.19 2.21, 2.14 we arrive at

$$\nabla^2\bar{E}(\mathbf{r},t)exp(-i\omega_o t) = \frac{1}{c^2}\frac{\partial^2}{\partial t^2}(\epsilon_t\bar{E}(\mathbf{r},t)exp(-i\omega_o t)) \tag{2.24}$$

where

$$\epsilon_t = (1 + \chi^{(1)} + \epsilon_{NL}) \tag{2.25}$$

This yields the nonlinear scalar wave equation if only the first order nonlinearity is retained and the instantaneous response approximation is applied.

While 2.24 would normally be Fourier transformed, since ϵ_{NL} contains temporal variation this step does not lead to the standard simplifications. Therefore, as noted above, the contribution of ϵ_{NL} is examined perturbatively[2, 1]. To first order, we have

$$\begin{aligned}\nabla^2\tilde{E}(\mathbf{r},\omega-\omega_o) &= \frac{\epsilon_t(\omega)}{c^2}(i\omega)^2\tilde{E}(\mathbf{r},\omega-\omega_o) \\ &= -\frac{\epsilon_t(\omega)}{c^2}\omega^2\tilde{E}(\mathbf{r},\omega-\omega_o)\end{aligned} \tag{2.26}$$

after replacing the Fourier transform of time derivatives by $i\omega$ and noting that the transform of a function multiplied by a temporal exponential leads to a frequency shift in the function.

2.26 can now be solved through separation of variables. That is, we assume that $\tilde{E}(\mathbf{r},\omega-\omega_o)$ possesses the following form [1, 2]

$$\tilde{E}(\mathbf{r},\omega-\omega_o) = F(x,y)\tilde{A}(z,\omega-\omega_o)\exp i\beta_o z \tag{2.27}$$

in which the rapid variations in the propagation direction, z, are segregated into the exponential term, according to the slowly varying amplitude approximation, while the

rapid temporal variations are associated with the $\exp i\omega_o t$ term, consistent with the quasi-monochromatic approximation. In other words, higher order derivatives with respect to t or z are neglected, as already evident when ϵ_{NL} was considered constant when Fourier transforming.

Substituting 2.27 into 2.26, and employing

$$k_o^2 = \left(\frac{\omega_o}{c}\right)^2 \tag{2.28}$$

$$\begin{aligned}\frac{\partial^2}{\partial z^2}(\tilde{A}(z,\omega-\omega_o)\exp i\beta_o z) &= \frac{\partial}{\partial z}\{\frac{\partial \tilde{A}(z,\omega-\omega_o)}{\partial z}\exp i\beta_o z + i\beta_o \tilde{A}(z,\omega-\omega_o)\exp i\beta_o z\} \\ &= \exp i\beta_o z\{\frac{\partial^2 \tilde{A}(z,\omega-\omega_o)}{\partial z^2} + 2i\beta_o \frac{\partial \tilde{A}(z,\omega-\omega_o)}{\partial z} \\ &\quad -\beta_o^2 \tilde{A}(z,\omega-\omega_o)\}\end{aligned} \tag{2.29}$$

yields

$$\nabla^2(F(x,y)\tilde{A}(z,\omega-\omega_o)\exp i\beta_o z) = -\frac{\epsilon_t(\omega)}{c^2}\omega^2 F(x,y)\tilde{A}(z,\omega-\omega_o)\exp i\beta_o z \tag{2.30}$$

$$\begin{aligned}\tilde{A}(z,\omega-\omega_o)\exp i\beta_o z\nabla_{tr}^2 F(x,y) &+ F(x,y)\frac{\partial^2}{\partial z^2}(\tilde{A}(z,\omega-\omega_o)\exp i\beta_o z) \\ &= -\epsilon_t(\omega)(\frac{\omega}{c})^2 F(x,y)\tilde{A}(z,\omega-\omega_o)\exp i\beta_o z\end{aligned} \tag{2.31}$$

Substituting in 2.26, dividing by $F(x,y)\tilde{A}(z,\omega-\omega_o)\exp i\beta_o z$ and rearranging, yields two separate equations with a common eigenvalue, $\bar{\beta}^2(\omega)$. The wave equation accordingly adopts the form

$$\nabla_{tr}^2 F(x,y) + (\epsilon_t(\omega)k_o^2 - \bar{\beta}^2(\omega))F(x,y) = 0 \tag{2.32}$$

$$2i\beta_o\frac{\partial \tilde{A}(z,\omega-\omega_o)}{\partial z} + (\bar{\beta}^2(\omega) - \beta_o^2)\tilde{A}(z,\omega-\omega_o) = 0 \tag{2.33}$$

We now solve the first equation for the value of this eigenvalue in a first order approximation for which ϵ_{NL} is set to zero and then this value is employed in the second equation. The solution for $F(x,y)$ then will be identical to the standard solution for single mode fibers and the 0 order eigenvalue $\bar{\beta}^{(0)}(\omega)$ will exhibit the standard dispersion relation.

Subsequently we include ϵ_{NL} again and correct the lowest-order estimate. In this order, $F(x,y)$ is unchanged while the eigenvalue is corrected according to[14]

$$\bar{\beta}^{(1)}(\omega) = \bar{\beta}^{(0)}(\omega) + \delta\beta \tag{2.34}$$

with

$$\delta\beta = \frac{k_o}{2n} \frac{\int_{x,y} \epsilon_{NL} |F(x,y)|^2 dxdy}{\left(\int_{x,y} |F(x,y)|^2 dxdy\right)^2} \tag{2.35}$$

and

$$n = \sqrt{1 + \chi^{(1)}} \tag{2.36}$$

We have assumed $\chi^{(1)}$is real, so that material losses are absent.

Substituting the above expressions into 2.33 and applying the following approximations

$$\begin{aligned} \bar{\beta}(\omega) &\approx \bar{\beta}^{(1)}(\omega) = \bar{\beta}^{(0)}(\omega) + \delta\beta & (2.37) \\ \bar{\beta}^2(\omega) - \beta_o^2 &= (\bar{\beta}(\omega) + \beta_o)(\bar{\beta}(\omega) - \beta_o) \\ &\approx 2\beta_o(\bar{\beta}(\omega) - \beta_o) & (2.38) \end{aligned}$$

the last of which is a consequence of both the weakly guiding and the quasi-monochromatic approximations, and further applying the latter approximation to neglect higher order terms in a Taylor expansion of $\bar{\beta}^{(0)}(\omega)$ (the linear propagation constant) around ω_o, so that,

$$\bar{\beta}^{(0)}(\omega) \approx \beta_o + (\omega - \omega_o)\beta_1 + \frac{1}{2}(\omega - \omega_o)^2\beta_2 \tag{2.39}$$

where $\beta_1$is the reciprocal of the group velocity and β_2 is the group velocity dispersion, we obtain

$$i\frac{\partial \tilde{A}(z, \omega - \omega_o)}{\partial z} + \{(\omega - \omega_o)\beta_1 + \frac{1}{2}(\omega - \omega_o)^2\beta_2 + \delta\beta\}\tilde{A}(z, \omega - \omega_o) = 0 \tag{2.40}$$

Inverse Fourier transforming and replacing all instances of $(\omega - \omega_o)$ by the temporal differential

$$i\frac{\partial A(z,t)}{\partial z} + i\beta_1\frac{\partial A(z,t)}{\partial t} - \frac{\beta_2}{2}\frac{\partial^2 A(z,t)}{\partial t^2} + \delta\beta A(z,t) = 0 \tag{2.41}$$

and substituting2.28, 2.22 and 2.27 into 2.35 yields

$$\delta\beta = \gamma|A(z,t)|^2 \tag{2.42}$$

with

$$\gamma = \frac{\omega_o n_2}{cA_{eff}} \tag{2.43}$$

$$n_2 = \frac{3\chi^{(3)}}{8n} \tag{2.44}$$

$$A_{eff} = \frac{\left(\int_{x,y}|F(x,y)|^2 dxdy\right)^2}{\int_{x,y}|F(x,y)|^4 dxdy} \tag{2.45}$$

Here $\delta\beta$ was considered constant when the wave equation is Fourier transformed according to our first order approximation. The radial frequency in γ has further been approximated by the center frequency.

Including the optical loss, which is proportional to the imaginary part of $\chi^{(1)}$ adds an additional term to 2.41, which now becomes

$$i\frac{\partial A(z,t)}{\partial z} + i\beta_1\frac{\partial A(z,t)}{\partial t} - \frac{\beta_2}{2}\frac{\partial^2 A(z,t)}{\partial t^2} + \gamma|A(z,t)|^2 A(z,t) + i\frac{\alpha}{2}A(z,t) = 0 \tag{2.46}$$

Finally we perform the substitution

$$T = t - \frac{z}{v_g} = t - \beta_1 z \tag{2.47}$$

$$z = z \tag{2.48}$$

to arrive at a frame of reference in which the envelope of the signal is stationary. After this transformation we arrive at the desired propagation equation

$$\frac{\partial A(z,T)}{\partial z} = -i\frac{\beta_2}{2}\frac{\partial^2 A(z,T)}{\partial T^2} - \frac{\alpha}{2}A(z,T) + i\gamma|A(z,T)|^2 A(z,T) \tag{2.49}$$

Despite the numerous approximations, Eq. 2.49 explains nonlinear effects with sufficient accuracy for the calculations of this thesis. However, it should be noted that as a result of the quasi-monochromatic approximation pulses of light of width $T \leq 100$ fs, cannot be described with our technique [1] as different equations then apply.[10]

2.3 Numerical Solution

Analytic methods cannot be employed to solve Eq. 2.49 except for certain specific input fields. While numerous numerical algorithms are available to solve the equation numerically, perhaps the most frequently employed is the split-step Fourier method (SSF) [1], which we accordingly analyze in this section.

2.3.1 Split-Step Fourier Transform Procedure

Rewriting the propagation equation of propagation as

$$\frac{\partial A(z,T)}{\partial z} = (\hat{D}(T) + \hat{N}(z,T)) \times A(z,T) \tag{2.50}$$

with

$$\hat{D}(T) = -\frac{i}{2}\beta_2\frac{\partial^2}{\partial T^2} - \frac{\alpha}{2} \tag{2.51}$$

$$\hat{N}(z,T) = i\gamma|A(z,T)|^2 \tag{2.52}$$

we find a formal solution[14],

$$A(z,T) = \exp\{\int_0^z (\hat{D}(T) + \hat{N}(\zeta,T))d\zeta\} \times A(0,T) \tag{2.53}$$

If the integral in the above equation is performed

$$\hat{D}_t(z,T) = \hat{D}(T)z \tag{2.54}$$
$$\hat{N}_t(z,T) = \int_0^z \hat{N}(\zeta,T)d\zeta \tag{2.55}$$

the solution becomes,

$$A(z,T) = \exp\{\hat{D}_t(z,T) + \hat{N}_t(z,T)\} \times A(0,T) \tag{2.56}$$

However, in this case the exponent contains the sum of two non-commuting operators and cannot therefore be separated into two simple exponentials. We accordingly apply the Baker-Hausdorff formula[5],

$$\exp(\hat{X})\exp(\hat{Y}) = \exp(\hat{X} + \hat{Y} + \frac{1}{2}[\hat{X},\hat{Y}] + \frac{1}{12}[\hat{X} - \hat{Y},[\hat{X},\hat{Y}]] + ...) \tag{2.57}$$

and retain only a limited number of terms from the expansion.

In the split-step Fourier (SSF) method higher-order commutators in the BCH identity are neglected by noting that if the length of the fiber segment is sufficiently short, these terms are small compared to the lowest-order term. Accordingly, the SSF method divides the link into small segments, such that the lowest-order expansion is valid in each. This yields

$$A(z+h,T) = \exp\{\hat{D}_t(h,T) + \hat{N}_t(h,T)\} \times A(z,T) \tag{2.58}$$
$$\approx \exp\{\hat{D}_t(h,T)\}\exp\{\hat{N}_t(h,T)\} \times A(z,T) \tag{2.59}$$
$$= \exp\{\hat{D}_t(h,T)\}\{\exp\{\hat{N}_t(h,T)\} \times A(z,T)\} \tag{2.60}$$

and the solution for the full fiber results after repeated alternate application of these two operators. Accordingly, a trade-off exists between accuracy, achieved by minimizing h, and efficiency which is degraded by the increased number of numerical operations.

To apply the first operator in the above formula, we simply evaluate the integral in Eq. 2.55. By neglecting variation in the propagation direction, the result is simply

$$\hat{N}_t(h,T) = \int_z^{z+h} \hat{N}(\zeta,T)d\zeta \tag{2.61}$$

$$\approx ih\gamma|A(z,T)|^2 \tag{2.62}$$

The dispersion part is then evaluated in the Fourier domain where each $\frac{\partial}{\partial T}$ is replaced by $i\omega$. Thus,

$$\exp\{\hat{D}_t(h,T)\}\times \equiv F^{-1}\{\exp(h\hat{D}(\omega))F\{ \tag{2.63}$$

Finally the equation relating the envelope at $z+h$ to the envelope at z is

$$A(z+h,T) = \exp(-\frac{\alpha h}{2})F^{-1}\{\exp\{\frac{i}{2}h\beta_2\omega^2\}F\{\exp(ih\gamma|A(z,T)|^2)A(z,T)\}\} \tag{2.64}$$

Importantly, while the main numerical operation in the SSF method is the Fourier transform, the numerical efficiency[17] is excellent, leading to a highly efficient numerical method.

We can if desired, further enhance the accuracy of the method by applying the following symmetric form[7],

$$A(z+h,T) = \exp\{\hat{D}_t(\frac{h}{2},T)\}\{\exp\{\hat{N}_t(h,T)\}\{\exp\{\hat{D}_t(\frac{h}{2},T)\}\times A(z,T)\}\} \tag{2.65}$$

This expression yields a zero coefficient for the first commutator in the Baker-Hausdorff expansion so that the error resulting from separating the two terms in the exponent is reduced.

Chapter 3

ELECTRONIC PRE-DISTORTION

3.1 Introduction

Chromatic fiber dispersion constitutes a primary source of distortion in high bit rate long-haul optical communication systems. While this effect is often equalized with dispersion compensating fiber with a length that yields the negative of the dispersion of the communication link, this adds expense, introduces excess losses, and reduces the flexibility in network planning because of the increased component count. Instead, we here examine electronic pre-distortion, (EPD), a process in which the channel response is inverted, and applied through fast digital signal processing circuitry, to the signal at the transmitter. Because the channel response varies in both phase and amplitude, a phase and amplitude modulator is required. Since both a fast DSP and a complex modulator are present, this form of EPD has not been previously employed. However, recent progress led to an experiment in which transmission over more than five thousand kilometers without optical compensation was achieved[12]. In this context, it should be noted that if the compensator is placed at the receiver as opposed to the transmitter, for intensity (i.e. incoherent) detection systems, phase information will be lost after detection and hence electronic compensation will be less effective.

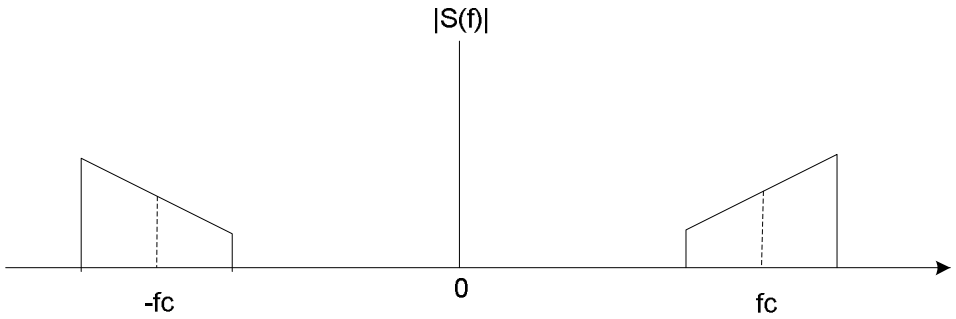

Figure 3.1: Frequency Content of the Signal $s(t)$

3.2 Mathematical Formulation

3.2.1 Band-Pass Signals and Systems

Signals formed by carrier modulation are termed band-pass signals. If the signal bandwidth is much smaller than the carrier frequency, it is further called a narrowband band-pass signal. We will study such signals in which the carrier frequency is the frequency of the unmodulated laser light. In this section we represent such signals mathematically.

Consider a real-valued narrowband band-pass signal $s(t)$ with a carrier frequency f_c. The frequency content of such a signal is shown in Fig. 3.1. A signal that contains the positive part of the frequency content is

$$S_+(f) = 2u(f)S(f) \tag{3.1}$$

where $S(f)$ and $u(f)$ are the Fourier transforms of $s(t)$ and the unit step function, respectively. The inverse Fourier transform of 3.1 yields

$$\begin{aligned} s_+(t) &= \int_{-\infty}^{\infty} S_+(f) exp(i2\pi ft) df \\ &= F^{-1}[2u(f)] \star F^{-1}[S(f)] \end{aligned} \tag{3.2}$$

where $\star$ represents convolution. Further,

$$F^{-1}[2u(f)] = \delta(t) + i\frac{1}{\pi t} \tag{3.3}$$

Substituting 3.3 in 3.2 yields

$$\begin{aligned} s_+(t) &= [\delta(t) + i\frac{1}{\pi t}] \star s(t) \\ &= s(t) + i\frac{1}{\pi t} \star s(t) \end{aligned} \tag{3.4}$$

where the second term in 3.4 is purely imaginary. The low-pass signal is obtained by translating the frequency spectrum of $s_+(t)$ by f_c, that is

$$S_l(f) = S_+(f + f_c) \tag{3.5}$$

or

$$s_l(t) = s_+(t)e^{-i2\pi f_c t} \tag{3.6}$$

The subscript l indicates low-pass. Inserting 3.4 in 3.6 and rearranging yields

$$s(t) + i\frac{1}{\pi t} \star s(t) = s_l(t)exp(i2\pi f_c t) \tag{3.7}$$

Taking the real part of both sides of the above equation yields the desired relation between the band-pass signal and its low-pass (envelope) representation

$$s(t) = \Re\{s_l(t)e^{(i2\pi f_c t)}\} \tag{3.8}$$

Note as well that

$$\begin{aligned} S(f) &= \int_{-\infty}^{\infty} s(t)\exp(-i2\pi ft)dt = \int_{-\infty}^{\infty} \Re\{s_l(t)\exp(i2\pi f_c t)\}\exp(-i2\pi ft)dt \\ &= \frac{1}{2}\int_{-\infty}^{\infty} [s_l(t)\exp(i2\pi f_c t) + s_l^*(t)\exp(-i2\pi f_c t)]\exp(-i2\pi ft)dt \\ &= \frac{1}{2}[S_l(f - f_c) + S_l^*(-f - f_c)] \end{aligned} \tag{3.9}$$

Repeating the above procedure for the channel transfer function, $h(t)$ reproduces the above answer, i.e.

$$h(t) = 2\Re\{h_l(t)\exp(i2\pi f_c t)\} \tag{3.10}$$

Note that this only applies to *linear* channels. The factor 2, which has been introduced for convenience, alters relation 3.9 into

$$H(f) = [H_l(f - f_c) + H_l^*(-f - f_c)] \tag{3.11}$$

3.2.2 Band-Pass System Response

The response of a band-pass system, $h(t)$, to a band-pass signal, $s(t)$, can be expressed as

$$r(t) = \int_{-\infty}^{\infty} s(\tau)h(t - \tau)d\tau \tag{3.12}$$

or, in the frequency domain,

$$R(f) = S(f)H(f) \tag{3.13}$$

Since this response is itself a band-pass signal, it can be represented by a low-pass equivalent $r_l(t)$. We will now establish a relationship between the low-pass equivalents $s_l(t)$, $h_l(t)$, and $r_l(t)$. Inserting 3.9 and 3.11 into 3.13 we find

$$R(f) = \frac{1}{2}[S_l(f - f_c) + S_l^*(-f - f_c)][H_l(f - f_c) + H_l^*(-f - f_c)] \tag{3.14}$$

Since all signals are narrowband, the cross terms vanish, yielding

$$R(f) = \frac{1}{2}[S_l(f - f_c)H_l(f - f_c) + S_l^*(-f - f_c)H_l^*(-f - f_c)] \tag{3.15}$$

From 3.9,

$$R(f) = \frac{1}{2}[R_l(f - f_c) + R_l^*(-f - f_c)] \tag{3.16}$$

while 3.15 and 3.16 yield

$$R_l(f) = H_l(f)S_l(f) \tag{3.17}$$

which is the desired result. Accordingly, we can ignore modulation-induced frequency shifts and analyze the signal envelopes only.[18]

3.2.3 Linear Impulse Response

For a linear optical fiber, ignoring losses and nonlinearity, we can easily derive the following propagation equation 2.49

$$\frac{\partial A(z,T)}{\partial z} = \frac{-i}{2}\beta_2 \frac{\partial^2 A(z,T)}{\partial T^2} \tag{3.18}$$

in which β_2 is the group velocity dispersion and A is the signal envelope(low-pass equivalent), c.f. Sec.2.2.2. Fourier transforming yields

$$\begin{aligned} \frac{\partial A(z,\omega)}{\partial z} &= \frac{-i}{2}\beta_2 F[\frac{\partial^2 A(z,T)}{\partial T^2}] \\ &= \frac{-i}{2}\beta_2 (i\omega)^2 A(z,\omega) \\ &= \frac{i}{2}\beta_2 \omega^2 A(z,\omega) \end{aligned} \tag{3.19}$$

which has the formal solution

$$A(L,\omega) = \exp\{\int_0^L [\frac{i}{2}\beta_2\omega^2]dz\}A(0,\omega) \tag{3.20}$$

in which L and ω denote the link length and the low modulation frequency. Evaluating the integral yields

$$A(L,\omega) = \exp(\frac{i}{2}L\beta_2\omega^2)A(0,\omega) \tag{3.21}$$

Thus the transmitted low-pass signal is $A(0,\omega)$, the received low-pass signal is $A(L,\omega)$, and the low-pass response is $\exp(\frac{i}{2}L\beta_2\omega^2)$.

3.3 Linear Dispersion Precompensation

From 3.22, we have

$$R_l(f) = H_l(f)S_l(f) \tag{3.22}$$

where in our case $H_l(f)$ is the optical fiber response, that distorts the signal. This distortion can be removed by inverting the channel response, that is

$$\begin{aligned} R_l(f) &= H_l(f)H_l(f)^{-1}S_l(f) \\ &= S_l(f) \end{aligned} \tag{3.23}$$

Equation 3.23 is fundamental relationship for the dispersion precompensation. Accordingly, we will now examine first the manner in which the optical channel response can be inverted and then the application of such a signal to a laser carrier.

3.3.1 Base-Band Filtering

From 3.21 we observe that the optical channel possesses an equivalent low-pass response given by $\exp(\frac{i}{2}L\beta_2\omega^2)$, which is simply inverted as $\exp(\frac{-i}{2}L\beta_2\omega^2)$. Accordingly, we need only to construct a filter with this response. Besides dispersion precompensation, other filters are normally applied to the optical signal to implement spectral shaping and receiver transfer function precompensation. Cascading these filters with dispersion precompensation leads to

$$\begin{aligned} H(\omega) &= H_{tx}(\omega)H_l(f)^{-1} \\ &= H_{tx}(\omega)\exp(\frac{-i}{2}L\beta_2\omega^2) \\ &= H_{tx}(\omega)\cos\frac{L\beta_2\omega^2}{2} - iH_{tx}(\omega)\sin\frac{L\beta_2\omega^2}{2} \\ &= M(\omega) + iN(\omega) \end{aligned} \tag{3.24}$$

in which all filtering functions besides dispersion precompensation are collected into $H_{tx}(\omega)$

$$\begin{aligned} M(\omega) &= H_{tx}(\omega)\cos\frac{L\beta_2\omega^2}{2} \\ N(\omega) &= -H_{tx}(\omega)\sin\frac{L\beta_2\omega^2}{2} \end{aligned} \tag{3.25}$$

Generally the input data signal is complex (for 2D modulation). Expressing the input accordingly as $I_{in}(t) + iQ_{in}(t)$ leads to

$$I_{out}(t) + iQ_{out}(t) = h(t) \star [I_{in}(t) + iQ_{in}(t)] \tag{3.26}$$

or in the frequency domain,

$$\begin{aligned} I_{out}(\omega) + iQ_{out}(\omega) &= H(\omega)[I_{in}(\omega) + iQ_{in}(\omega)] \\ &= [M(\omega) + iN(\omega)][I_{in}(\omega) + iQ_{in}(\omega)] \\ &= M(\omega)I_{in}(\omega) - N(\omega)Q_{in}(\omega) + i[N(\omega)I_{in}(\omega) + M(\omega)Q_{in}(\omega)] \end{aligned} \tag{3.27}$$

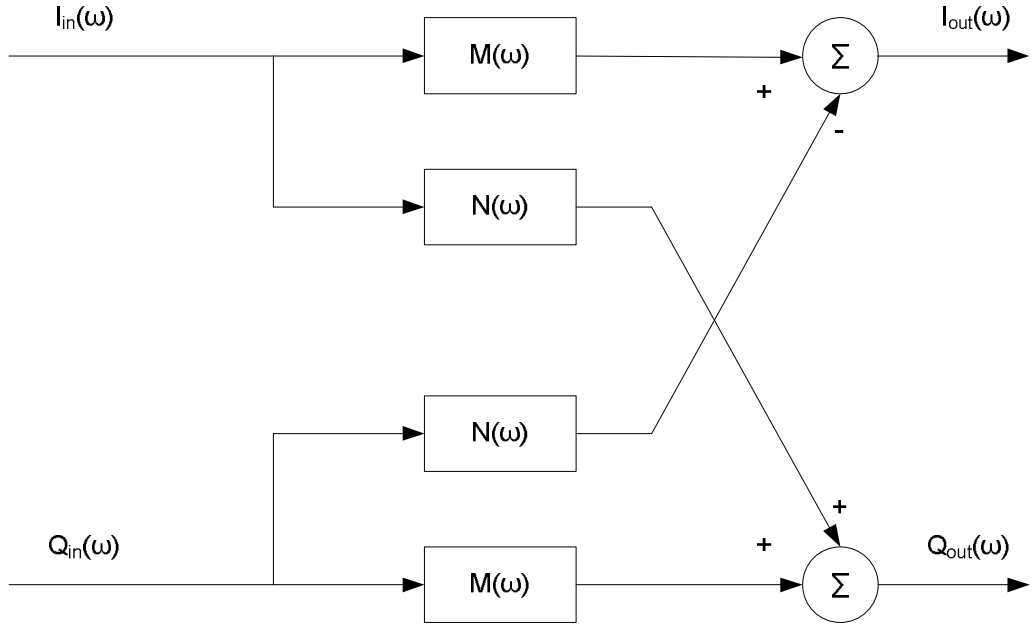

Figure 3.2: Complex filtering of a 2D modulated signal in which four FIR filters produce the complex output.

This transformation can be realized with four FIR filters as demonstrated in Fig. 3.2. For the case of 1D modulation, $Q_{in}(t) = 0$, and one branch in Fig. 3.2 suffices, as illustrated in Fig. 3.3.

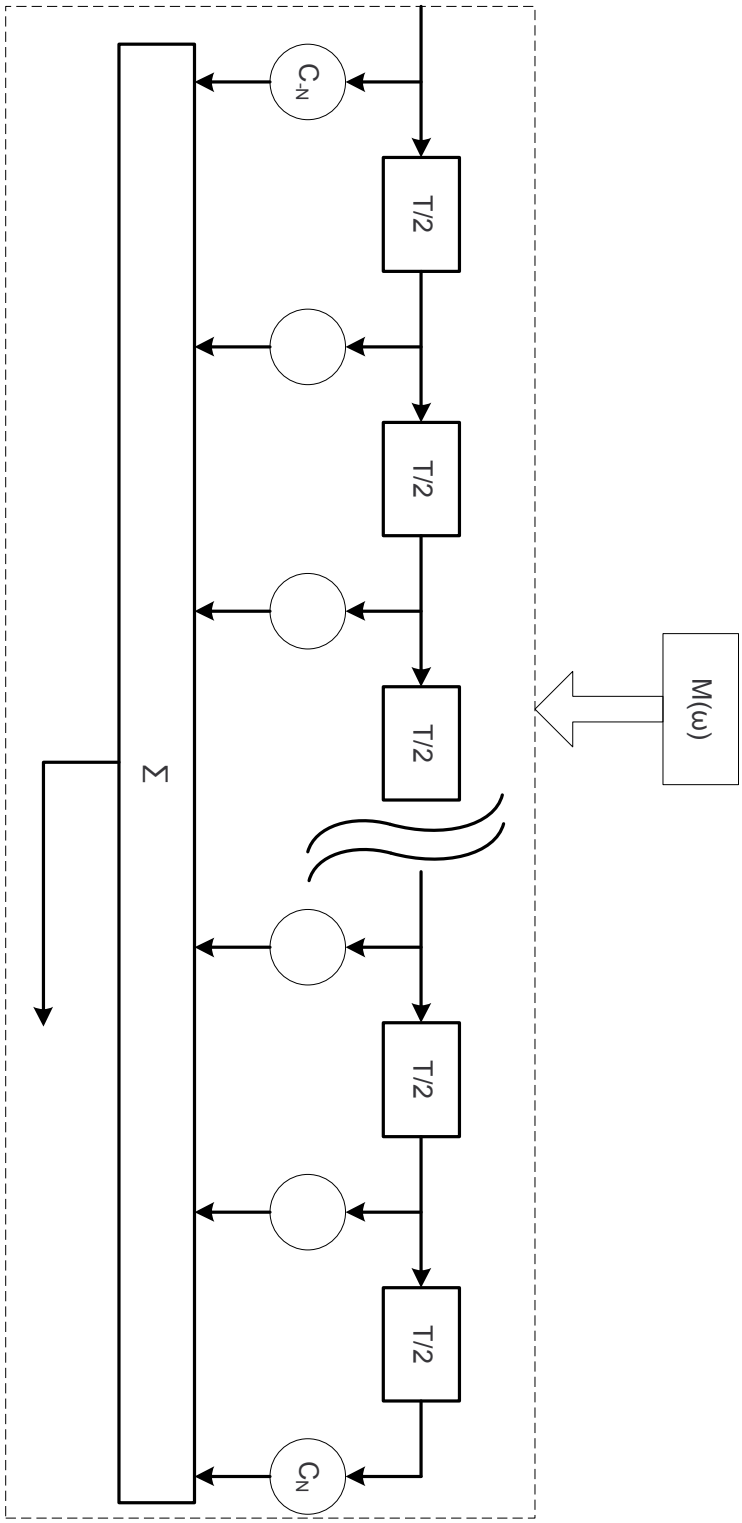

Figure 3.3: FIR filter with $2N + 1$ taps, $T/2$ spaced.

3.3.2 Carrier Modulation

To employ the low-pass signal for carrier modulation and produce the desired transmission signal, we obtain from 3.8, with $s_l(t) = I_{out}(t) + iQ_{out}(t)$,

$$\begin{aligned} s(t) &= \Re\{s_l(t)\exp(j2\pi f_c t)\} = \Re\{[I_{out}(t) + iQ_{out}(t)][\cos 2\pi f_c t + i\sin 2\pi f_c t]\} \\ &= I_{out}(t)\cos 2\pi f_c t - Q_{out}(t)\sin 2\pi f_c t \end{aligned} \tag{3.28}$$

which can be realized with two Mach-Zehnder interferometers and a laser source together with a $\pi/2$ phase delay arranged as in Fig. in Fig. 3.4.

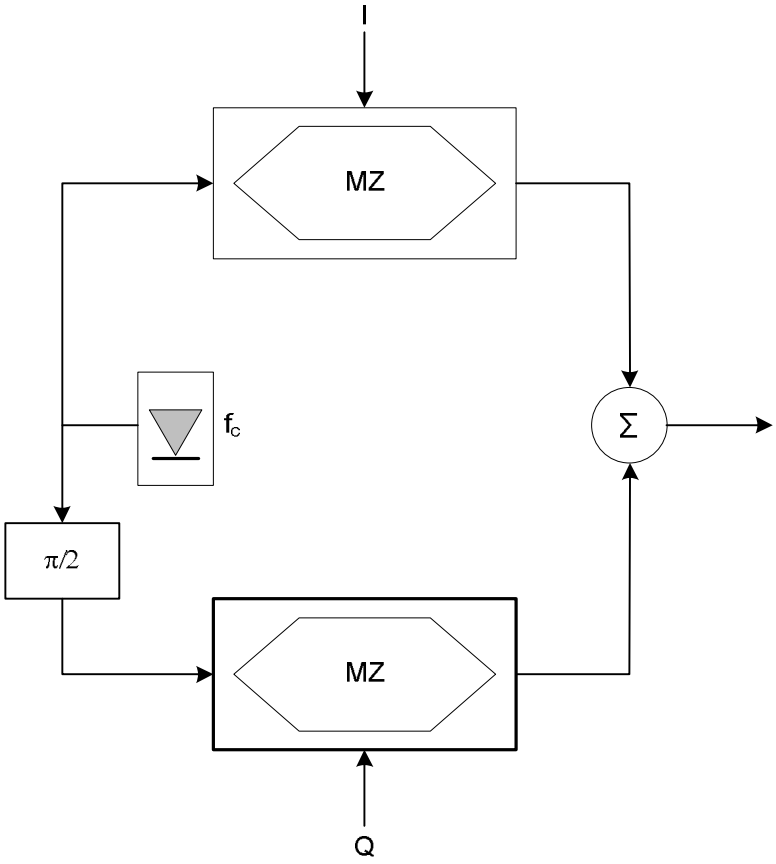

Figure 3.4: 2D modulation of a monochromatic source. The laser output is split into two branches, one of which leads the other by $\pi/2$. The two paths are combined each path is modulated with its corresponding signal(I_{out} or Q_{out}), yielding the result of Eq.3.28.

Chapter 4

NEXT GENERATION MODEMS

4.1 Introduction

In this chapter we analyze Nortel's Next Generation Modulator (NGM) [25] [24]. The modulator is an optical component that implements full dispersion compensation at the transmitter. For this thesis, we have simulated, incorporated and characterized the application of this component to the self-phase modulation compensation. Our design is guided by both physical and commercial constraints, and hence the features of the compensator within the context of a full transmission system will be examined carefully in this chapter.

We start with a general system-level description of the card, including a general theory of operation.

4.2 NGM Layout

The next generation modulator consists of an ASIC called the Warp chip, two driver amplifiers, Mach-Zehnder modulators, and a laser source. A generic functional block diagram of a NGM transmitter is provided in Figure4.1. The digital processing of the signal is performed by the Warp chip, and the result is then converted to an analog signal in the DACs, low pass filtered to restrict the signal to within an assigned bandwidth and then fed to the driver amplifiers. The resulting voltages are then applied to the Mach-Zehnder modulator

electrodes. The CW laser light is divided equally into two branches by a Y-junction, one of which is phase shifted by $\pi/2$ to enable the required complex modulation of the previous chapter3.3.2.

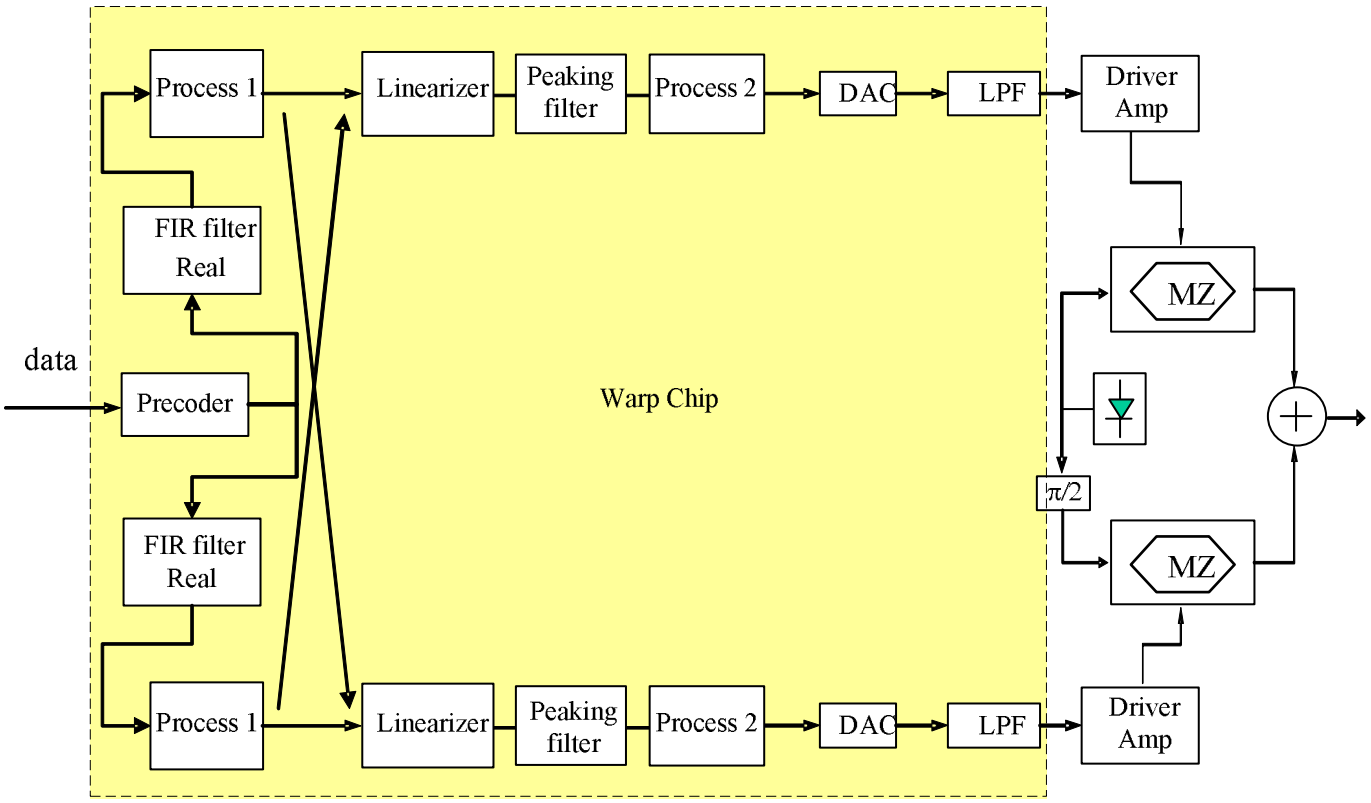

Figure 4.1: NGM block diagram. Blocks that are integrated into the Warp chip, are inside the yellow box. Other connections are implemented through a motherboard bus architecture. A microprocessor that performs DSP calculations is absent from the figure.

The Warp chip receives binary that is coded according to the specific requirements of the communication system application. The encoded signal is then applied to an FIR filter that additionally automatically upsamples the signal, as will be detailed later in this section. The linearizing function provides a nonlinear lookup table that provides a nonlinear mapping for the dual drive modulation in which one Mach-Zehnder modulator

is employed in place of two. The peaking filter finally precompensates distortions from the DAC's and LPF's.

The two main sources of noise present in the precompensator are quantization and clipping noise. The output signal must be confined to certain limits, leading to clipping, but compressing the signal to avoid this effect yields quantization noise. Thus the function of process blocks one and two is to implement an optimal trade-off between these two effects. In particular, we apply the adjustments for SPM compensation in the FIR filter while the linearizer is responsible for signal clipping.

4.3 NGM Operation

The NGM possesses a further microprocessor block that together with accompanying feedback loops is responsible for allocating data to the programable digital processing blocks inside the Warp chip in an optimum fashion. The microprocessor employs a stored program/algorithm to calculate these optimum values based on the state of the feedback signals. The particular feedback parameter, relevant to this study is the net dispersion of the link. From 3.2.3, the desired precompensation formula is quadratic in frequency and we therefore require a single feedback parameter. The NGM determines the value of this parameter based on bit-error-rate information fed back from the receiver. The value chosen is the value of the total dispersion that minimizes the bit error rate. The algorithm is designed to find this minima with the least number of iterations.

4.4 Nonlinear Table

As stated earlier, while the laser carrier is normally modulated by two Mach-Zehnder modulators each with single drive, these can be more inexpensively replaced by a dual drive single Mach-Zehnder modulator. However, as will be explained below, this limits the signal extent. Here, we quantify the extent of the signal by assigning each entry of the signal to a point in the complex plane. This yields a scatter diagram, as in Fig. 4.2 which shows a normalized complex base-band signal after dispersion precompensation filtering.

With two Mach-Zehnder modulators, the laser can be modulated with a signal located

anywhere in the whole complex plane (cartesian modulation), while with a dual drive single Mach-Zehnder (polar modulation) the extent of the signal is limited.

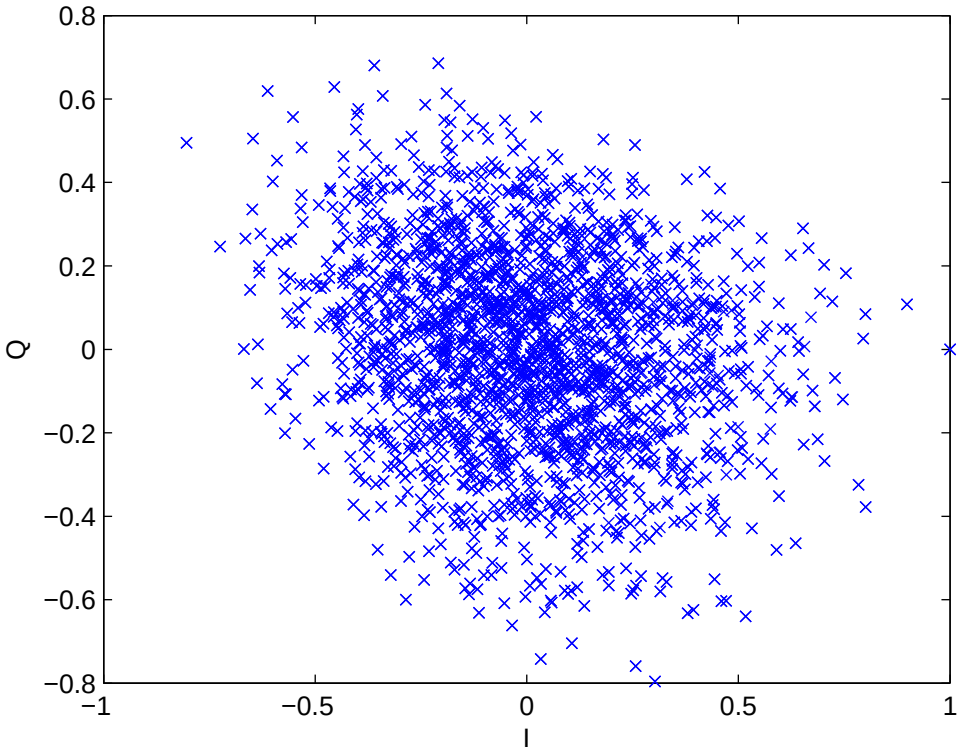

Figure 4.2: A scatter diagram of a normalized complex base-band signal (after removing the DC component). The x-axis represents the real, I, and the y-axis represents the imaginary, Q, part.

For a dual drive Mach-Zehnder the output field is[23]

$$E_{out} = \frac{E_{in}}{2}(e^{i\phi_1} + e^{i\phi_2}) \tag{4.1}$$

Since the complex exponential is periodic, E_{out} is limited to a certain space in the complex (IQ) plane. Thus, the nonlinear table is divided into two parts. The first is to provide a nonlinear mapping between the complex E_{out} and the real values of ϕ_1 & ϕ_2 such that the

output of the nonlinear table can be applied at the Mach-Zehnder modulators. Secondly, the nonlinear table clips its input to within the limits of the accessible complex modulation space. Further, any modulation near the origin of the complex plane will be vulnerable to phase noise and will need large drive for the origin cross over and is therefore also clipped.

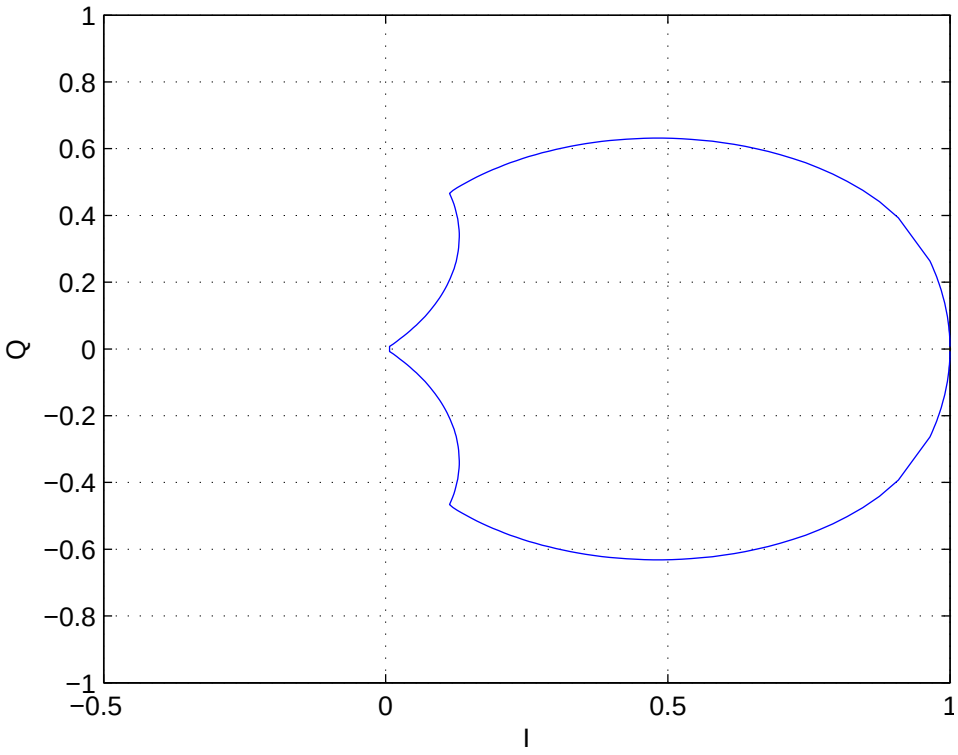

Figure 4.3: Modulation area. Any point outside the ellipse is clipped to the corresponding maximum amplitude.

A typical example of the accessible complex space is shown in Fig. 4.3. That is, the nonlinear table function clips any input points outside this space, and then applies a nonlinear transformation to produce ϕ_1 & ϕ_2.

4.1 is inverted according to appendix B, yielding

$$\phi_1 = \theta + \arccos A \tag{4.2}$$

$$\phi_2 = \theta - \arccos A \tag{4.3}$$

where

$$E_{out}/E_{in} = A\exp(i\theta) \tag{4.4}$$

We must determine the permissible limits between which the SPM compensator will not clip the signal. These limits will be described using polar coordinates. The clipping radius $\rho_{max}(\theta)$ is plotted for a typical case in Fig. 4.3 with $-\pi/2 < \theta < \pi/2$, (note that the real part entering the nonlinear table is always positive). For every point in the signal with a radius $\rho = \sqrt{I^2 + Q2} > \rho_{max}(\theta)$, with $\theta = \arctan Q/I$, ρ is clipped to $\rho_{max}(\theta)$.

4.5 Finite Impulse Response Filter

As mentioned in 3.3.1, precompensation can be applied through finite impulse response, FIR, filters. In NGM and the current application we will employ 1D modulation, which requires two instead of four filters. These two FIR filters and the NGM must accomplish the following requirements:

1. Spectral shaping of the input bit sequence.
2. Precompensation of the receiver filter.
3. Dispersion precompensation.
4. Self-Phase modulation precompensation.

The NGM operates at 2 samples per bit which is the minimum rate satisfying the Nyquist criterion. Since the binary data arrives at a sampling rate of one sample per bit, upsampling is required. Accordingly, zeros are added between samples. Instead of applying this upsampler together with a $T/2$ spaced filter, NGM applies the architecture illustrated in Fig. 4.4 and Fig. 4.5. Here the input is split into two branches with a relative $T/2$ delay. Each branch contains a T spaced filter after which the two branches are combined to yield the equivalent effect (to standard $T/2$ spaced filter) without upsampling and with a delay time T, leading to significant cost savings. One of the filters is termed an odd filter as it produces the $nT/2$ samples with n odd, c.f. Fig.4.4, while the even filter produces the $nT/2$ samples with n even, as in Fig.4.5.

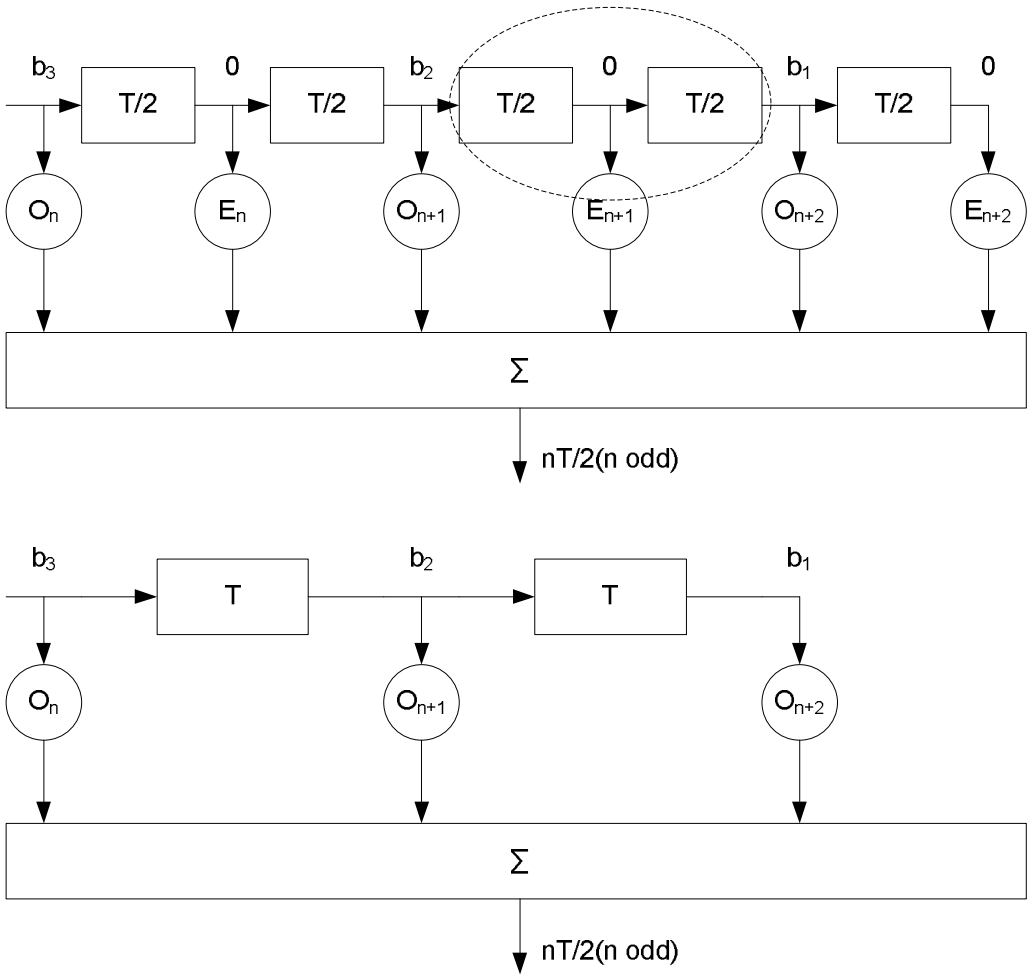

Figure 4.4: The original design is shown above, highlighting the unnecessary even taps for the odd samples. The lower figure demonstrates that less costly equipment can produce the same level of processing.

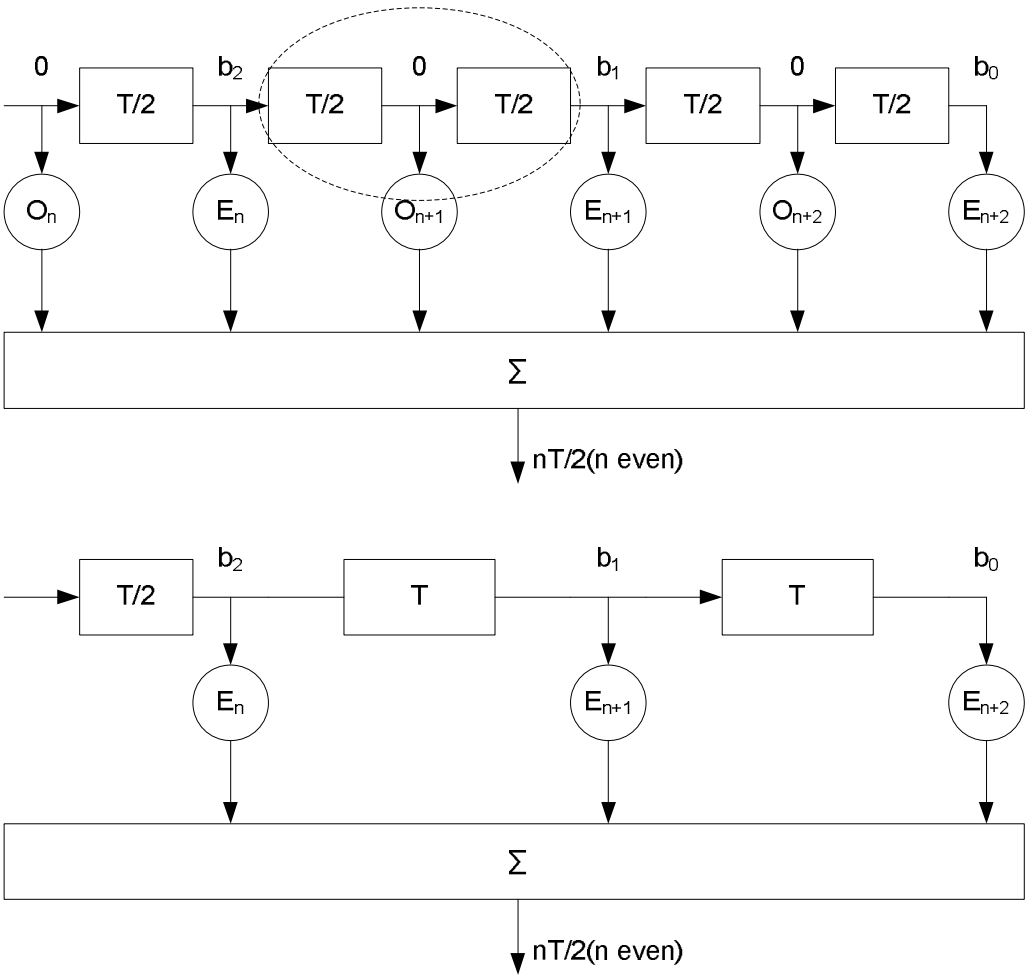

Figure 4.5: As in the previous figure but for the even samples

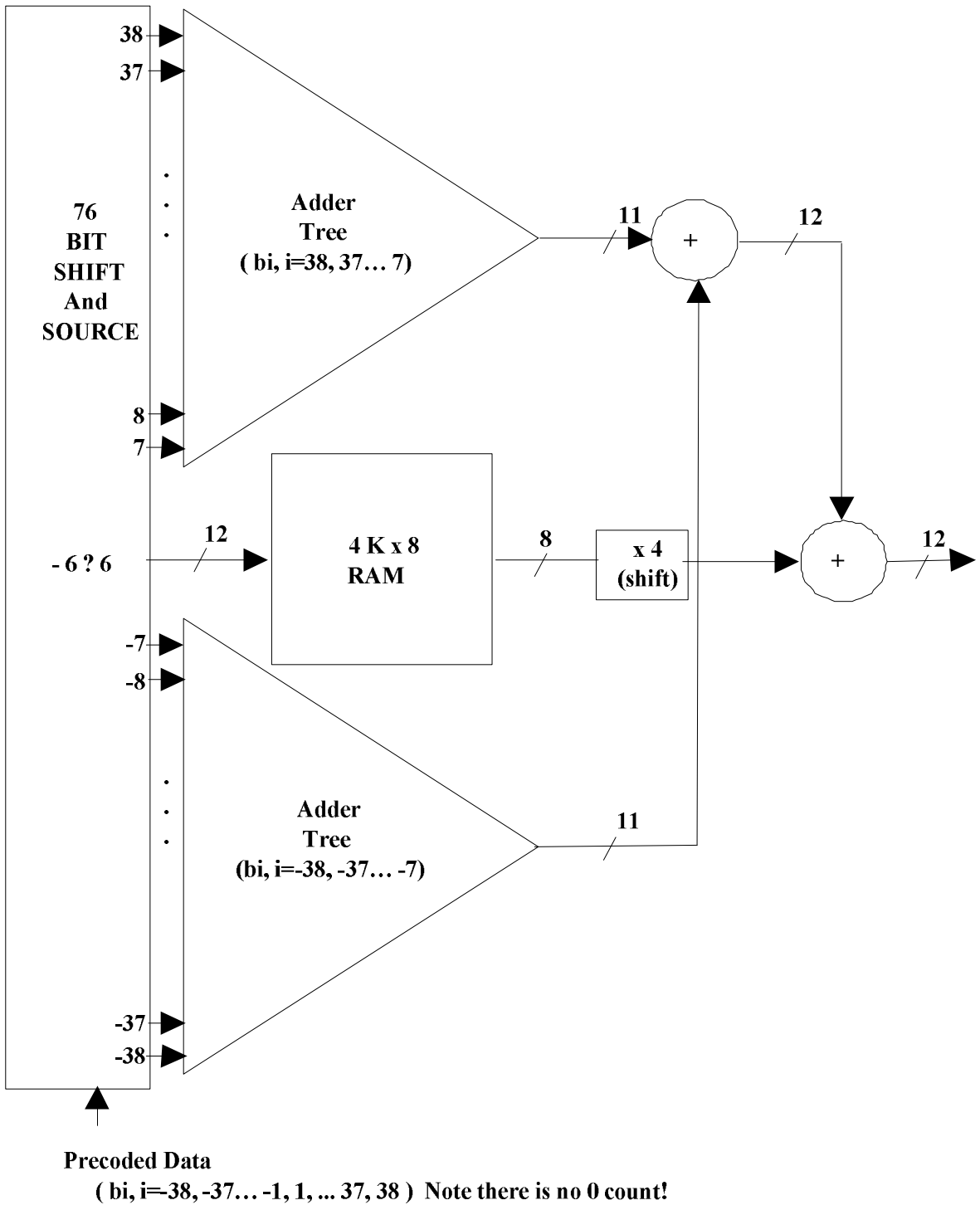

Figure 4.6: A block diagram of the odd/even FIR filter in the NGM. The zero count is omitted for simplicity.

A schematic diagram of the actual FIR filter inside the NGM is shown in Fig. 4.6. This FIR filter has 152 taps, corresponding to 76 taps for each one of the even/odd filters. A Random Access Memory (RAM) which enables self-phase modulation (SPM) compensation, is centered between the filter taps. The RAM replaces the center 12 taps, and therefore possesses a memory size of $2^{12} = 4096$Bytes. Without SPM compensation, the RAM cells are populated by a dot product of each address with the taps the RAM replaces, which yields the same action as the taps it replaced. The actual application of the RAM to SPM compensation will be the topic of the succeeding chapter.

Chapter 5

SELF-PHASE MODULATION COMPENSATION IN NGM

5.1 Introduction

Self-phase modulation is a nonlinear distorting effect that limits the power level in optical communication links. As a result, network designers must employ expensive low noise equipment to ensure a reasonable optical signal to noise ratio at the receiver.

Unlike chromatic dispersion, SPM is a nonlinear process and cannot be inverted by linear filtering. A lookup table that provides unconditioned compensation can however be employed to compensate for SPM. Nortel's NGM is equipped with such a lookup table and can therefore compensate for SPM through EPD.

In this chapter we describe in detail the inclusion of SPM compensation in NGM. We confine our analysis to single channel links, as WDM systems are examined in chapter 6.

5.2 Previous Work

In previous work, it was established that lookup table based SPM compensation can enable a $2 \sim 3$ dB increase in launch power [25] in an NGM system compared with a non SPM compensated system.

In the following part we implement SPM compensation in NGM, propose an improved algorithm and optimize it.

5.3 Nonlinear EPD in NGM

5.3.1 Nonlinear EPD Basic Concept

Electronic pre-distortion applies the inverse of the communication link response through electronic filtering to eliminate link induced distortion so that

$$Y(f) = H^{-1}(f)X(f) \tag{5.1}$$

in which $Y(f)$ is the output of the EPD filter, $X(f)$ is the input, and $H(f)$ is the link response, all in the frequency domain. This equation is valid in the baseband domain as described in chapter 3 for amplitude modulation transmission.

Since SPM is a nonlinear process both the link response and its inverse, are nonlinear. Therefore Eq. 5.1 becomes

$$Y(f) = H^{-1}(f, X)X(f) \tag{5.2}$$

where H in this case is a function of X as well as frequency. Inverse Fourier transforming yields

$$y(t) = \int_{-\infty}^{\infty} h^{-1}(t-\tau, x)x(\tau)d\tau \tag{5.3}$$

We limit our analysis to discrete time quantized signals with N samples per bit period, T, and M quantization levels. Eq. 5.3 then becomes

$$y(nT/N) = \Sigma_{m=-\infty}^{m=\infty} h^{-1}((n-m)T/N, x)x(mT/N) \tag{5.4}$$

where n is the sample index. We subsequently ignore the factor T/N for convenience.

In practical communication links, the link response requires a finite time, so that we can assume that h^{-1} is non-zero only between $-K$ to K. That is, all values of h^{-1} except the $2K$ (without the zero count) within this interval are ignored so that

$$y(n) = \Sigma_{m=n-K}^{m=n+K} h^{-1}(n-m, x)x(m) \tag{5.5}$$

Clearly, 5.5 implies that for a nonlinear EPD filter, with the functional form $h^{-1}(n,x)$, the filter values must change according to the input signal. This can be accomplished by a lookup table for which an input array, $[x(n-K)...x(n+K)]$ is employed as an address to generate the corresponding output, $y(n)$, i.e.

$$y(n) = LUT([x(n-K)...x(n+K)]) \tag{5.6}$$

with

$$LUT([x(n-K)...x(n+K)]) = \Sigma_{m=n-K}^{m=n+K} h^{-1}(n-m,x)x(m) \tag{5.7}$$

The right hand side of this equation filters a data stream with the inverse of the link response, which constitutes the fundamental equation for Nonlinear EPD. For a M level quantization of x and $2K$ input values, the lookup table requires a maximum of M^{2K} elements. In general, to compensate for a nonlinear response of $2K/N$ bauds, a lookup table of $2K$ inputs and M^{2K} entries is necessary.

To evaluate the lookup table entries the inverse response of the given link must be computed and substituted in Eq. 5.7. The link parameters are read into a microcomputer that evaluates the inverse link response and thus the lookup table entries. Hence nonlinear EPD requires

1. A lookup table.
2. Microprocessor.
3. a priori knowledge of necessary link parameters.

5.3.2 Nonlinear Optical Channel Response-Back Propagation

While that the right hand side Eq. 5.7 represents the vector x filtered with the inverse of the full (nonlinear) optical link response, c.f. 5.5, the inverse of the nonlinear optical link, h^{-1}, cannot be evaluated in a closed form for SPM, since the differential propagation equation that includes SPM, Eq. 2.49, is nonlinear and cannot in general be integrated analytically. Accordingly, we employ the concept of optical phase conjugation (OPC).

In particular, when a beam of modulated light that passed through a link is phase conjugated and then retraverses the same link, the distortion imparted by the forward

propagation is removed by the reverse propagation (See appendix C). Thus a signal that is propagated through a certain link and phase conjugated is equivalent to a signal that is filtered with the inverse response of the link, which corresponds to the right hand side of Eq. 5.7.

OPC, however, is only approximate in the presence of attenuation. We therefore modify our formalism through a "back propagation" technique, which means that we solve the propagation equation in reverse time, replacing γ, β_2 and α with $-\gamma$, $-\beta_2$ and $-\alpha$. The initial condition is then to the desired output envelope, x. The solution of 2.49 for these conditions is detailed in appendix C.

5.3.3 Required Link Parameters

In long haul communications the link is divided into segments called spans, each of which is preceded with an amplifier. We thus employ the split step fourier transform method to evolve the pulse through a span, readjust its power and repeat this process for the following span. The required input parameters for each link are then the group velocity dispersion β_2, loss α, γ in Eq. 2.43, the span lengths, $\vec{L}$, and the optical output power of the amplifiers, $\vec{P}$. These application space parameters will be collectively represented below by the vector $\vec{S} = [\gamma, \beta_2, \alpha, \vec{P}, \vec{L}]$.

5.3.4 NGM Capabilities

The EPD filter in NGM employs a binary input ($M = 2$) with a single sample per bit ($N = 1$). Because of the binary input, a simple RAM can store the lookup table. NGM is equipped with a RAM with a 12 bits input ($2K = 12$) that therefore can store $2^{12} = 4096$ entries. Thus this NGM can maximally compensate for nonlinear links with a response that is spread over 12 bauds. The NGM also contains a microprocessor that stores link parameters and computes the required RAM entries. The algorithm for this will be discussed in the following section.

The link parameters, $\vec{S}$, required by the microprocessor to evaluate the inverse channel response are however not always accurately measured at the transmitter side of the link. Later in this chapter we accordingly propose an algorithm that reduces significantly the

required quantity of a priori information. At first, however, we assume that the entire $\vec{S}$ has been determined and that the link is uniform so that the parameters are identical for all spans in the link. Since NGM can be treated as an instance of nonlinear EPD, we can then employ NGM hardware to precompensate SPM.

5.3.5 NGM Limitations

The available RAM size in NGM limits the use of the SPM compensation to channels with a response width of 12 bauds. For optical fiber links, the response width is dependent on the total dispersion of the link, which is in turn directly proportional to the total link length. For example consider G.625 fiber; for 80 km per span, and at a center wavelength 1.55 μm the total spread due to dispersion is 80 km $\times$17 ps/nm/km = 1360 ps/nm. For 10 Gb/sec transmission and therefore a $\sim$ 0.08 nm bandwidth, this spread will be $\sim$ 110 ps or $\sim$ 1.1 baud per span. The RAM size therefore limits the compensation reach to 10 spans in this case.

Besides the RAM size, the bandwidth of NGM and NGM clipping necessarily limit the maximum compensation gain.

Other general limitations are:

- Bit patter dependance.
- DSP calculation power.
- Sensitivity to change of $\vec{S}$.

We address the first two points in this chapter and the last point in the following chapter.

5.4 SPM Precompensation Algorithm in NGM

5.4.1 EPD Filter Details

Fig. 5.1 shows the schematic diagram of the nonlinear EPD filter in NGM, divided into a linear FIR filter with taps and a lookup table (that implements the nonlinear compensa-

tion), which as previously noted accepts the binary data vector $\vec{x}$ and output y.

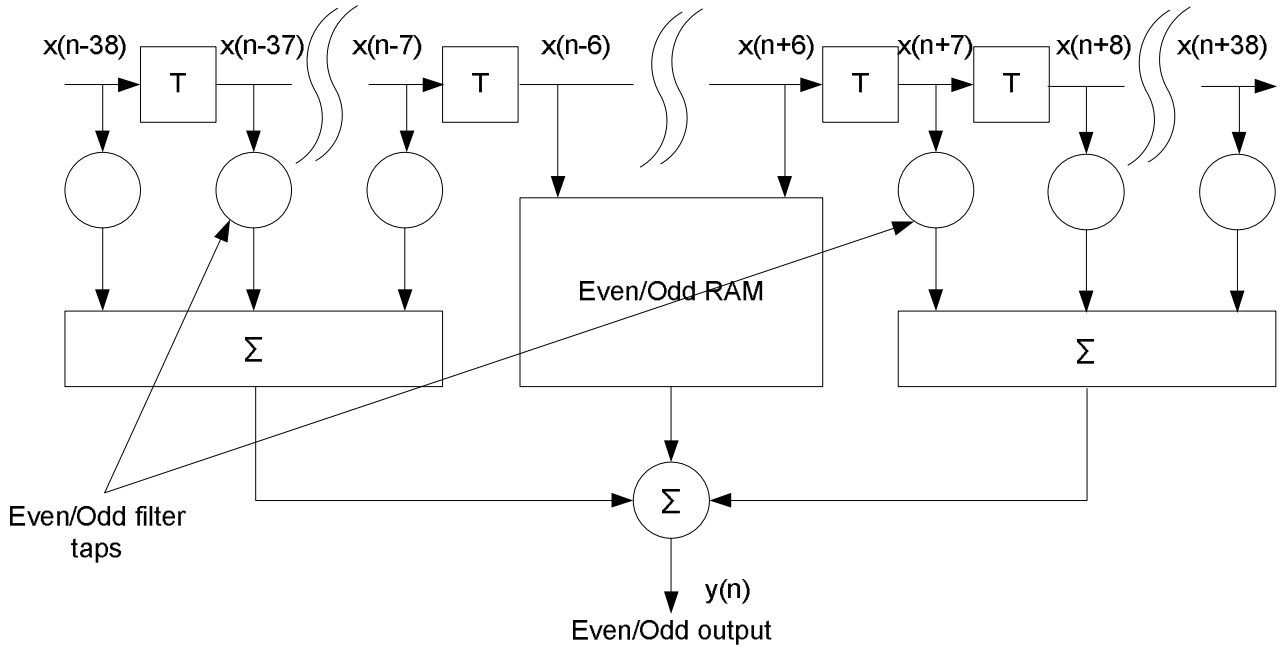

Figure 5.1: A block diagram of the odd/even FIR filter in the NGM. The RAM employed a lookup table is shown together with x samples addressing the RAM.

The linear (chromatic dispersion) compensation is less expensive and complex to implement than nonlinear compensation. Accordingly, we seek to combine a reasonably sized RAM covering 12 bauds for high power medium range operation, with a reasonably size FIR filter covering 76 bauds, enabling low power long range operation.

The center 12 taps of the linear FIR filter are replaced by the RAM yielding the output

$$\begin{aligned} y(n) &= \Sigma_{m=n-38}^{n-7} h_F^e(n-m)x(m) + R^e([x(n-6)....x(n+6)]) \\ &\quad +\Sigma_{m=n+7}^{n+38} h_F^e(n-m)x(m) \qquad (5.8) \\ y(n+1/2) &= \Sigma_{m=n-38}^{n-7} h_F^o(n-m)x(m) + R^o([x(n-6)....x(n+6)]) \\ &\quad +\Sigma_{m=n+7}^{n+38} h_F^o(n-m)x(m) \qquad (5.9) \\ & \qquad (5.10) \end{aligned}$$

Here $n = 1, 2, 3....$, $m \neq 0$ and h_F is the filter response in which the superscript indicates the even/odd correspondence The RAM, R, has two functions as it implements the 12 center taps in the linear case, and nonlinear filtering in the nonlinear case. The linear contribution is,

$$R_L^{e/o}(\vec{x}_R(n)) = \Sigma_{m=n-6}^{n+6} h_F^{e/o}(n-m)x(m) \tag{5.11}$$

where $\vec{x}_R(n) = [x(n-6)...x(n+6)]$ is the RAM input vector.

The final RAM values are obtained by summing the linear and nonlinear contributions

$$R^{e/o} = R_L^{e/o} + R_{NL}^{e/o} \tag{5.12}$$

h_F is the linear filtering that contains the linear inverse (dispersion contribution) of the optical channel, c.f. chapter 3, as well as spectral shaping and receiver filter inversion.

$$h_F(t) = F^{-1}\{H_{Rx}^{-1}(f)H_L^{-1}(f)H_S(f)\} \tag{5.13}$$

$$h_F^e = h_F(k) \tag{5.14}$$

$$h_F^o = h_F(k+1/2) \tag{5.15}$$

in which $k = -38, -37, ..., -1, 1, ..., 37, 38$, H_{Rx}^{-1} is the inverse of the receiver response, $H_L^{-1} = \exp\left(\frac{-i}{2}L\beta_2\omega^2\right)$ represents the inverse of the optical channel and H_S is the spectral shaping function, often chosen to be a sinc function.

H_{Rx}^{-1} and H_S are provisioned. NGM scans the unknown parameter $D = \beta_2 L$ to find its optimum value D_{opt} and then employs it to evaluate H_L^{-1}.

5.4.2 Nonlinear RAM Evaluation

In the previous sections we have explained the manner in which the RAM and filter tap values are populated for linear operation. We now implement a nonlinear SPM compensating filter. We first rewrite Eqs. 5.8 and 5.9 in the form

$$y(n) = \tilde{y}(n) + R_{NL}^e(\vec{x}_R(n)) \tag{5.16}$$

$$y(n+1/2) = \tilde{y}(n+1/2) + R_{NL}^o(\vec{x}_R(n)) \tag{5.17}$$

where

$$\begin{aligned} \tilde{y}(n) &= \Sigma_{m=n-38}^{n-7} h_F^e(n-m)x(m) + R_L^e(\vec{x}_R(n)) \\ &\quad + \Sigma_{m=n+7}^{n+38} h_F^e(n-m)x(m) \qquad (5.18) \\ \tilde{y}(n+1/2) &= \Sigma_{m=n-38}^{n-7} h_F^o(n-m)x(m) + R_L^o(\vec{x}_R(n)) \\ &\quad + \Sigma_{m=n+7}^{n+38} h_F^o(n-m)x(m) \qquad (5.19) \end{aligned}$$

These equations describe the relation between the NGM EPD filter output $y(n)$ and the input $x(n)$. We will employ this relation to evaluate the nonlinear RAM entries in a numerical program. We accordingly rearrange Eqs. 5.16 and 5.17 as

$$\begin{aligned} R_{NL}^e(\vec{x}_R(n)) &= y(n) - \tilde{y}(n) \qquad (5.20) \\ R_{NL}^o(\vec{x}_R(n)) &= y(n+1/2) - \tilde{y}(n+1/2) \qquad (5.21) \end{aligned}$$

Since to every possible value of the input vector $\vec{x}_R$ we can associate a corresponding entry address, we can view the unknowns as the RAM entries that must be obtained from $\vec{x}_R$, $\vec{y}$ and $\vec{\tilde{y}}$, where the last two vectors are functions of the components of $\vec{x}_R$. The RAM then possess a minimum of $2^{12} = 4096$ entries, so this calculation must be performed at least 4096 times. This can be done in a single computation by constructing an artificial input array $\vec{x}_A$, evaluating the associated vectors $\vec{y}$ and $\vec{\tilde{y}}$ and finally substituting these values into 5.20 and 5.21 for each entry. Clearly for $\vec{x}_A$ to possess at least 4096 entries, all 4096 RAM entries must be populated. Further, $\vec{x}_A$ must yield a minimum of 4096 different combinations of the $\vec{x}_R$ that span all possible 12 (the length of $\vec{x}_R$) bit values. This can be done with e.g. a maximal length pseudo random bit sequence generator of order 12. (PRBS, see appendix A)

To evaluate $\vec{\tilde{y}}$ we substitute $\vec{x}_A$ into Eqs. 5.18 and 5.19 after determining $R_L^{e/o}$ and h_F from the value of D_{opt}. Further, $\vec{y}$ is calculated from $\vec{x}_A$ and $\vec{S}$ through back propagation as described before. Back propagation does not directly yield the data vector $\vec{x}_A$ as spectral shaping and receiver filter inversion must first be applied to the input signal $\vec{x}_A$. We term the resulting signal $\vec{y^o}$, with

$$\begin{aligned} y^o(n) &= \Sigma_{m=n-33}^{n+33} h_F^{o-e}(n-m)x_A(m) \qquad (5.22) \\ y^o(n+1/2) &= \Sigma_{m=n-33}^{n+33} h_F^{o-o}(n-m)x_A(m) \qquad (5.23) \end{aligned}$$

for $n = 1, 2, ...2^{12}$ and $k = -33, -32, ..., 31, 32$ and

$$h_F^o(t) = F^{-1}\{H_{Rx}^{-1}(f)H_S(f)\} \quad (5.24)$$

$$h_F^{o-e} = h_F^o(k) \quad (5.25)$$

$$h_F^{o-o} = h_F^o(k + 1/2) \quad (5.26)$$

Signal conditioning is further applied before and after back propagation to enhance the performance as will be described shortly.

Finally, we substitute $\vec{y}$, $\vec{\tilde{y}}$, n and $\vec{x}_A$ in Eqs. 5.20 and 5.21 and to obtain the desired nonlinear RAM that compensates for the optical link characterized by $\vec{S}$. Since $n = 1, 2, 3....2^{12}$, the address $[x(n-38)....x(n+38)]$ at the input of the EPD filter can refer to indexes of x that are either negative or larger than 2^{12}. In these cases we act as if x is periodically extended such that e.g. $x(1+2^{12}) = x(1)$. Fig. 5.2 summarizes this procedure and the SPM compensation algorithm.

5.4.3 Algorithm Modification

Increasing PRBS order

We now consider Fig. 5.2, which relates to a 2^{15} maximum length sequence with $2^{15-12} = 8$ instances of each $\vec{x}_R$. Each instance is extended differently outside the 12 bit window. Ideally if two pulse streams share the same 12 bit address, they will map to same value of a corresponding value of $\vec{y} - \vec{\tilde{y}}$. In practice, however, if the response exceeds 12 bits, two streams with the same 12 bit address will yield different values for $\vec{y} - \vec{\tilde{y}}$ if the address occurs with different neighboring pulse sequences. Substituting the new values of $\vec{x}_A$, $\vec{y}$, and $\vec{\tilde{y}}$ in Eqs. 5.20 and 5.21 therefore yields a cluster of 8 values for each address. We employ the arithmetic mean of these values as the nonlinear contribution of the address in order to reduce the bit pattern dependence and simultaneously the overall penalty.

Clipping Reduction

As mentioned in chapter 4, due to the finite dynamic range of analog to digital samplers, our signal is confined to a portion of the complex plane. In the absence of SPM compensation, the data is optimally centered within the complex plane by determining the

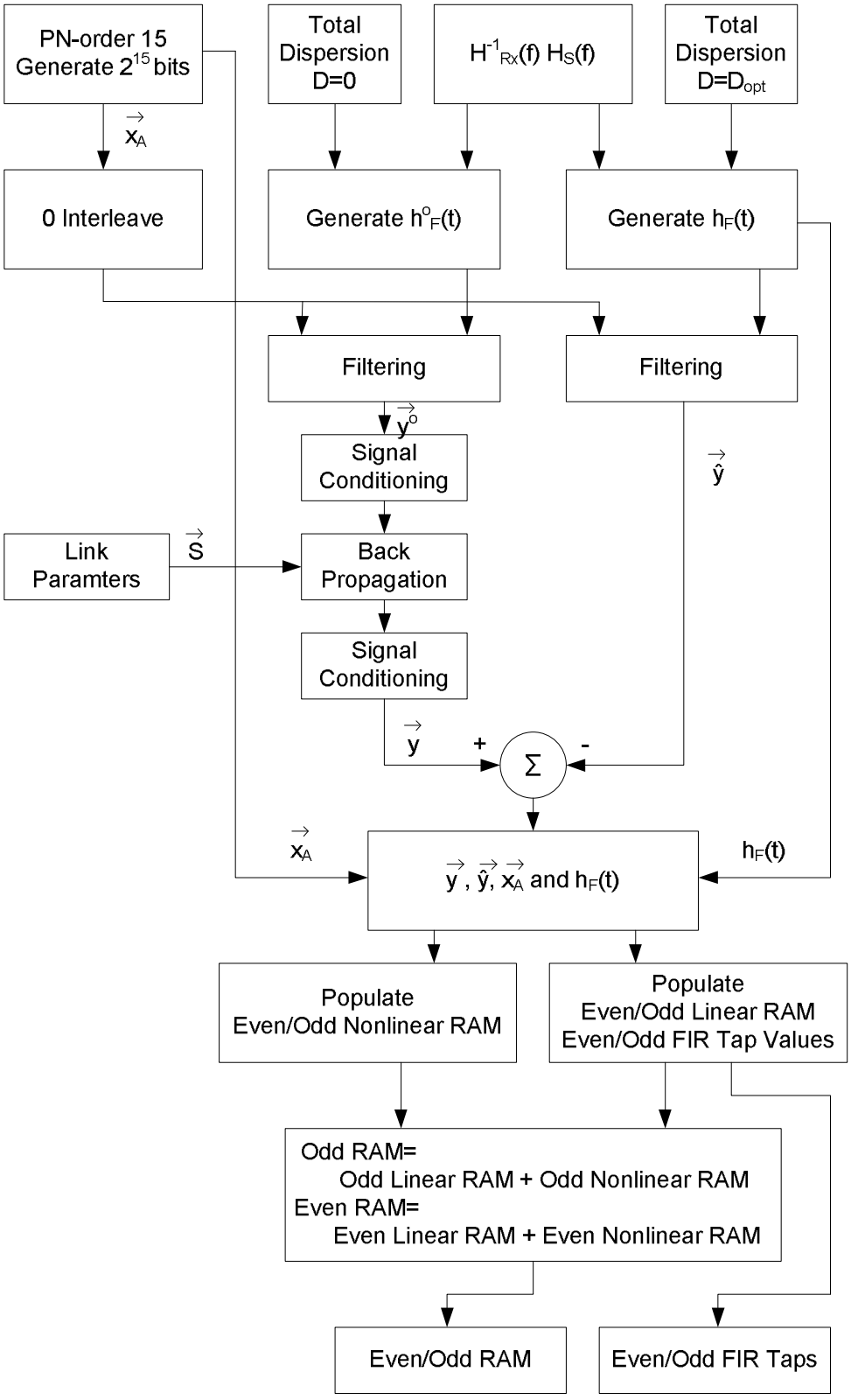

Figure 5.2: Algorithm for populating EPD filter with linear and nonlinear corrections.

best compromise between clipping and quantization noise. After SPM compensation, this optimization is however largely removed due to the phase rotation bias of the modulated field waveform associated with SPM.

The nonlinear table is designed to optimize the performance of NGM which employs differential drive modulation. It centers and scales the signal in the IQ plane in order to minimize clipping of the optical electric field. This optimization is generic for linear dispersion compensation and is nearly unchanged over a wide range of dispersion values. SPM precompensation introduces a phase rotation of the signal in the IQ plane since SPM is an intensity dependent phase term, leading to additional clipping in the nonlinear table. If the signal is rotated in IQ plane, however, the clipping can be minimized, preserving the signal fidelity without affecting the phase-insensitive square law detector. The chosen rotation angle is the RMS of the sample's rotation and, as we will find presently, equals the α_c parameter of section 5.6. Fig. 5.3 displays a non SPM compensated signal before and after correction from the nonlinear table in the complex plane for an 8×87km G.625 fiber system and 3dBm launch power. Note that the blue circles are the signal values before nonlinear table is applied and red x's are after. Fig. 5.4 is the same as 5.3 but with SPM compensation included in the FIR filter before the prerotation. Finally Fig. 5.5 is the same as 5.4 but with the prerotation included.

Aliasing Noise

While we sample at 2 SPB in constructing the RAM values, SPM yields a frequency spread and therefore constitutes a potential source of aliasing noise in numerical back propagation. While the test signal is often upsampled to a higher SPB before optical phase conjugation and then filtered to remove the signal components beyond the bandwidth and downsampled back to 2 SPB, we have found that for the relevant power levels, this aliasing noise is negligible. Therefore, we can significantly reduce the DSP power by performing the numerical processing at 2 SPB.

Figs. 5.6, 5.7, and 5.8 illustrate these considerations by displaying the performance with and without aliasing noise. The performance difference is less than 0.05 dB.

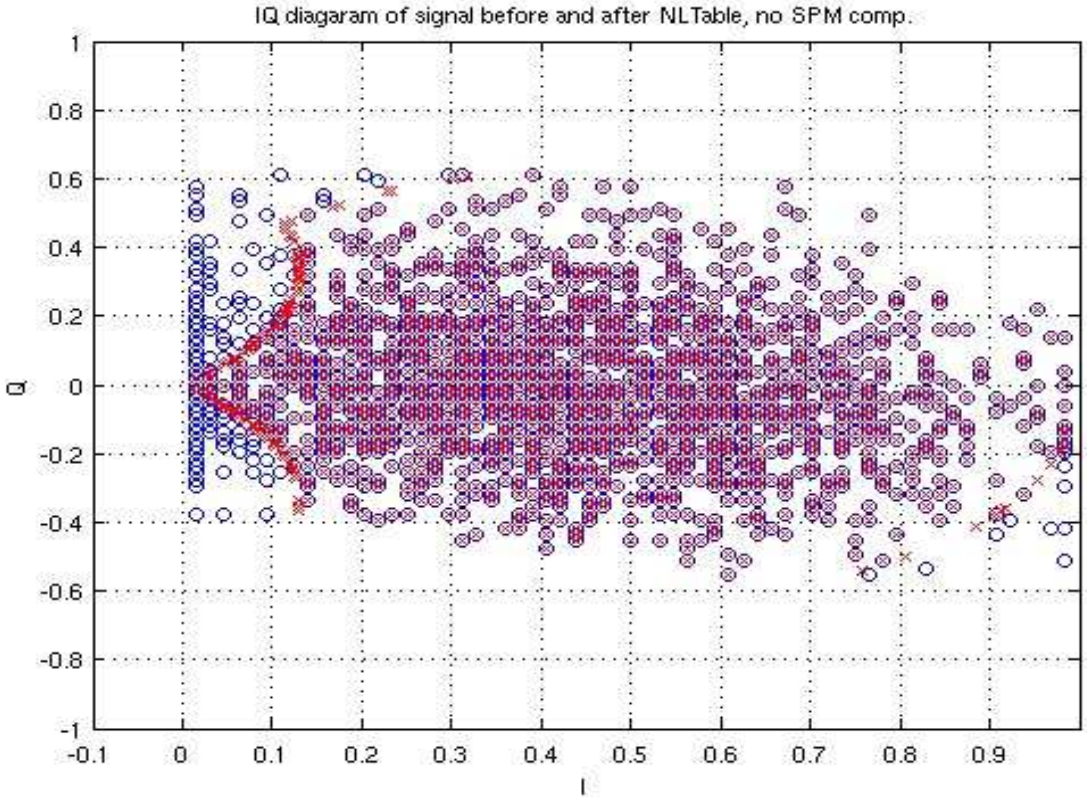

Figure 5.3: Signal scatter diagram before (blue circles) and after (red cross) the nonlinear lookup table is applied for a system with 8 87 km spans, and a 3 dBm launch power in the absence of SPM compensation.

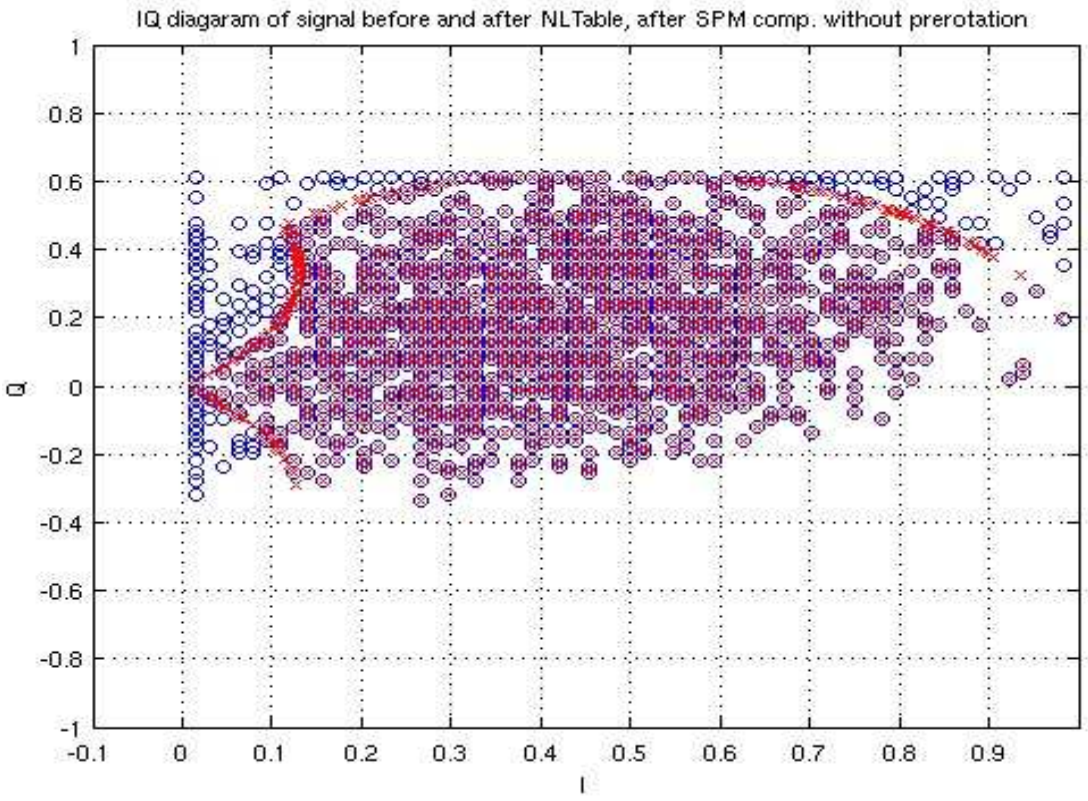

Figure 5.4: As in the previous figure but with SPM compensation in the absence of pre-rotation.

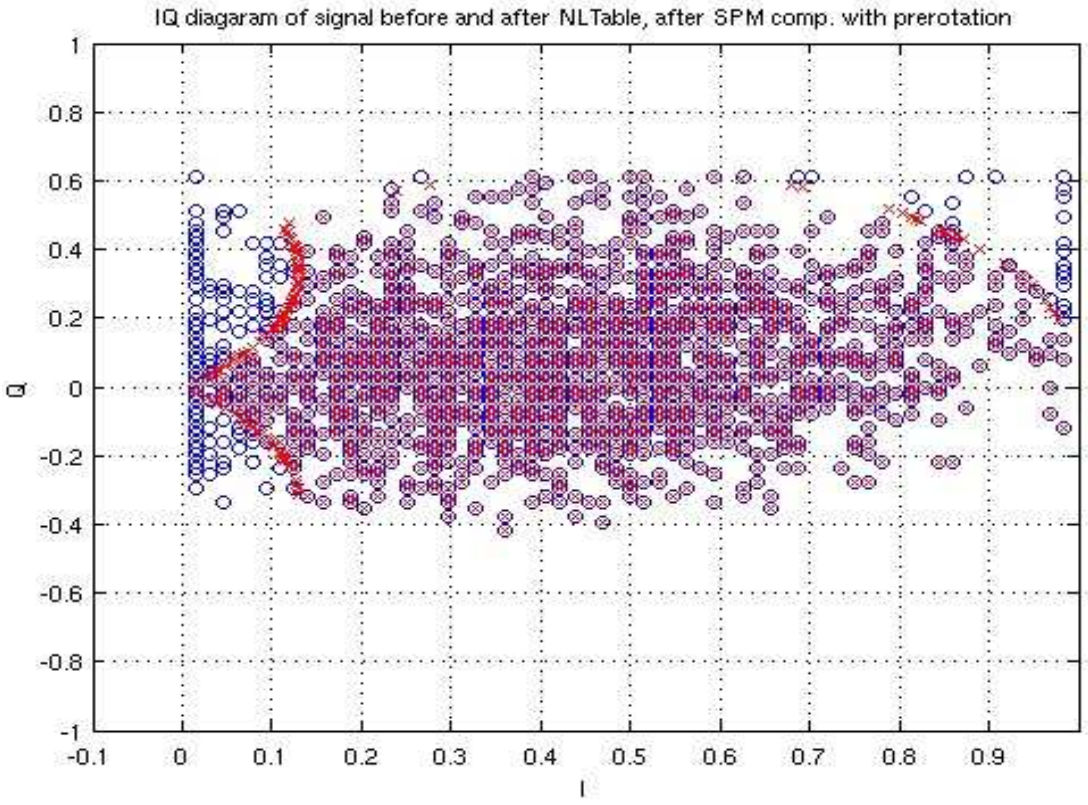

Figure 5.5: As in Fig. 5.3 with both SPM compensation and prerotation

5.5 Application Space

To determine the compensation efficiency, we modified the software program employed by Nortel for NGM system testing. This program simulates the card and the fiber link, including all optical filters and receiver effects. The output of the simulation is the optical signal to noise ratio, ROSNR, required for a given bit error rate, BER. The maximum acceptable BER for the current level of forward error correction (FEC)is 3×10^{-3}.

We first tested our algorithm for ideal, medium reach systems. in which the fiber parameters (G.652 fiber) are uniform throughout the link and the length of all spans is 87 km. The power level at the output of each amplifier is identical for all the amplifiers and is adjusted for each calculation. For greater powers, the SPM distortion increases and we therefore expect the ROSNR to grow with launch power, as is verified by a plot of ROSNR versus launch power. The optimum launch power is the power at which the slope of this curve is unity so that the marginal improvement in ROSNR delivered to the receiver is equal to the marginal SPM impairment. The SPM compensation increases optimum launch powers. Accordingly, we employ this derivative as a measure of the gain measure in units of dB.

Figs. 5.6, 5.7, and 5.8 display the ROSNR in dB versus optical launch power in dBm for 8, 6, and 4 span systems. From these figures, the gain is approximately $2 \sim 3$ dB while the aliasing noise is within a 0.05 dB range, so that no upsampling is required. Finally, in Fig. 5.9, we plot the ROSNR versus launch power for SPM compensated with and without prerotation (see the previous section). This figure indicates that prerotation enhances the ROSNR by more than 2 dB.

5.6 Reduction of Parameters of OPC

We now simplify the back propagation algorithm in order to reduce of the number of required link parameters in $\vec{S}$, to a single dimensionless parameter, α_c. defined as

$$\alpha_c = \gamma \times \sum_{i=1}^{N} P(i) \times L_{eff}(i) \tag{5.27}$$

with

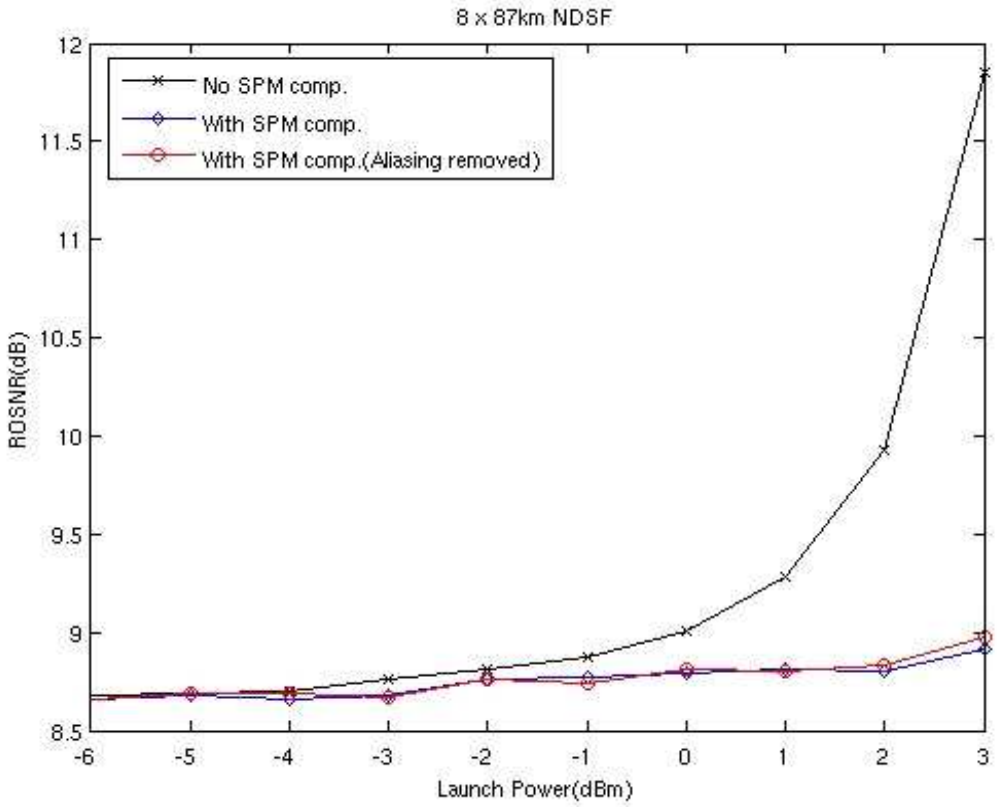

Figure 5.6: The required optical signal to noise ratio, ROSNR, for 10^{-3} bit error rate transmission versus launch power for an eight 87 km span G.625 system and (a) no SPM compensation, SPM compensation with (b) and without (c) removal of aliasing noise.

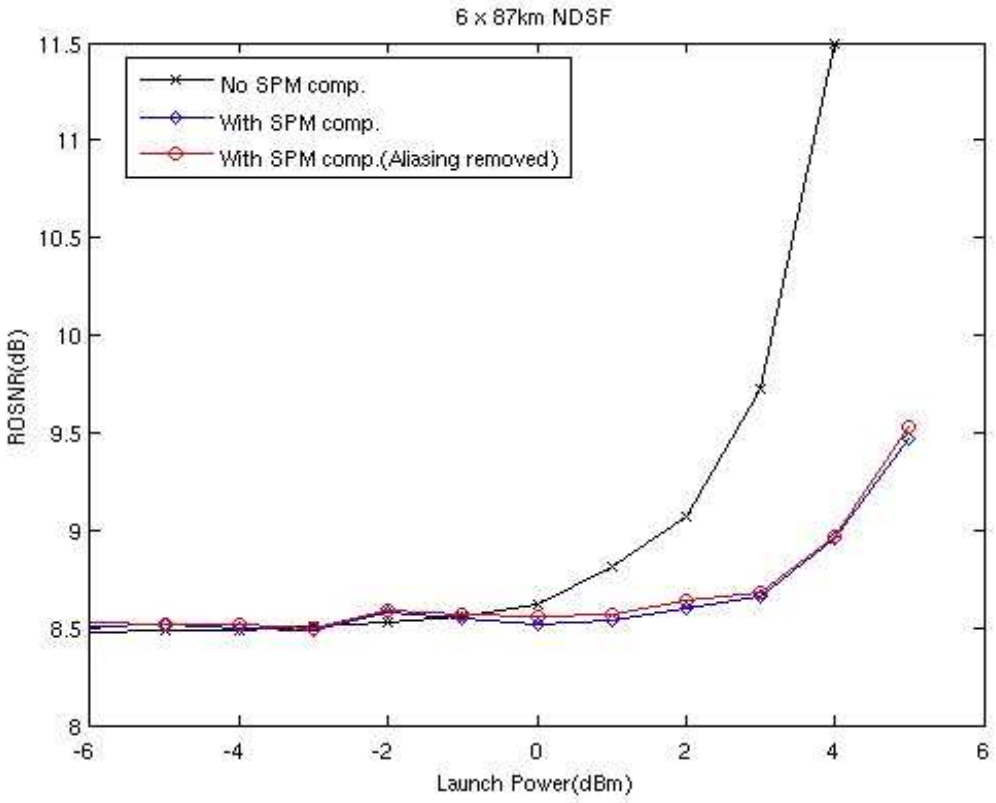

Figure 5.7: As in the previous figure but for a six 87 km span G.625 system.

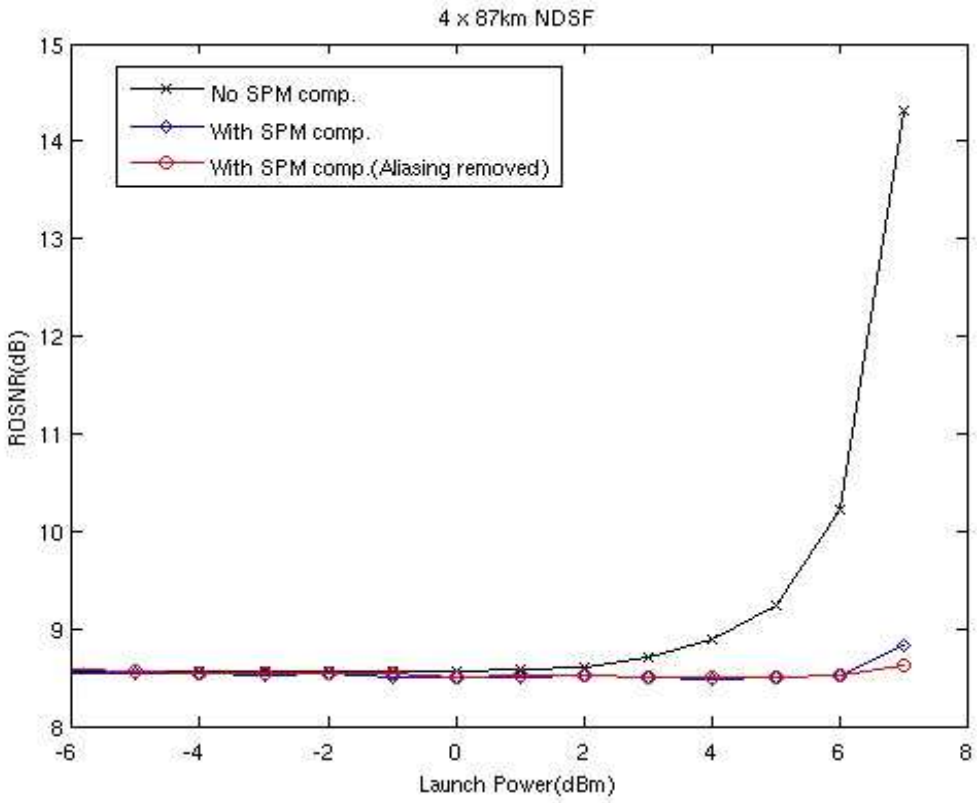

Figure 5.8: As in Fig. 5.6 but for a four 87 km span G.625 system.

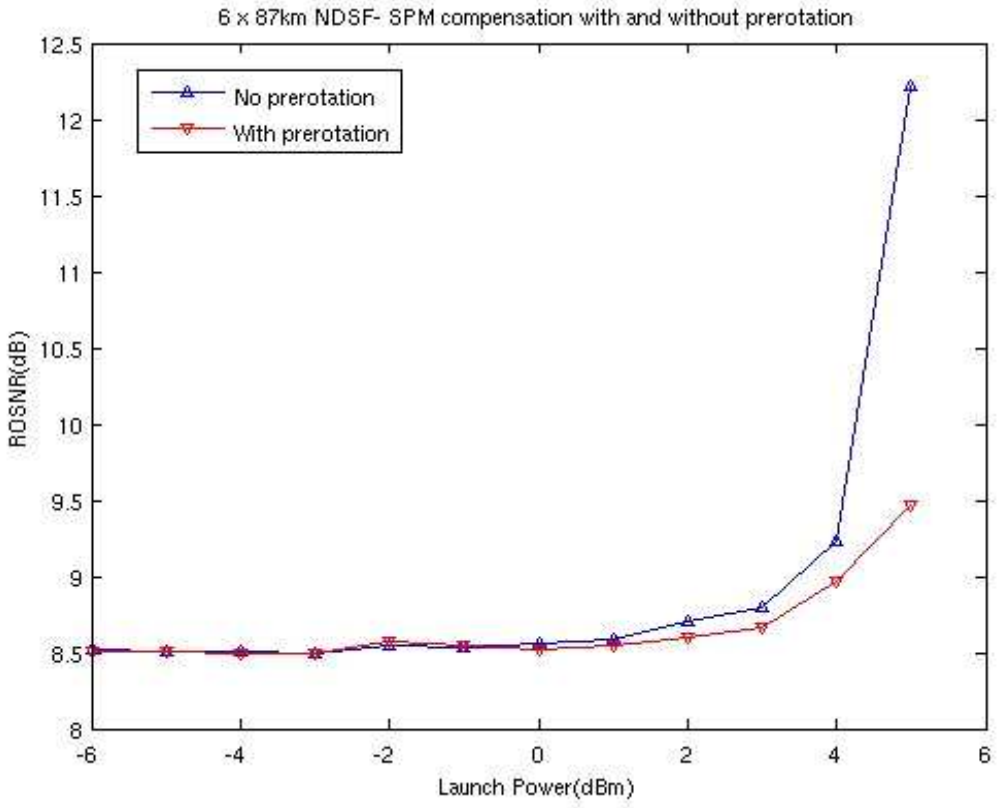

Figure 5.9: As in Fig. 5.6 but for a six 87 km span G.625 system in the presence of SPM compensation with and without prerotation.

γ Nonlinearity parameter, see equation 2.43

$L_{eff}(i)$ Effective length [19] of span i

N Number of spans in the link

$P(i)$ Average channel power launched into span i

The link is modeled as a single span that introduces a nonlinear phase α_c, over one split step (the number of steps can be increased in a tradeoff between accuracy and DSP power). Defining

$$\hat{D} = \frac{-i}{2} \times D_{opt} \times \omega^2 \tag{5.28}$$

$$P_{sig} = \langle |\vec{y}^o|^2 \rangle = \frac{1}{T} \times \int_T |\vec{y}^o|^2 dt \tag{5.29}$$

$$A = \frac{\vec{y}^o}{\sqrt{P_{sig}}} \times \exp -i\alpha_c \tag{5.30}$$

in which D_{opt} is the optimum dispersion, ω is the radial frequency and λ is the wavelength, our algorithm then can be expressed as

$$B = F^{-1}\{\exp \frac{\hat{D}}{2} F\{A\}\} \tag{5.31}$$

$$C = F^{-1}\{\exp \hat{D} F\{A\}\} \tag{5.32}$$

$$\hat{N} = -i \times \alpha_c \times \frac{1}{4} \times \{|A|^2 + 2 \times |B|^2 + |C|^2\} \tag{5.33}$$

$$\vec{y} = \sqrt{P_{sig}} \times F^{-1}\{\exp \frac{\hat{D}}{2} \times F\{\exp \hat{N} \times B\}\} \tag{5.34}$$

Here A is the normalized prerotated signal, B and C are the result of linear propagation of A over a half and a full link distance respectively, that is they represent the normalized prerotated signals at the beginning, middle, and the end of bulk material for exclusively linear propagation. From A,B and C, we employ trapezoidal integration [17] to calculate the average of the linear signal over the fiber. Weighting with α_c yields the approximate

nonlinear operator, where the approximation enters in that we have employed only linear propagation to determine the variables that enter the nonlinear phase contribution. This is valid in regimes where chromatic dispersion is the dominant process, as in our current study. Finally the nonlinear operator is applied between the two dispersion steps, consistent with operator symmetrization, and finally the resulting pulse is multiplied by channel power. This algorithm is discussed further in appendix D.

In practice, two steps of this technique are generally sufficient, given the non-ideal behavior of the NGM, such as its clipping and bandwidth limits, Figs. 5.10, 5.11, and 5.12 display ROSNR versus launch power for uncompensated, standard compensated and compensated with α_c, in 8, 6 and 4 span G.625 systems.

In this case, we employ half the value of both D_{opt} and α_c to calculate $\vec{y}$, after which the remainder of D_{opt} and α_c is applied with $\vec{y}$ as the new input variable, $\vec{y}^o$. This method leads to a decreased error and provides additional freedom associated with the division of D_{opt} and α_c between the two steps, as will be discussed in the following chapter. Each α_c step requires 3 fast Fourier transforms (FFT) and 3 inverse FFTs, which is 20 fewer DSP operations compared to our previous algorithm.

In Fig. 5.13 we display the ROSNR for uncompensated SPM as a function of the α_c of the link, for 4, 6, and 8 span systems. The ROSNR here reflects the SPM-induced nonlinear penalty. Since three systems yield similar graphs, α_c can be considered a measure of the system nonlinearity. This observation is further justified by Fig. 5.14, which graphs the difference between $D_{opt} - D_{total}$ between the optimally compensated dispersion obtained with the NGM (some of the SPM penalty can be compensated by dispersion) and the total channel chromatic dispersion versus α_c for different systems. From 5.14 we again conclude that the dispersion mismatch can be accurately quantified by the value of the α_c parameter.

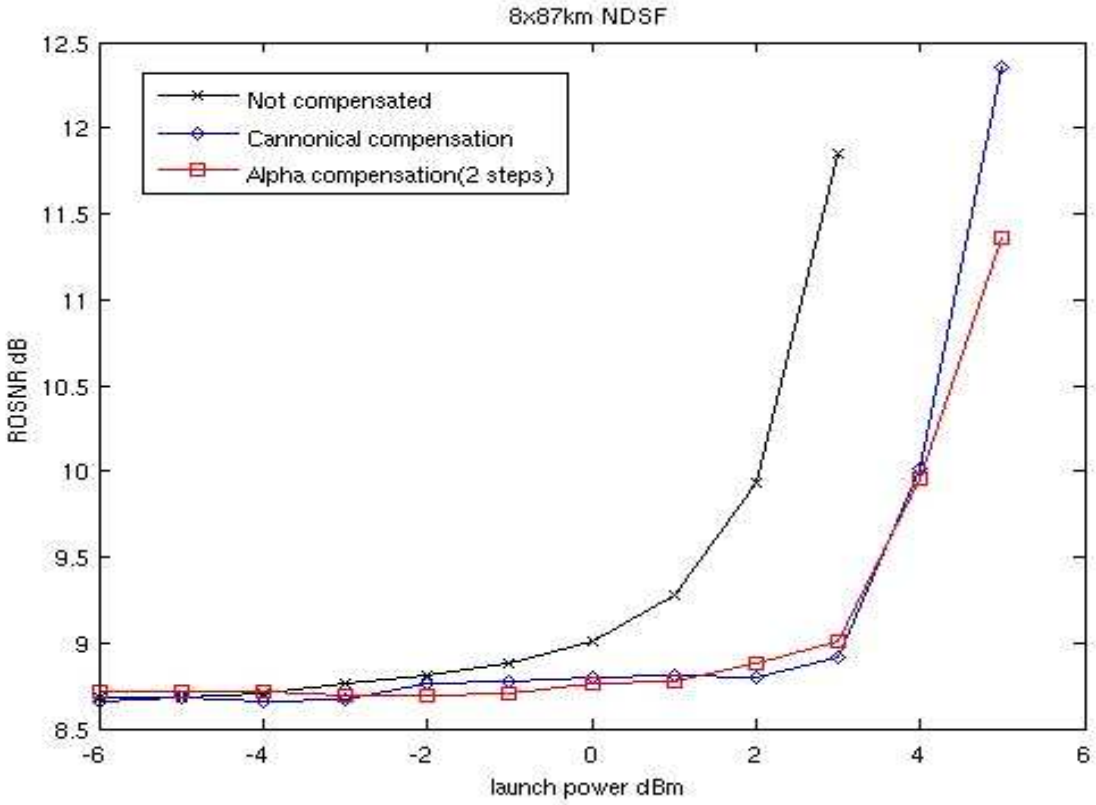

Figure 5.10: As in Fig. 5.6 but for an eight 87 km span G.625 system for (a) no SPM compensation, (b) standard SPM compensation, and (c) a numerical 2 step α_c compensator

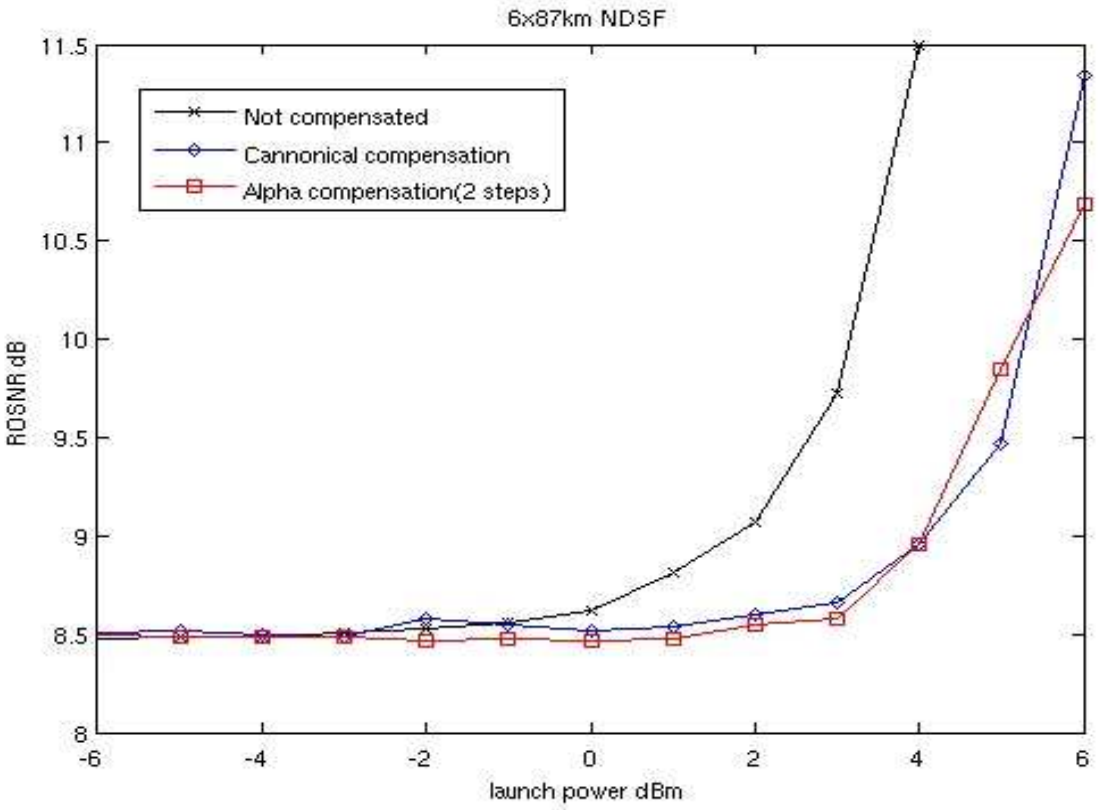

Figure 5.11: As in the previous figure but for a six 87 km span G.625 system.

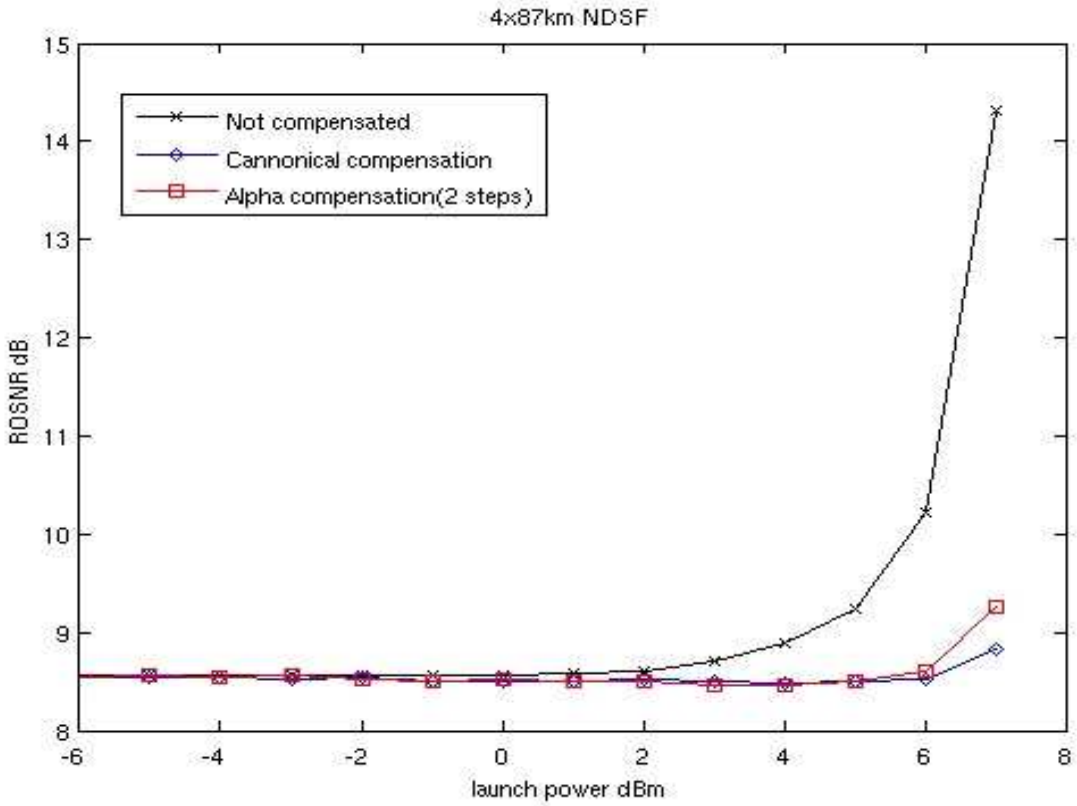

Figure 5.12: As in Fig. 5.10 but for a four 87 km span G.625 system.

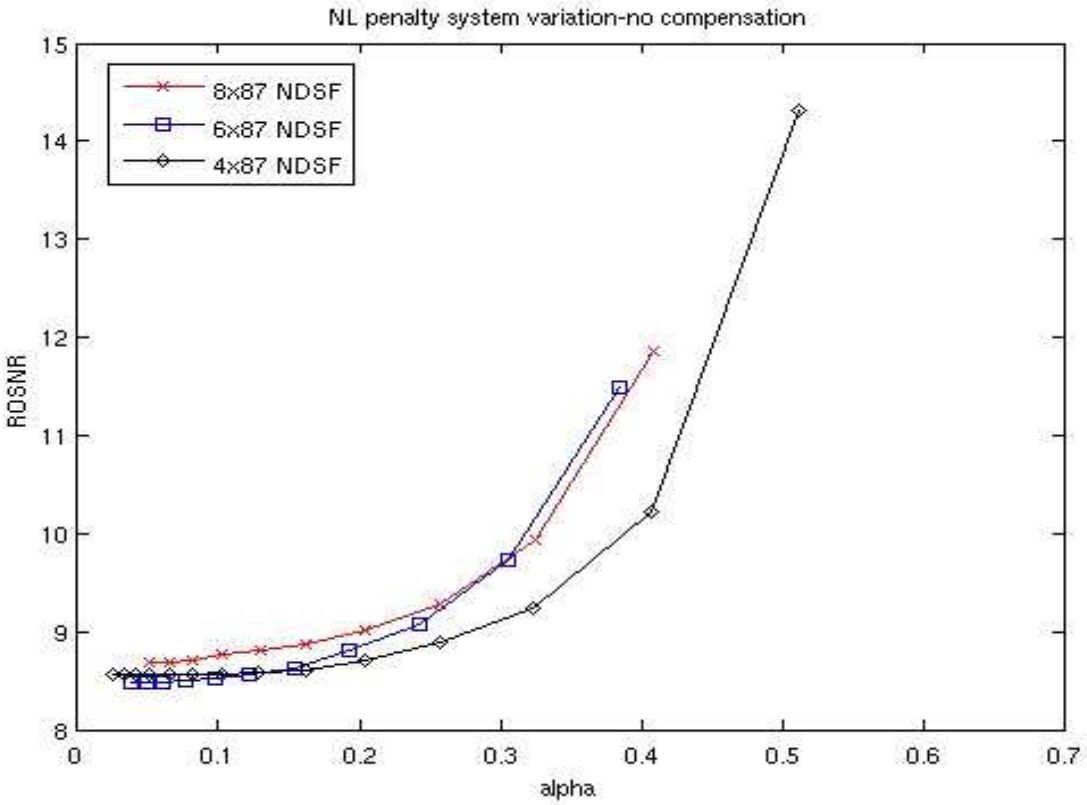

Figure 5.13: Required optical signal to noise ratio, ROSNR, for a 10^{-3} bit error rate transmission versus α_c for eight, six and four 87 km span G.625 system. The agreement between the three graphs indicates that the SPM penalty here depends almost exclusively on α_c.

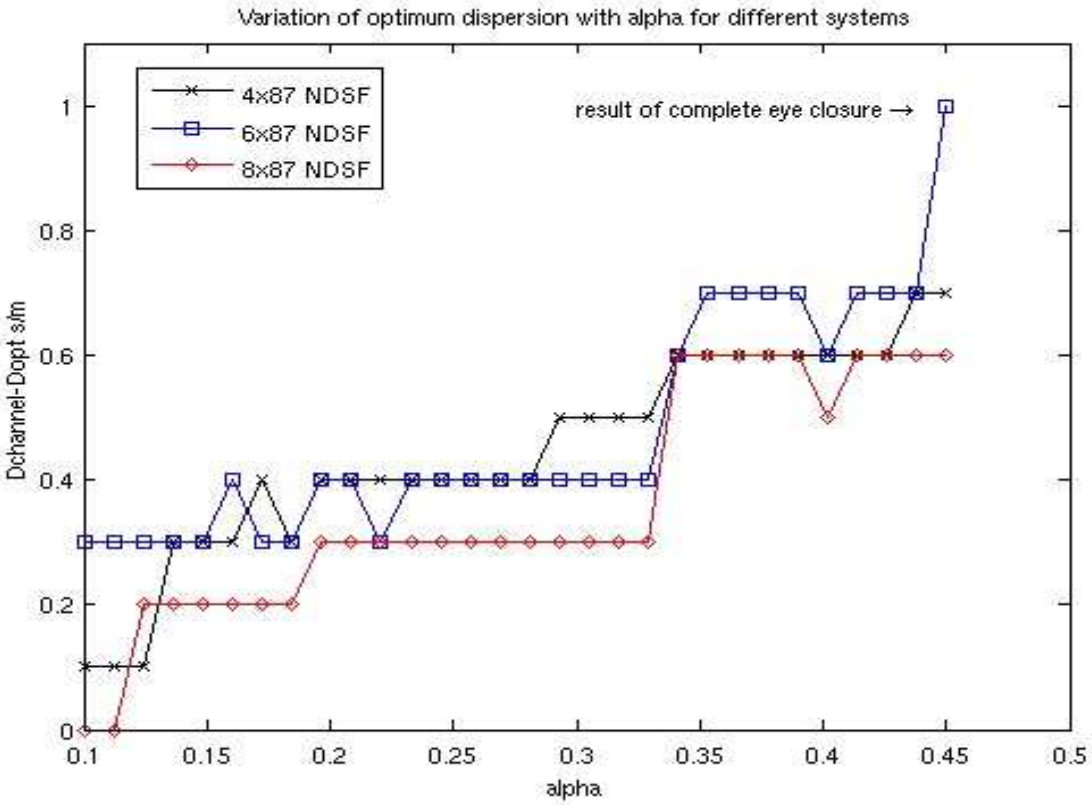

Figure 5.14: The SPM-induced dispersion mismatch versus α_c for eight, six and four 87 km span G.625 system. Again the three curves nearly coincide indicating again that the SPM penalty again depends primarily on α_c in this domain.

Chapter 6

SPM COMPENSATION SENSITIVITY ANALYSIS

6.1 Introduction

In this chapter, a sensitivity analysis is applied to determine the stability of our mathematical model to changes in its input parameters. This model of the multichannel (WDM) communication link, includes all practical uncertainties present in real life fiber links and incorporates link nonuniformities by tracking the optical output power of each amplifier in the link and the length of each fiber span. Monte Carlo sampling is applied to generate different realizations of the model variables that are consistent with their underlying probability density functions. The probability density function of the model output variable is then calculated by evaluating the result of the model for each given realization and arranging these in a histogram.

In our procedure, the power and length of each span fluctuates around mean values P_o and L_o so that the distribution of performances is dependent on the distribution of these values. This represents a departure from the behavior of the uniform model that employs the same parameters P_o and L_o for all links. The output of an experiment in the new model is a probability density function of the ROSNR rather than a single value in the uniform case. Accordingly, we quantify the quality of the compensation by comparing the statistical properties (namely the mean, standard deviation and the performance value

at the 95% cumulative probability of occurrence) of a compensated distribution with an uncompensated one.

Finally, based on an analysis of the new link model, we modify the SPM compensation algorithm that was optimized for uniform ideal links, and optimize it for the new, more realistic model. We also investigate the utility of employing a feedback loop to enhance performance. Conclusions based on a comparison of the different algorithms are finally given.

6.2 Link Model

Any fiber optic link is characterized by the optical launch power, total length and fiber type. The actual value of each parameter deviates from the design value for practical reasons so that in WDM communication systems, the launch power is non-uniform, principally as a result of spectral ripple in optical amplifiers, polarization dependent loss (PDL) and the control error of the optical amplifiers. The length of each fiber span can also deviate from the design value depending on the terrain traversed by the communication link, forcing designers to use different spacing between spans. Further, even if the same type of fiber is employed in every span, the fiber parameters fluctuate due to fabrication tolerances.

In this section we model the variations and uncertainties in the optical output power of each amplifier in the link as well as the length of each span while those of other fiber parameters are ignored.

6.2.1 Power Variation Model

Spectral Ripple

If the frequency response of the optical amplifiers were flat, all channels would experience an identical gain. In practice, however, each channel experiences a different gain. For identical amplifiers this gain nonuniformity is repeated at each span. At any given wavelength the channel average power will either constantly increase or decrease with position along the link. The magnitude of this change depends on the difference between the channel gain and loss per span. We model this by assuming that each amplifier site provides a mean

gain (in dB), which equals the loss per span, together with a variable gain δ that can have any channel-dependent value and is between $\pm\Delta$ where Δ is the amplitude of the ripple of the optical amplifier; that is,

$$G_{amp} = L_{span} + \delta \tag{6.1}$$

where L_{span} is the total loss of a span. Thus the gain of each amplifier lies within $L_{span} \pm \Delta$. The optical output power of each amplifier in the link is

$$\begin{aligned} P(1) &= P_{initial} && (6.2)\\ P(2) &= P_{initial} - L_{span} + G_{amp} && (6.3)\\ P(n) &= P_{initial} + n\{-L_{span} + G_{amp}\} && (6.4) \end{aligned}$$

in which $P_{initial}$ is the initial launch power and n is the span index. Therefore

$$P(n) = P_{initial} + (n-1)\delta \tag{6.5}$$

In a typical link, channels that will constantly increase in power ($\delta > 0$) are initially launched with low power and vice versa. This forms the basis of a power equalization which is used commercially to equalize system performance across channels of optical communication links. Here $P_{initial}$ is chosen to minimize the maximum allowable difference between different channels powers, i.e.

$$P_{initial} = P_o - \frac{\delta}{2}(N-1) \tag{6.6}$$

The mean output power of the channels, P_o, is the power design parameter and is set by system designers. This equalization decreases the maximum difference in power from $\Delta \times (n-1)$ to half of this value. Substituting Eq.6.6in Eq.6.5, we have

$$P(n) = P_o + \frac{\delta}{2}(2n - N - 1) \tag{6.7}$$

Fig. 6.1 displays numerical results for the extreme cases of power evolution in the link with and without equalization, where $Po = 3$ dBm for 8 span system with $\delta = \pm 1$. The maximum difference without equalization is 14 dBm, while this value is reduced to 7 dBm with equalization.

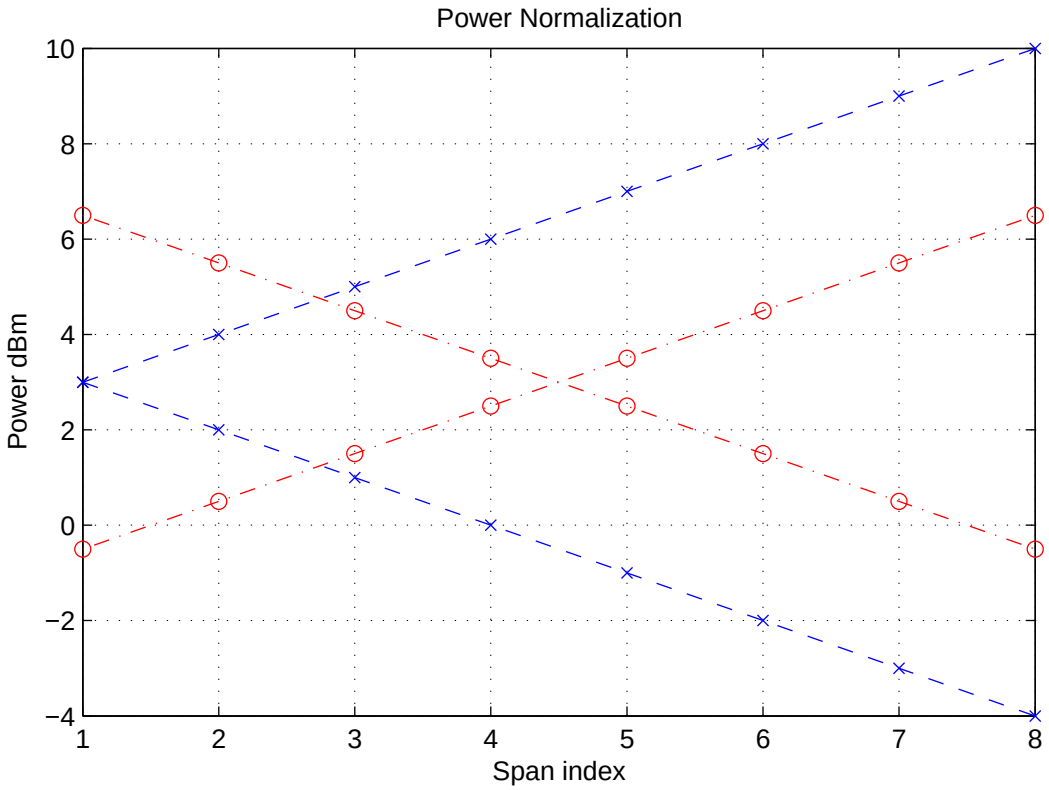

Figure 6.1: Power evolution in an equalized (red circles) and a nonequalized (blue crosses) link.

PDL

Since optical amplifiers should ideally compensate for the overall loss of fiber span, L_{span}. Thus any decrease or increase in the expected loss value will result in extra gain or loss respectively. One such source of power fluctuation is polarization dependent loss (PDL), which introduces an extra source of loss that is dependent on the polarization of each channel. The PDL induced in each span results from the combined effect of several PDL elements (the amplifier and the optical fiber connectors). Each element has a Jones matrix of the following form after diagonalization

$$\begin{pmatrix} 1 & 0 \\ 0 & a \end{pmatrix} \tag{6.8}$$

Here $a(< 1)$ represents the maximum loss and is the PDL magnitude of the element. The combined effect of the PDL elements in each span will depend on the loss of each element, a, and the orientation of each element with respect to the other elements. Thus, the final magnitude, x, of the PDL can, in principal possess any value from zero up to a maximum PDL value corresponding to perfect alignment of the PDL vectors of all elements. The composite Jones matrix of the span is then after diagonalization

$$J^{PDL} = \begin{pmatrix} A & 0 \\ 0 & B \end{pmatrix} \tag{6.9}$$

The PDL magnitude, x, is given by the ratio B/A. Mathematical models have been developed to derive a probability distribution of x. From [13], we find that the distribution in x, in decibels (X) for a large number of concatenated PDL elements follows a Maxwellian distribution. We therefore assume that the PDL in each span, X_n, where n is the span index, follows a Maxwellian distribution, even though the number of PDL elements contributing to it is generally low. The Maxwellian distribution in this case yields a higher probability of occurrence of large X_n values. However since we employ our model in numerical sensitivity analysis in which the output variable must be reevaluated numerous times, the ease of computation of the Maxwellian distribution compared to the exact PDL distribution, is a decisive factor. That the exact distribution overweights large PDL values implies that we slightly overestimate the effect of system fluctuations on SPM compensation so that our results can be treated as an upper bound in this regard.

We also assume that the optical amplifiers are designed to yield equal total output power for all channels, and that the channel count is large. The constant total output power forces the amplifiers to adjust their gain to account for average extra loss in all the channels. But since the channel count is large and the amplifier control circuit is slow, the additional gain g_n^{pdl} equals the average of all loss values.

$$g_n^{pdl} = \langle \frac{A_n^2 + B_n^2}{2} \rangle \tag{6.10}$$

Thus the overall span Jones matrix becomes

$$J_n^{pdl} = \sqrt{g_n^{pdl}} A_n \begin{pmatrix} 1 & 0 \\ 0 & x_n \end{pmatrix} \tag{6.11}$$

From [15], Eq.6.11 yields

$$J_n^{pdl} = \sqrt{10^{\frac{-0.11\mu_{pdl}}{10}} \times \sqrt{\frac{1}{x_n}}} \times \begin{pmatrix} 1 & 0 \\ 0 & x_n \end{pmatrix} \tag{6.12}$$

In the above equation μ_{pdl} is the mean PDL magnitude in each span X_n. The empirical relation relating g_n^{pdl} and A_n to μ_{pdl} was employed to derive Eq.6.12.[15]

The two eigenvalues of this matrix in decibels are

$$\lambda_1 = \frac{X_n}{2} - 0.11 \times \mu_{pdl} \tag{6.13}$$

and

$$\lambda_2 = -\frac{X_n}{2} - 0.11 \times \mu_{pdl} \tag{6.14}$$

Since the signal polarization can be any value between the two states Eq. 6.13 and Eq. 6.14 with equal probability, any extra gain/loss of a channel due to PDL at the n^th span can be represented by a random variable that is distributed uniformly between these two eigenvalues so that

$$G_n^{pdl} = \lambda_1 r_n + \lambda_2 (1 - r_n) = X_n (r_n - 0.5) - 0.11 \times \mu_{pdl} \tag{6.15}$$

with r_n a uniform random variable on $[0, 1]$ This equation is then employed to modify the old power values P^o (Eq. 6.7) (the superscript indicates power values before the PDL

correction), yielding

$$P(1) = P^o(1) + X_1(r_1 - 0.5) - 0.11 \times \mu_{pdl} \quad (6.16)$$

$$P(2) = P^o(2) + X_1(r_1 - 0.5) + X_2(r_2 - 0.5) - 2 \times 0.11 \times \mu_{pdl} \quad (6.17)$$

$$P(n) = P^o(n) - n \times 0.11 \times \mu_{pdl} + \sum_{i=1}^{n} X_i(r_i - 0.5) \quad (6.18)$$

Optical Amplifier Control Error

The output of the amplifier control circuits deviates from their nominal output value as a result of circuit variability. Consequently, the output is best modeled by adding a Gaussian random variable with zero mean and a standard deviation $\sigma_{control}$, to the power value at each site.[20] The average power of any channel that is launched into the n^{th} span, $P(n)$ is then

$$P(n) = P_o + \frac{\delta}{2}(2n - N - 1) - n \times 0.11 \times \mu_{pdl} + \sum_{i=1}^{n} X_i(r_i - 0.5) + \sigma_{control} \times N_n(0,1) \quad (6.19)$$

in which $N_n(0,1)$ denotes a Gaussian random variable with zero mean and unity standard deviation. Evidently, $P(n)$ is a function of the provisioned average power P_o, the amplifier ripple amplitude Δ, the mean PDL per span μ_{pdl} and the standard deviation $\sigma_{control}$ of the control error as well as on a number of Maxwellian (X_n), uniform(δ and r_n), and Gaussian random variables ($N_n(0,1)$).

6.2.2 Span Length

The span length variation can also be modeled as a Gaussian random variable with σ_{length} standard deviation and a mean length per span L_o, which is the span length design parameter, so that so that

$$L(n) = L_o + \sigma_{length} \times N_n(0,1) \quad (6.20)$$

6.3 Sensitivity Analysis

We now employ sensitivity analysis to generate the system performance probability density function. We will compare SPM compensated with uncompensated systems and will compute the sensitivity of the performance to errors in the precompensation parameter. We further investigate if the our analysis of the gain of the SPM compensation in the uniform links is valid for nonuniform links (recall that the gain in the nonuniform links is the increase in the **optimum** launch power that is enabled by SPM compensation). The gain in the uniform case will be found to constitute an upper bound to the gain in the realistic, nonuniform, case. We will accordingly select the optimum uniform link parameters (namely P_o and L_o) to equal the mean of the nonuniform link parameters, and will determine if the same gain is obtained by comparing the probability distributions of the compensated and uncompensated system.

6.3.1 Methodology

The NGM system model inputs (i.e. design parameters) are the provisioned launch power, P_o, the provisioned fiber span length, L_o, the number of spans, N, and the compensation parameters α_c and D_{opt}. Other model parameters are the transmitter and receiver parameters (constant for all the tests and irrelevant to our purpose), the fiber parameters (γ, β_2, and α) and the uncertainty parameters (Δ, μ_{pdl}, $\sigma_{control}$, and σ_L). The model output is defined as the optical signal to noise ratio required to achieve a transmission with a bit error rate of 10^{-3}. We will further use a single fiber type, G.625, in this study. Its parameters are listed in table 6.1. The uncertainty parameters are measured by means of onsite measurements, and are listed in table 6.2.

For $N = 8$ span systems with a provisioned span length of $L_o = 87$ km, we find from Fig. 5.10 that the optimum launch powers for the uncompensated and compensated uniform systems are 0 dBm and 3 dBm, respectively. Thus we employ $P_o = P_o^l = 0$ dBm for the low power uncompensated simulation, and $P_o = P_o^h = 3$ dBm for the high power compensated simulation. We employ a single value for the compensation parameter α_c for all realizations and all channels. We therefore term this quantity the global compensation

parameter α_c^g and propose the following definition

$$\alpha_c^g = \gamma \times N \times P_o \times L_{oeff} \tag{6.21}$$

with

$$L_{oeff} = \frac{1 - \exp\{-\alpha L_o\}}{\alpha} \tag{6.22}$$

By varying α_c^g around this nominal value we will test the sensitivity of the performance to computational error.

In our first test, we vary the optical output power of each optical amplifier in the link, $P(n)$, and the length of each fiber span, $L(n)$ according to the model in Eqs. 6.19 and 6.20, which yield a N element array of power and lengths, $\vec{P}$ and $\vec{L}$, for each realization. For M realizations we therefore create a $M \times N$ matrix of power and length values. A 1024 bit array is then created and employed as the transmitter input. From the transmitter model parameters together with α_c^g, we compute the electric field output of the transmitter E_{Tx}. This signal is propagated M times, where $M = 1000$ in this thesis, through the link defined by the fiber parameter values and the power and length matrices. Subsequently, this signal is processed by the receiver model with the assumed receiver parameters. By also comparing the response of the receiver to the original bit pattern, we determine the optical signal to noise ratio required for 10^{-3} bit error rate detection. For every realization of the link a different ROSNR is obtained and recorded. The simulation thus generates M values for the ROSNR. These values yield the ROSNR probability density function once they are arranged in bins and the normalized number of occurrences in each bin is computed. Note that if $\vec{P}$ and $\vec{L}$ are substituted in Eq. 5.27 the result does not necessarily equal α_c^g. This mismatch together with the nonuniformity of the link, unlike the uniform link employed in numerical back propagation yields the observed residual SPM penalty.

If we restrict our realizations of $\vec{P}$ and $\vec{L}$ to those that yield the same value of α_c^g, such that

$$\gamma \times N \times P_o \times L_{oeff} = \gamma \times \sum_{i=1}^{N} P(i) \times L_{eff}(i) \tag{6.23}$$

in the sensitivity analysis, the measured residual penalty arises solely from the nonuniformity error alone, which we term the nonuniformity test.

The sensitivity analysis procedure can be summarized as follows:

Parameter	NGM system value	Unit
β_2	-2.1	ps^2km^{-1}
γ	1.2×10^{-3}	$m^{-1}W^{-1}$
α	.2	dB/km

Table 6.1: The G.625 fiber parameters.

Parameter	NGM system value	Unit
Δ	0.8	dB
μ_{pdl}	0.36	dB
$\sigma_{control}$	0.16	dB
σ_L	10	km

Table 6.2: The values of the constants in the current application space.

1. Select the values of P_o, L_o, N and the fiber type.
2. Select the desired number of realizations M.
3. Employ the design parameters P_o, L_o, and N along with uncertainty parameters to create the $M \times N$ matrices $P(n)$ and $L(n)$.
4. Select a value for α_c^g.
5. For nonuniformity test, insure that the condition 6.23 applies.
6. Apply a test bit pattern to the transmitter model and create E_{Tx}
7. Employing the power and length matrices and the fiber parameters, propagate E_{Tx} in the fiber link.
8. Employ the receiver model to calculate the ROSNR of each link realization.
9. Employ the M values of ROSNR to compute its probability density function.

6.3.2 Sensitivity Analysis Results

Following the methodology of section 6.3.1, we now compute the probability density functions of the compensated and uncompensated systems. The results are displayed in Fig. 6.2.

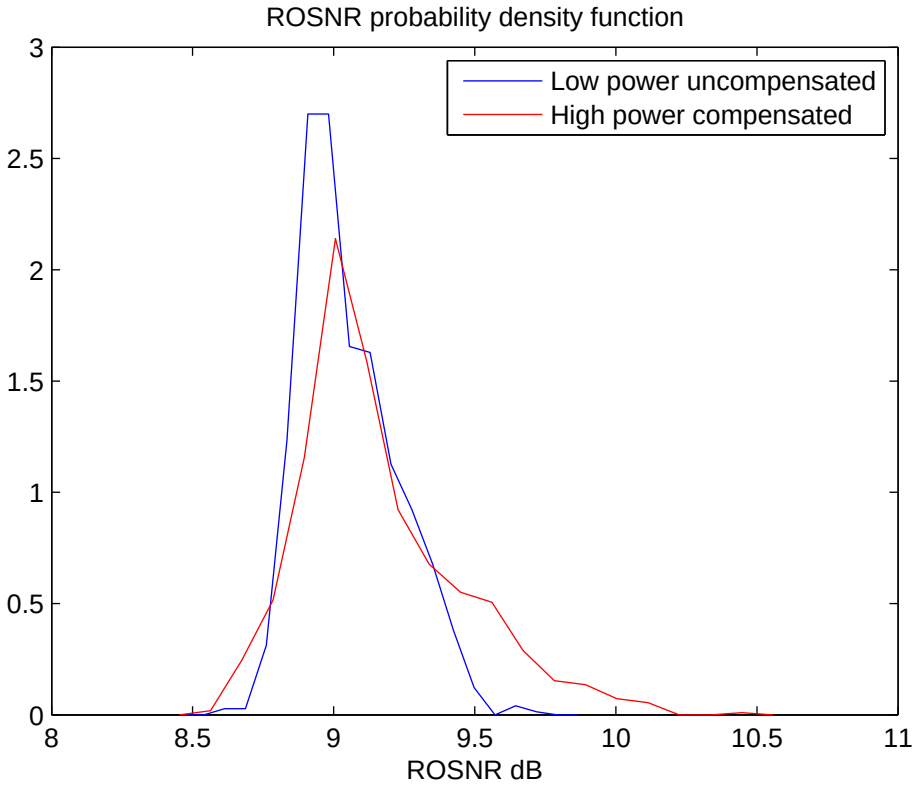

Figure 6.2: The probability density function (in units of dB^{-1}) of the ROSNR in the absence and presence of compensation.

Evidently the residual SPM penalty contributes to the tail of the compensated distribution. The tail of the performance corresponds to the high penalty region, so that a rapidly decaying probability density function at this region is a primary objective in communication system design. We must therefore modify the algorithm to ensure that the tails

	Mean	Mean Sensitivity	Standard deviation	Standard deviation Sensitivity	95% ROSNR	95% ROSNR Sensitivity
Old Compensation	9.2 dB	0.03 dB	0.3 dB	0.02 dB	9.7 dB	0.06 dB
No Compensation	9.0 dB	—	0.2 dB	—	9.4 dB	—
Uniform	9.0 dB	—	0 dB	—	9.0 dB	—

Table 6.3: The statistical properties of compensated, uncompensated and uniform distributions for a 8 span system.

of the compensated and uncompensated distributions nearly coincide. That is, although the statistical properties of the compensated and uncompensated distribution are nearly identical (refer as well to table 6.3), the slow decay of the compensated distribution with the ROSNR is undesired.

We repeated our sensitivity analysis for different α_c^g equal to $0.7\alpha_c^g$, $0.8\alpha_c^g$, $0.9\alpha_c^g$, α_c^g, and $1.1\alpha_c^g$. The mean and 95% ROSNR value are displayed in Fig. 6.3 as a function of α_c^g together with the standard deviation, labeled by the y-axis at the right end of the figure. The x-axis at the top of the figure shows the α_c^g value as a percentage of α_c^g.

From this figure we can determine the sensitivity of the performance to the choice of α_c^g. Applying a second order fit to all the curves and defining the sensitivity of the performance measure as the change in the performance value for a 10% change in the value of α_c^g, we obtain the results of table 6.3, which demonstrate that the algorithm is nearly insensitive to changes in the value of α_c^g.

6.3.3 Modified Compensation Algorithm

We now examine the decay in the residual SPM penalty for the compensated distribution in Fig. 6.2. Since we established that our results are relatively insensitive to α_c^g, the most probable source of error would appear to be the nonuniformity of realistic links. To verify

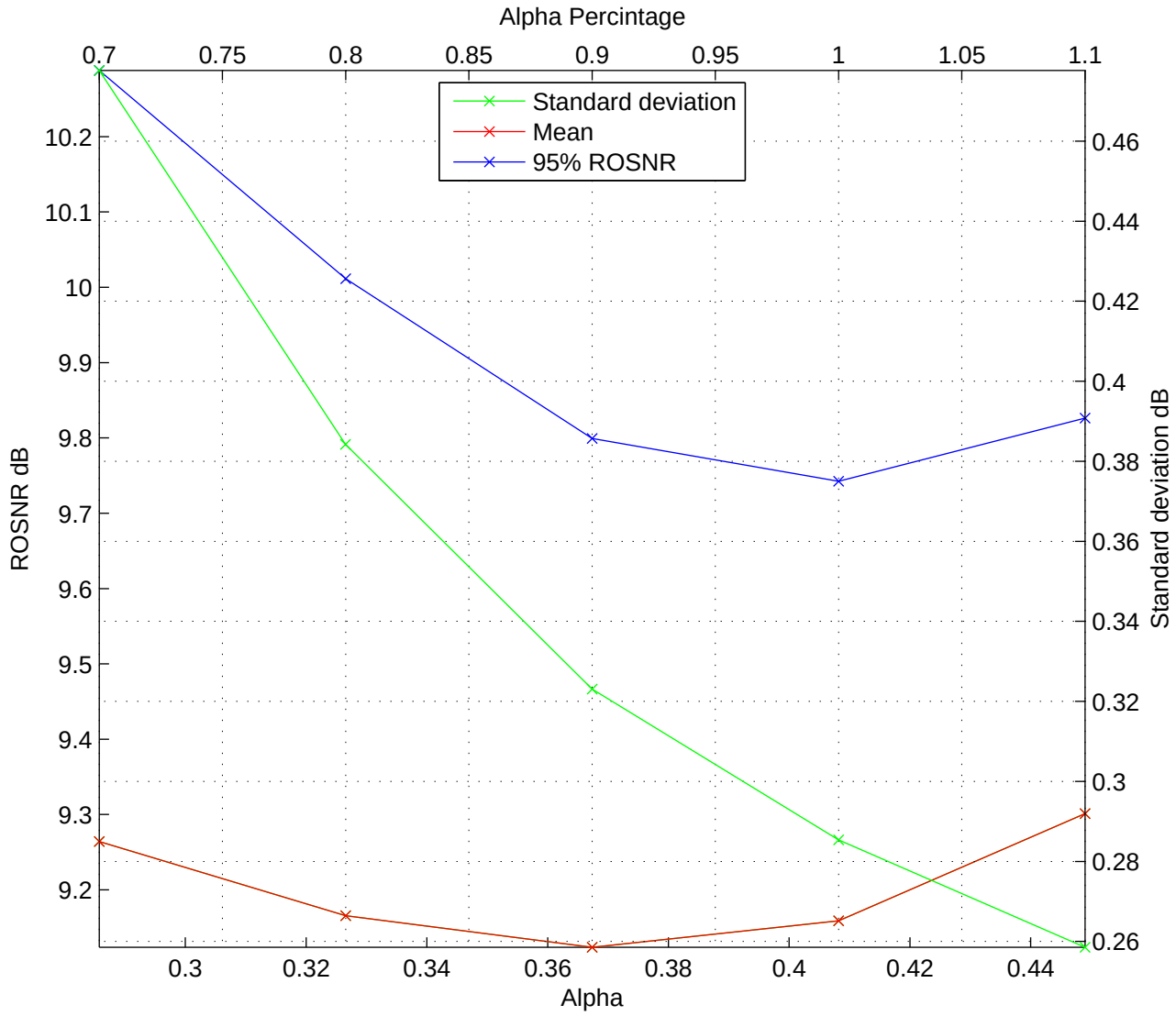

Figure 6.3: The mean, standard deviation and the 95% ROSNR value of the probability density function of the ROSNR versus the global optimization parameter

this, we rerun the sensitivity analysis while enforcing the condition 6.23, which removes the mismatch error. The resulting probability density function of the performance is presented shown in Fig. 6.4.

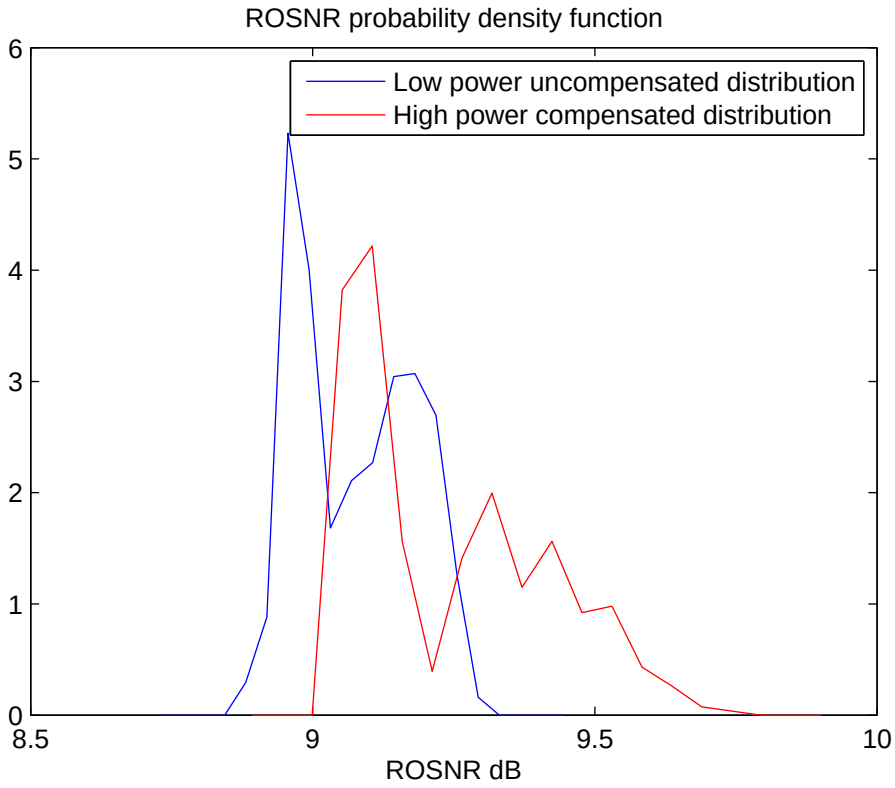

Figure 6.4: Probability density function (in units of dB^{-1}) of the nonuniformity penalty in the presence and absence of compensation

We observe that the distribution has two separated features, a wide peak at high SPM residual penalty associated with channels with a descending power trend ($\delta < 0$) and a further, narrow distribution from channels with an ascending profile ($\delta > 0$). In other words, the SPM penalty increases when the nonlinear phase (the chirp) experiences more dispersion, so that if the launch power is higher in the earlier spans, the resulting nonlinear phase is more dispersed than in the case that the high power occurs towards the end of

	Mean	Standard deviation	95% ROSNR
Old Compensation	9.24 dB	0.17 dB	9.65 dB
Modified Compensation	9.32 dB	0.04 dB	9.42 dB

Table 6.4: Statistical properties of old and modified compensation nonuniformity analysis results.

the link, creating a higher penalty.

That the penalty of the descending channels is higher than the penalty of the other channels suggests that the global remedy applied to all the channels should be adjusted slightly to better compensate the higher penalty channels in order to enhance the overall performance. Thus instead in place of an uniform link we modify the numerical back propagation process to better compensate the descending power profile. For 2 step compensation we therefore divide α_c into two segments with relative magnitudes x_r and $1-x_r$ and divide D_{opt} similarly into the two segments with relative lengths $1-x_r$ and x_r respectively with $x_r = 0.4$ in place of $x_r \neq 0.5$. This is an empirical choice as the optimum value depends in general on the uncertainty parameters. We then repeat the previous calculation and plot the probability density function of both uncompensated and compensated cases in Fig. 6.5.

Here we find that the two features in Fig. 6.4 approach each other to form a single peak as shown in Fig. 6.5. Even if the overall mean is slightly higher than the uncompensated case, the narrowness of the distribution indicates a significantly reduced penalty associated with the link nonuniformity, c.f. table 6.4.

6.3.4 Modified Compensation Sensitivity Analysis

After reducing the effect of link nonuniformity through the parameter x_r we repeat our sensitivity analysis with the modified algorithm. This yields the probability density functions for the compensated and uncompensated distributions shown in Fig. 6.6.

The statistical properties of the original and the modified algorithms distributions are

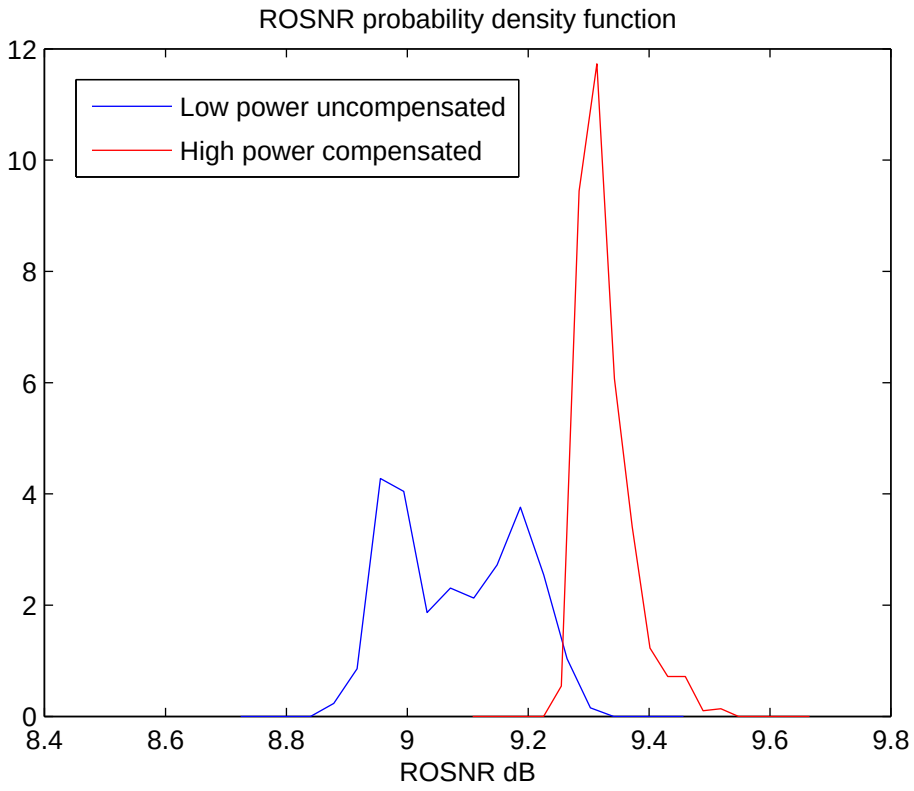

Figure 6.5: The probability density function (in units of dB^{-1}) for a nonuniform penalty and the modified SPM compensation algorithm in both the presence and absence of compensation

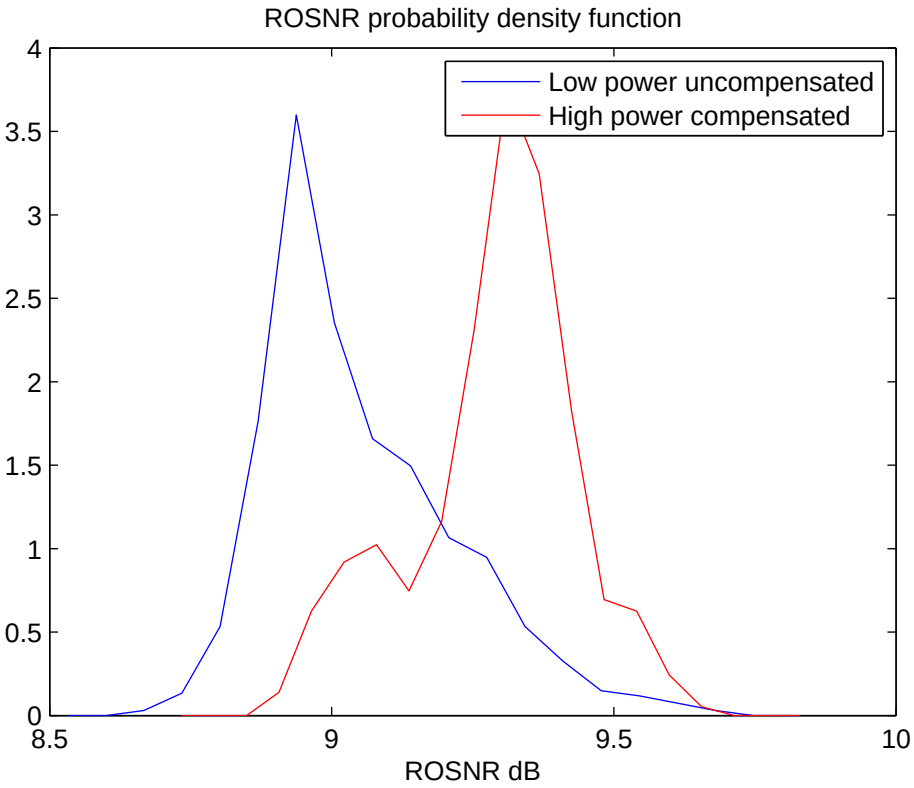

Figure 6.6: The probability density functions (in units of dB^{-1}) of the ROSNR for uncompensated system and a system compensated according to our modified algorithm

	Mean	Mean Sensitivity	Standard deviation	Standard deviation Sensitivity	95% ROSNR	95% ROSNR Sensitivity
Old Compensation	9.2 dB	0.03 dB	0.3 dB	0.02 dB	9.7 dB	0.06 dB
Modified Compensation	9.3 dB	0.04 dB	0.1 dB	0.02 dB	9.5 dB	0.08 dB

Table 6.5: The variation of the statistical properties with α_c^g, for both the unmodified and modified compensation algorithms.

compared in table 6.5. From the 95% ROSNR values and a visual inspection of Fig. 6.6 we observe that the tail of the distribution has been suppressed so that the compensated system decays at a similar rate to the uncompensated system, although at the cost of a slight increase in the mean of the distribution.

We now determine the sensitivity of the new method to the choice of α_c^g by employing values of α_c^g, from 0.7 to 1.1. This yields the values for the mean, standard deviation and 95% ROSNR value of Fig. 6.7.

The sensitivity is slightly degraded in the modified algorithm as shown in table 6.5; however the loss of performance as a result of this effect is slight.

6.3.5 Optimized Modified Compensation

Closed loop control is a standard method for optimizing communication network performance that is employed in the context of NGM to optimize the parameter D_{opt}. We could accordingly optimize α_c by different feedback-determined α_c value for each channel instead of a single global value. Since we have previously noted that the performance is relatively insensitive to α_c^g, however we expect that the dependence on such a feedback parameter would be small.

In this section we therefore examine an alternative method for channel optimization. We will optimize x_r for each channel in place of applying one global ratio to all the channels. In particular, we employ $x_r = .4$ for descending channels and $x_r = .5$ for ascending ones.

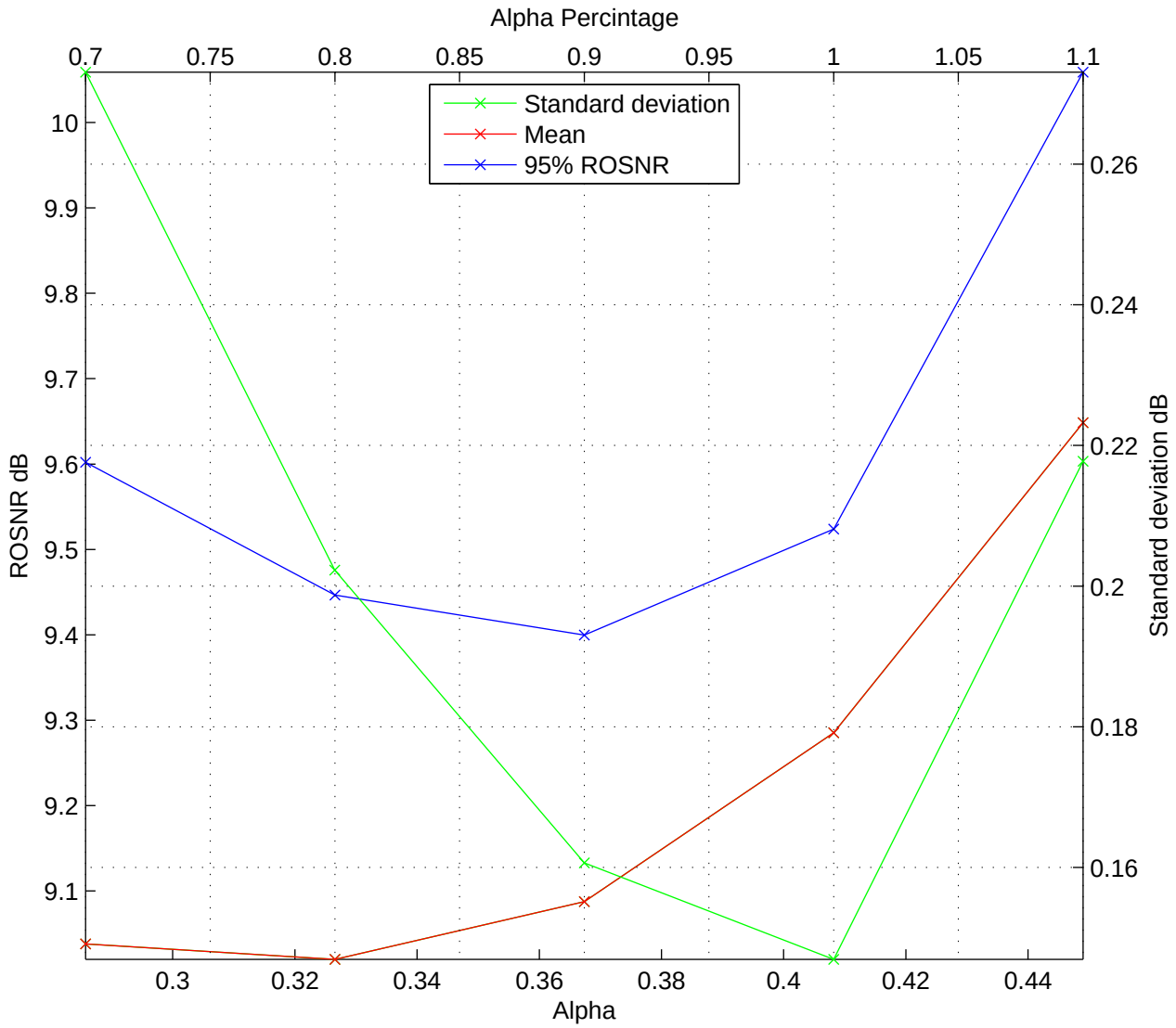

Figure 6.7: The mean, standard deviation and 95% ROSNR value of the probability density function as a function of the global optimization parameter for the modified compensation method

The quantity x_r can be more easily optimized than α_c as it has only two values and can even be provisioned.

Applying our sensitivity analysis to the optimized modified compensation algorithm we obtain the results of Fig. 6.8

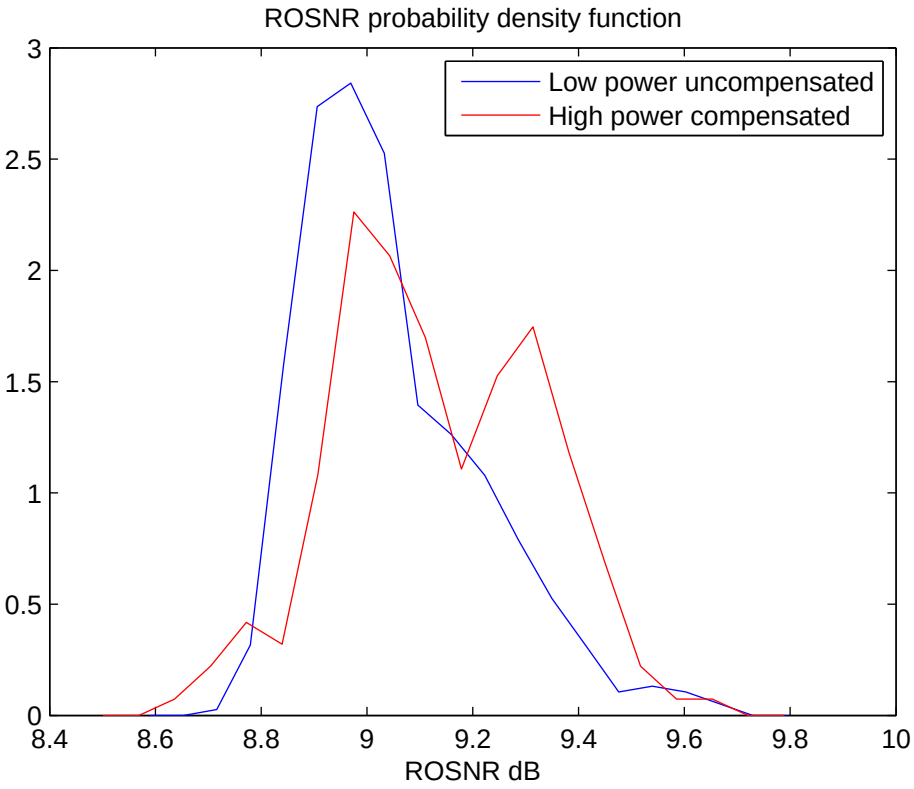

Figure 6.8: Probability density function (in units of dB^{-1}) of ROSNR for both an uncompensated system and a system compensated with optimized x_r values, displayed with a linear scale

Graphed in a logarithmic scale, c.f. Fig. 6.9 we observe that the tails of the probability distribution functions of the uncompensated and x_r compensated distributions are nearly identical.

The statistical properties of the compensated distribution are listed in table 6.6 together

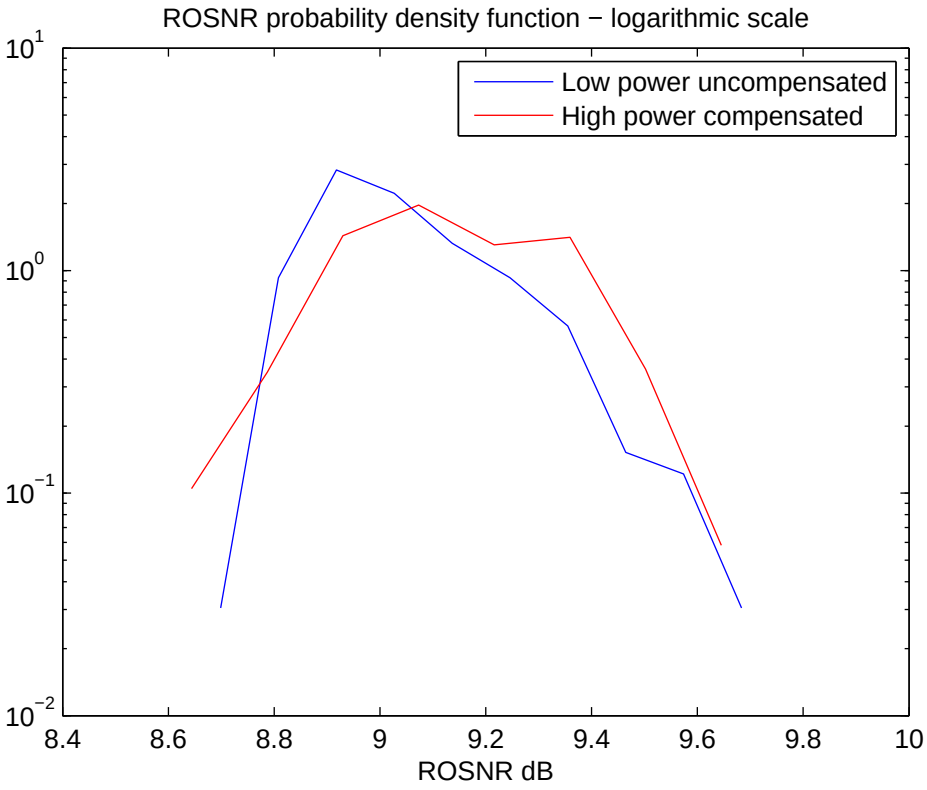

Figure 6.9: As in the previous figure but with a logarithmic scale

	Mean	Mean Sensitivity	Standard deviation	Standard deviation Sensitivity	95% ROSNR	95% ROSNR Sensitivity
Old Compensation	9.2 dB	0.03 dB	0.3 dB	0.02 dB	9.7 dB	0.06 dB
Modified Compensation	9.3 dB	0.04 dB	0.1 dB	0.02 dB	9.5 dB	0.08 dB
Optimized x_r	9.1 dB	0.03 dB	0.2 dB	0.01 dB	9.4 dB	0.05 dB
No Compensation	9.0 dB	—	0.2 dB	—	9.4 dB	—
Uniform	9.0 dB	—	0 dB	—	9.0 dB	—

Table 6.6: A summary of SPM compensation performance for a 8 span system.

with the results of the other compensation algorithms and of the uncompensated case. Evidently the statistical properties of the optimized modified algorithm agree to within $< \pm 0.1$dB to those of the uncompensated distribution. Further, we observe from Fig. 6.10 and table 6.6 that the method is insensitive to the value of α_c^g. Accordingly, a closed loop is not necessary for SPM compensation.

6.4 4 Span Systems

The power and length variability of short-haul systems is less problematic than in their long haul counterparts. While our first compensation algorithm yields a performance very similar to the uncompensated case, we will associate $P_o^l = 3$ dBm $P_o^h = 6$ dBm with "optimum" launch powers proceeding from Fig. 5.12. The resulting performance is displayed in Figs. 6.11 and 6.12.

Clearly, the figures and the table 6.7 indicate that the two curves possess nearly identical statistical properties. Additionally, Fig. 6.13 displays the mean, standard deviation and the 95% ROSNR value of the probability density function as a function of α_c^g. Again, the performance measures vary very slowly with α_c^g indicating that our initial, simple

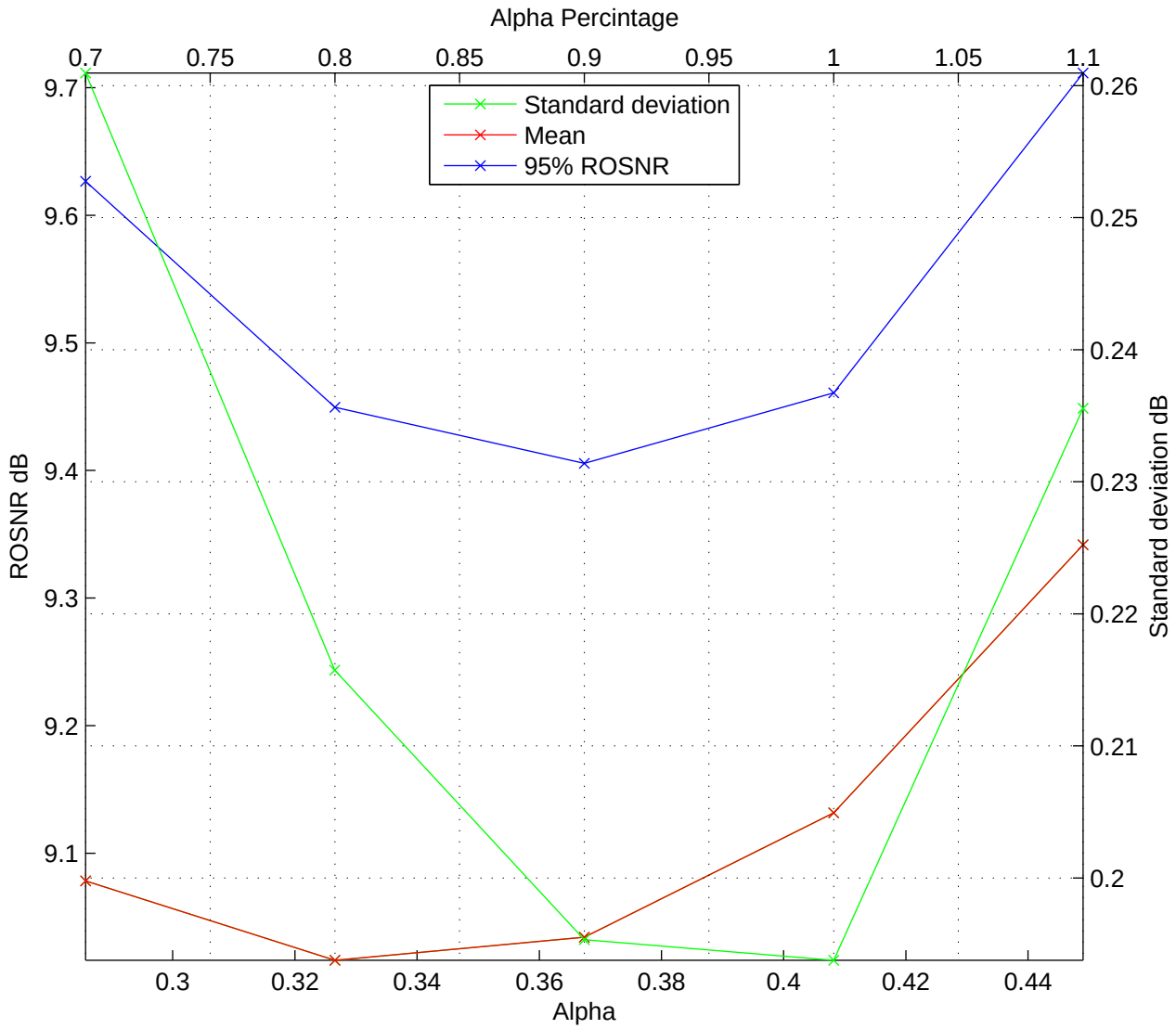

Figure 6.10: The mean, standard deviation and 95% ROSNR value of the probability density function of ROSNR versus the value of the global optimization parameter for optimized x_r compensation.

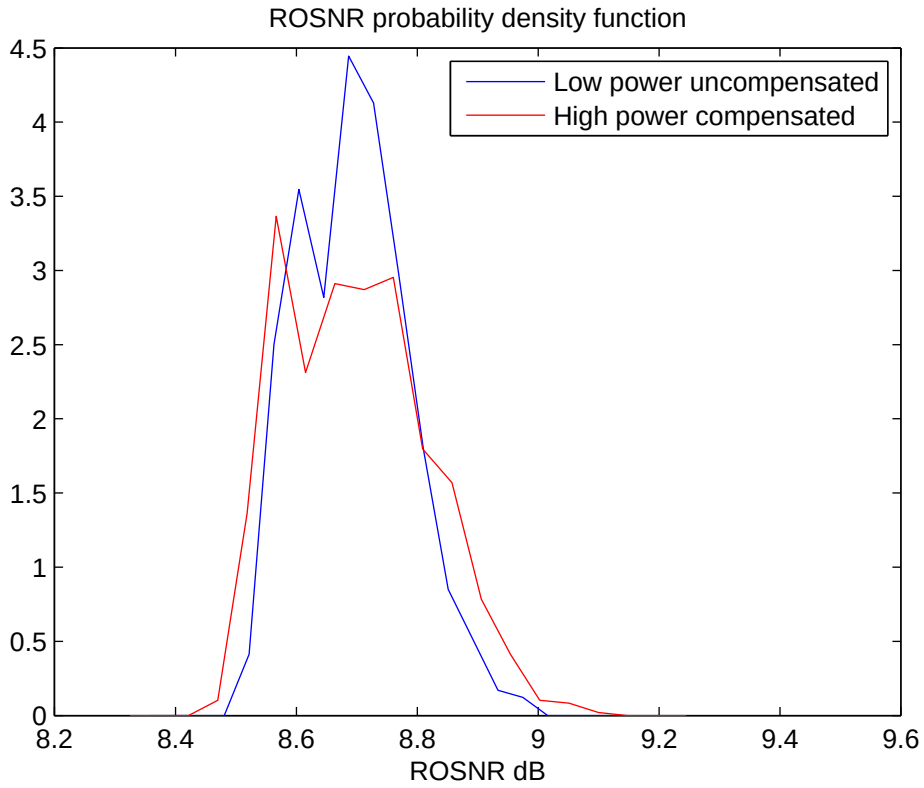

Figure 6.11: The probability density function (in units of dB^{-1}) of the ROSNR in both the absence and presence of compensation for a 4 span system in linear scale.

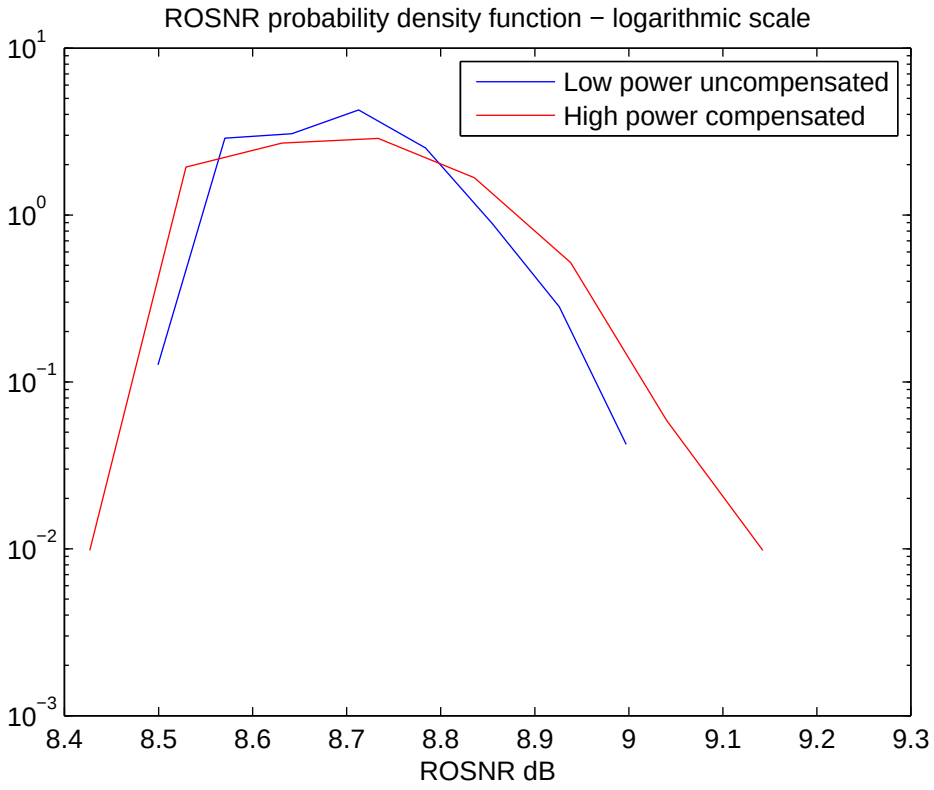

Figure 6.12: As in the previous figure but plotted on a logarithmic scale.

compensation algorithm is sufficient for short haul systems.

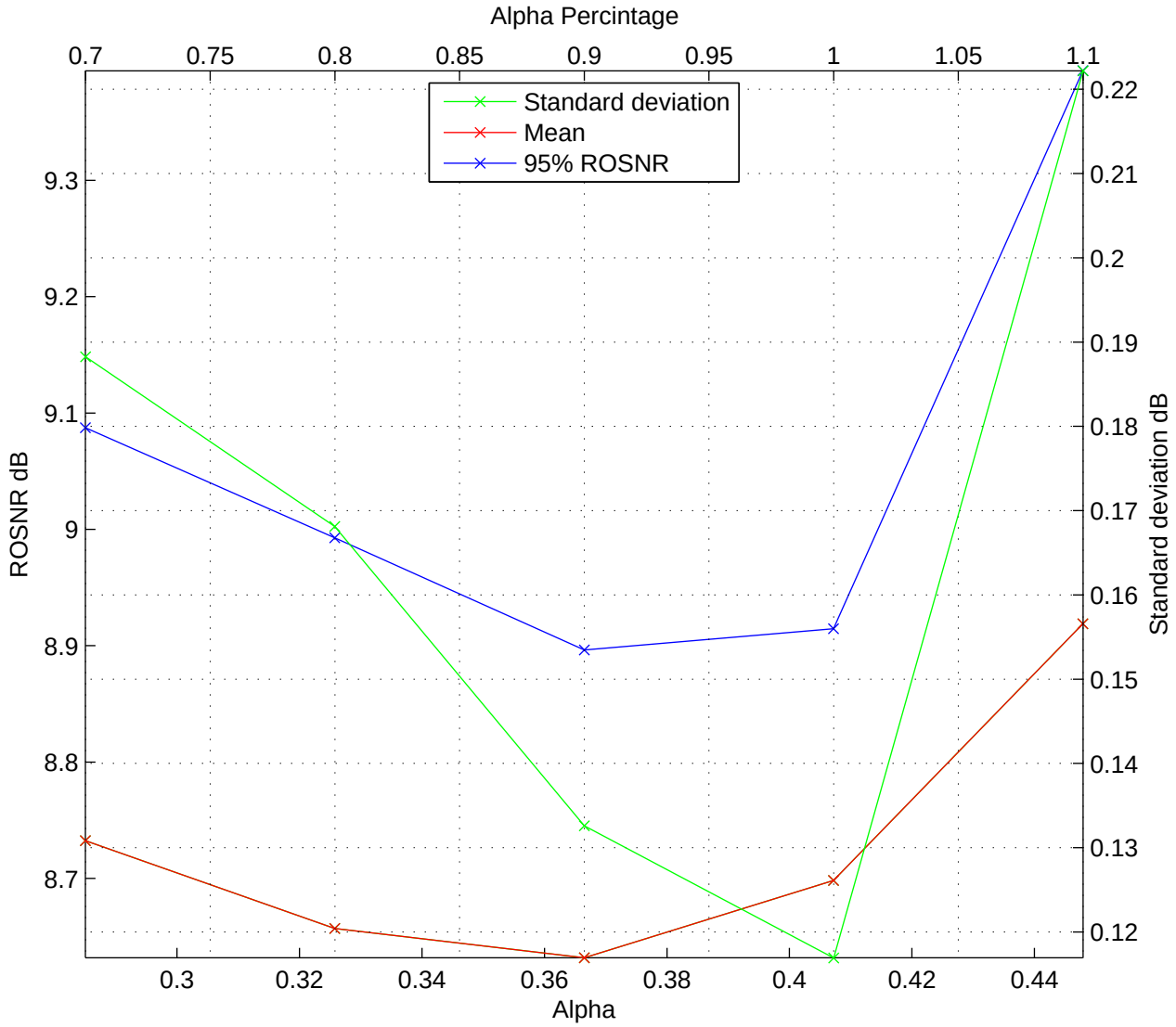

Figure 6.13: The mean, standard deviation and the 95% ROSNR value of probability density function of ROSNR versus the global optimization parameter

	Mean	Mean Sensitivity	Standard deviation	Standard deviation Sensitivity	95% ROSNR	95% ROSNR Sensitivity
Old Compensation	8.7 dB	0.04 dB	0.1 dB	0.02 dB	8.9 dB	0.07 dB
No Compensation	8.7 dB	—	0.1 dB	—	8.9 dB	—
Uniform	8.7 dB	—	0 dB	—	8.7 dB	—

Table 6.7: A summary of SPM compensation performance for a 4 span system.

6.5 Conclusions

We have developed methods for SPM compensation that yield a 3 dBm increase in launch power for 8 and 4 span systems in the presence of realistic power and length variations in the link. A similar gain is recorded for systems with uniform links, indicating that our compensation procedures are stable against power and span length fluctuations. We have also found that the performance varies by $< .1$ dB for a 10% change in the global compensation parameter. Further, the use of feedback to optimize the compensation parameter α_c appears unnecessary since optimizing x_r for each channel only yields an increase in performance that of < 0.1 dB compared to the low power performance. Here the optimization of x_r can be provisioned (unlike α_c and D_{opt}) by assigning to it one of two values depending on whether the channel initial launch power is higher or lower than average launch power.

Appendix A

Pseudo Random Bit Sequence

A Pseudo Random Bit Sequence, PRBS, as the name implies, is a sequence of bits that is close to being a true random sequence. A typical example for an order 9 modulo 2 polynomial is [17]

$$x^9 + x^4 + x^0 \tag{A.1}$$

Here the + operation represents modulo 2 addition and the value of the bit i is the result of applying its 9 preceding bits $(i-1, i-2, .., i-9)$ to the polynomial. In order to obtain the $i+1$ number in the sequence, we shift the input address by a single bit $(i, i-1, .., i-8)$ and recalculate from the polynomial and so on.

Repeating this process starting from any initial set of bits (except the zero bit sequence) yields a sequence of bits that repeats after 2^N-1 bits but contains all possible combinations of N bits. Thus each polynomial of degree N yields a $2^N - 1$ pseudo random bit sequence which contains all possible sequences of N bits in an effectively random order.

In this thesis a maximal length PRBS sequence of order 15 is employed generated from the polynomial

$$x^{15} + x^{14} + x^{13} + x^{11} \tag{A.2}$$

Appendix B

Dual Drive Mach-Zehnder

In this appendix, we derive the relation between nonlinear table output and input. From 4.1,

$$E_{out} = \frac{E_{in}}{2}(e^{j\phi_1} + e^{j\phi_2})$$

in which

$$E_{out}/E_{in} = Ae^{j\theta}$$

and

$$Ae^{j\theta} = \frac{1}{2}(e^{j\phi_1} + e^{j\phi_2}) \tag{B.1}$$

Taking the amplitude of both sides,

$$\begin{aligned} 2A &= \sqrt{(\sin\phi_1 + \sin\phi_2)^2 + (\cos\phi_1 + \cos\phi_2)^2} \\ &= \sqrt{2 + 2(\sin\phi_1 \sin\phi_2 + \cos\phi_1 \cos\phi_2)} \\ &= \sqrt{2(1 + \cos\phi_1 - \phi_2)} \end{aligned}$$

or alternatively

$$\begin{aligned} 2A &= \sqrt{4\cos^2\frac{\phi_1 - \phi_2}{2}} \\ &= 2\cos\frac{\phi_1 - \phi_2}{2} \end{aligned}$$

Thus

$$\phi_1 - \phi_2 = 2\arccos A \tag{B.2}$$

Taking the phase of both sides of B.1 now yields

$$\theta = \arctan \frac{\sin \phi_1 + \sin \phi_2}{\cos \phi_1 + \cos \phi_2}$$

or equivalently

$$\begin{aligned} \theta &= \arctan \frac{2 \sin \frac{\phi_1+\phi_2}{2} \cos \frac{\phi_1-\phi_2}{2}}{2 \cos \frac{\phi_1+\phi_2}{2} \cos \frac{\phi_1-\phi_2}{2}} \\ &= \arctan \tan \frac{\phi_1 + \phi_2}{2} \end{aligned}$$

Since

$$\phi_1 + \phi_2 = 2\theta \tag{B.3}$$

we finally obtain after combining B.2 & B.3

$$\phi_1 = \theta + \arccos A \tag{B.4}$$

$$\phi_2 = \theta - \arccos A \tag{B.5}$$

Appendix C

Back Propagation/Optical Phase Conjugation

Optical phase conjugation, OPC, can be employed to remove distortion resulting from propagation through any medium, as was demonstrated by Yariv for perfect reconstruction of pictorial information propagated through a multimode fiber in [26], and of signals sent through atmosphere layers in [27]. In particular, if a signal is transmitted through a medium and is subsequently phase conjugated and retransmitted through the same media, the signal is restored to its original shape.

Phase conjugation was typically implemented by nonlinear three and four wave mixing together with appropriate filtering.[28] Such a procedure was also found to compensate both dispersion [29] and nonlinear distortion [16], including both dispersion and self-phase modulation.[6] To see this, we represent the scalar electric field $E_F(\mathbf{r}, t)$ as[27]

$$E_F(\mathbf{r}, t) = \Re\{\psi(\mathbf{r}) \exp i(\omega t - kz)\} \tag{C.1}$$

in which the subscript indicates forward propagation.

Placing this into the scalar wave equation

$$\nabla^2 E + \omega^2 \mu\epsilon(\mathbf{r}) E = 0 \tag{C.2}$$

we obtain

$$\nabla^2 \psi + [\omega^2 \mu\epsilon(\mathbf{r}) - k^2]\psi - 2ik\frac{\partial \psi}{\partial z} = 0 \tag{C.3}$$

or, complex conjugating,

$$\nabla^2\psi^* + [\omega^2\mu\epsilon(\mathbf{r}) - k^2]\psi^* + 2ik\frac{\partial\psi^*}{\partial z} = 0 \tag{C.4}$$

which is identical to the wave equation of a back propagating field of the form,

$$E_B(\mathbf{r},t) = \Re\{\psi^*(\mathbf{r})\exp i(\omega t + kz)\} \tag{C.5}$$

A further implication of this result is that the initial signal $\psi(x,y,0)$ that will generate a desired signal at the end of the link given by $\psi(x,y,L)$ can be obtained by complex conjugating the desired signal and employ this as the boundary condition of Eq. C.4. Then, solving this wave equation for the appropriate link parameters yields the desired signal $\psi(x,y,0)$. This process can be performed numerically with DSP techniques instead of physically, as previously suggested, which avoids the obvious problems associated with conjugating the signal.

If losses are present, the propagation constant, k, is complex and the above derivation fails. As a result, the OPC procedure becomes less accurate. However, this limitation can be removed by back propagation. This corresponds to OPC in which however attenuation during propagation is replaced by amplification. Thus for forward propagation we obtain from 2.64

$$A(z+h,T) = \exp(-\frac{\alpha h}{2})F^{-1}\{\exp\{\frac{i}{2}h\beta_2\omega^2\}F\{\exp(ih\gamma|A(z,T)|^2)A(z,T)\}\} \tag{C.6}$$

which is can be inverted to

$$A(z,T) = \exp(-ih\gamma|\tilde{A}(z+h,T)|^2)\tilde{A}(z+h,T) \tag{C.7}$$

with

$$\tilde{A}(z+h,T) = F^{-1}\{\exp\{\frac{-i}{2}h\beta_2\omega^2\}F\{\exp(\frac{\alpha h}{2})A(z+h,T)\}\} \tag{C.8}$$

That is, we again start with $A(0,T)$ and employ C.6 to determine the envelop after a certain length, $A(L,T)$. We then proceed to apply C.6 to this value to recover $A(0,T)$. Accordingly back propagation is time reversed propagation employing the negative of the parameters α, β_2, and γ. In this manner, we recover $A(0,T)$, which is the desired signal multiplied by the inverse response of the link.

Appendix D

Parameter Reduction

D.1 Single Parameter Approximation

To derive the α_c approximation in which the parameter set of the fiber is replaced by a single parameter, we first rewrite Eq. 2.53 as

$$A(z,T) = \exp\{\int_0^z (\hat{D}(T) + \hat{N}(\zeta,T))d\zeta\} \times A(0,T) \tag{D.1}$$

Further, for back propagation in the absence of loss

$$\hat{D}(T) = \frac{i}{2}\beta_2\frac{\partial^2}{\partial T^2} \tag{D.2}$$

$$\hat{N}(z,T) = -i\gamma|A(z,T)|^2 \tag{D.3}$$

constitutes the formal solution of the wave equation. If the exponent is approximated by a symmetrical product of individual exponents as suggested by the second-order BCH formula. That is,

$$A(z,T) = \exp\{\hat{D}(T)\frac{z}{2}\}\{\exp\{\int_0^z \hat{N}(\zeta,T)d\zeta\}\{\exp\{\hat{D}(T)\frac{z}{2}\}A(0,T)\}\} \tag{D.4}$$

We will now approximate the integral in the second operator by noting that the SPM penalty, is far smaller than the dispersion, c.f. chapter 5. Assuming as well that the pulse

envelope evolves linearly with propagation distance and incorporating the parameters for our G.625 non dispersion-managed fiber, we find that a 3 point trapezoidal formula is sufficiently accurate for our further results.[17] The integration is performed over the whole link in which we have ignored losses and replaced each span with its effective length, L_{eff}, instead of its total length, so that the total effective fiber length is NL_{eff}, i.e.

$$\int_0^z \hat{N}(\zeta,T)d\zeta = -i\gamma \int_0^z |A(\zeta,T)|^2 d\zeta \tag{D.5}$$

$$\int_0^z \hat{N}(\zeta,T)d\zeta = -i\gamma(\frac{NL_{eff}}{4})(|A(0,T)|^2 + 2|A(\frac{z}{2},T)|^2 + |A(z,T)|^2) \tag{D.6}$$

Normalizing the envelope yields Eq. 5.33 with

$$\alpha_c = \gamma \times N \times P \times L_{eff} \tag{D.7}$$

or for a general link,

$$\alpha_c = \gamma \times \sum_{i=1}^{N} P(i) \times L_{eff}(i) \tag{D.8}$$

That is, in our present method, we approximate the influence of both loss and dispersion instead of solely loss on the field appearing in the integral expression in the central operator. This will lead to a large increase in computational accuracy per step. That only three operators are required in our subsequent computations can be understood from the fact that below a somewhat smaller launch power, only one operator is required since dispersion dominates.

D.2 Error Quantification

We now quantify the error associated with linearizing the nonlinear integral. We expand the integral in Eq. D.4 in a Taylor series,

$$\begin{aligned} A_{NL}(z,T) &= \exp\{\hat{D}(T)\frac{z}{2}\}\{(1 - i\gamma \int_0^z |A(\zeta,T)|^2 d\zeta + ...)\{\exp\{\hat{D}(T)\frac{z}{2}\}A(0,T)\}\} \\ A_{NL}(z,T) &\approx (1 - i\gamma \int_0^z |A(\zeta,T)|^2 d\zeta + ...)\{\exp\{\hat{D}(T)z\}A(0,T)\} \\ A_{NL}(z,T) &= A_L(z,T) - \{i\gamma \int_0^z |A(\zeta,T)|^2 d\zeta\}A_L(z,T) + ... \end{aligned} \tag{D.9}$$

Since the second term is associated with the leading error, we will examine its squared magnitude relative to that of the of signal (note that the power of the linear and nonlinear signals are identical).

$$P_e = \frac{1}{T}\int |\{i\gamma \int_0^z |A(\zeta,T)|^2 d\zeta\}|^2 |A_L(z,T)|^2 dT \tag{D.10}$$

or equivalently

$$P_e = \gamma^2 \frac{1}{T}\int \{\int_0^z |A(\zeta_1,T)|^2 d\zeta_1\}\{\int_0^z |A(\zeta_2,T)|^2 d\zeta_2\}|A_L(z,T)|^2 dT \tag{D.11}$$

After interchanging the order of integration, and applying the following inequality, which we have found to be true in numerous simulations,

$$\begin{aligned}\frac{1}{T}\int \|A(\zeta_1,T)|^2 |A(\zeta_2,T)|^2 |A_L(z,T)|^2 dT \;\; < \;\; & \{\frac{1}{T}\int \|A(\zeta_1,T)|^2 dT\}\{\frac{1}{T}\int \|A(\zeta_2,T)|^2 dT\} \\ & \{\frac{1}{T}\int \|A_L(z,T)|^2 dT\}\end{aligned}$$

where the right hand side is identical to P^3. This yields, with $z = NL_{eff}$,

$$P_e < \gamma^2 \int_0^z \int_0^z P^3 d\zeta_1 d\zeta_2 = \gamma^2 N^2 L_{eff}^2 P^3 \tag{D.12}$$

or

$$Pe/P < \alpha_c^2 \tag{D.13}$$

Thus, the error is second order in α_c. For the moderate system powers of interest to this thesis, we have $\alpha_c < 0.5$, insuring the applicability of this method. The the error can of course be further reduced by employing an increased number of steps. Further, the error arising from the third error commutator neglected in this appendix is far smaller. Accordingly, we will employ the result of this appendix as an upper bound for the expected system performance. Results for this upper bound for a 8 span system and a single-step algorithm are compared to the analytic upper bound in Fig. D.1.

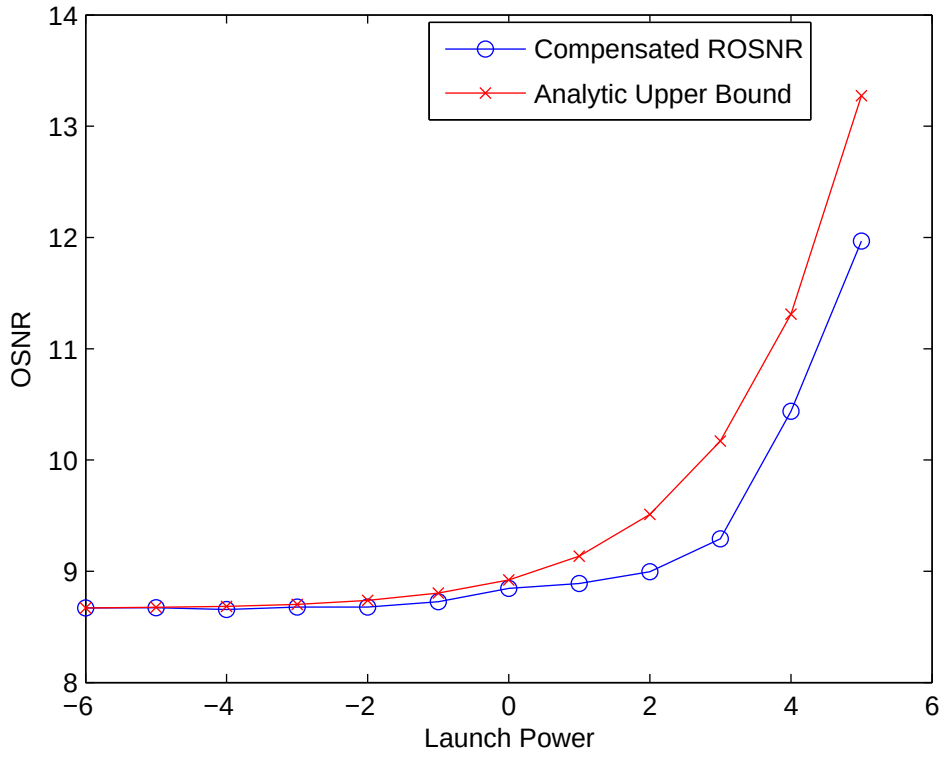

Figure D.1: Analytic upper bound compared to the results of the approximate three-operator theory

Bibliography

[1] Govind P. Agrawal. *Nonlinear Fiber Optics*. Academic Press, 1989.

[2] Govind P. Agrawal. *The Supercontinuum Laser Source*, chapter 3. Springer, 1989.

[3] Govind P. Agrawal. *Fiber-Optic Communication Systems*. John Wiley, 1997.

[4] Partha P. Banerjee. *Nonlinear Optics*. Marcel Dekker, 2004.

[5] Erik Eriksen. Properties of higher-order commutator products and the baker-hausdorff formula. *Journal of Mathematical Physics*, 9(5), May 1968.

[6] Robert A. Fisher, B. R. Suydam, and D. Yevick. Optical phase conjugation for time-domain undoing of dispersive self-phase-modulation effects. *Optics Letters*, 8(12), December 1983.

[7] J. A. Fleck, J. R. Morris, and M. D. Feit. Time-dependent propagation of high energy laser beams through the atmosphere. *Applied Physics*, 10(2), June 1976.

[8] T. K. Gustafson, J. P. Taran, H. A. Haus, J. R. Lifsitz, and P. L. Kelley. Self-modulation, self-steeping, and spectral development of light in small-scale trapped filaments. *Phys. Rev.*, 177(1), 1969.

[9] John David Jackson. *Classical Electrodynamics*. John Wiley, 1998.

[10] Yuji Kodama and Akira Hasegawa. Nonlinear pulse propagation in a monomode dielectric guide. *IEEE Journal of Quantum Electronics*, 23(5), 1987.

[11] S.G. Lipson, H. Lipson, and D.S. Tannhauser. *Optical Physics*. Cambridge, 1996.

[12] Doug McGhan, Charles Laperle, Alexander Savchenko, Chuandong Li, Gary Mak, and Maurice O'sullivan. 5120-km rz-dpsk transmission over g.652 fiber at 10 gb/s without optical dispersion compensation. *IEEE Photonic Technology Letters*, 18(2), January 2006.

[13] Antonio Mecozzi and Mark Shtaif. The statistics of polarization-dependent loss in optical communication systems. *IEEE Photonic Technology Letters*, 14(3), March 2002.

[14] Philip M. Morse and Herman Feshbach. *Methods of Theoretical Physics*. McGraw-Hill, 1953.

[15] Maurice O'sullivan. Pdl penalty prescription. Technical report, Nortle Networks, 2003.

[16] David M. Pepper and Amon Yariv. Compensation for phase distortions in nonlinear media by phase conjugation. *Optics Letters*, 5(2), February 1980.

[17] William H. Press, Brian P. Flannery, Saul A. Teukolsky, and William T. Vetterling. *Numerical Recipes in Pascal*. Cambridge, 1989.

[18] John G. Proakis. *Digital Communications*. McGraw-Hill, 2001.

[19] Rajiv Ramaswami and Kumar N. Sivarajan. *Opticla Networks, A Practical Perspective*. Morgan Kaufmann, 2002.

[20] K. F. Riley, M. P. Hobson, and Bence S. J. *Mathematical Methods*. Cambridge, 1998.

[21] Y. R. Shen. *The Principles of Nonlinear Optics*. John Wiley, 1984.

[22] Joseph T. Verdeyen. *Laser Electronics*. Prentice Hall, 1995.

[23] Sheldon Walklin and Jan Conradi. Effect of machzehnder modulator dc extinction ratio on residual chirp-induced dispersion in 10-gb/s binary and am-psk duobinary lightwave systems. *IEEE Photonics Technology Letters*, 9(10), October 1997.

[24] Kuang-Tsan Wu. Modulation formats for next-generation modulator. Technical report, Nortel Networks, 2003.

[25] Kuang-Tsan Wu. Investigation of spm compensation using warp. Technical report, Nortel Networks, 2006.

[26] Amon Yariv. Three-dimensional pictorial transmission in optical fibers. *Applied Physics Letters*, 28(2), January 1976.

[27] Amon Yariv. Compensation for atmospheric degradation of optical beam transmission by nonlinear optical mixing. *Optics Communications*, 21(1), April 1977.

[28] Amon Yariv. Phase conjugate optics and real-time holography. *IEEE Journal of Quantum Electronics*, 14(9), September 1978.

[29] Amon Yariv, Dan Fekete, and David Pepper. Compensation for channel dispersion by nonlinear optical phase conjugation. *Optics Letters*, 4(2), February 1979.